Développement de détecteurs de neutrons ultra-froids et d'un système d'analyse de polarisation pour la mesure de l'EDM du neutron

Gwendal Rogel

2009

Contents

Part I

L'essentiel...en français

Chapter 1

Introduction

Les moments dipolaires électriques (EDM - Electric Dipole Moment) sont des outils très sensibles dans la recherche d'une violation de la symétrie par renversement du temps (T). Pour l'EDM du neutron, la sensibilité expérimentale s'est améliorée de six ordres de grandeur depuis les années 50. Cela a permis de contraindre, voire d'écarter, de nombreuses extensions possibles du Modèle Standard de la physique des particules. La limite la plus récente sur d_n a été mesurée à l'Institut Laue-Langevin (ILL). L'expérience utilisait le stockage de neutrons ultra-froids (UCN - UltraCold Neutron). La mesure a donnée une limite supérieure de $|d_n| < 2.9 \cdot 10^{-26}$ $e \cdot \mathrm{cm}$.

Cette thèse s'inscrit dans un nouveau projet dont le but est de placer la sensibilité expérimentale à 10^{-28} $e \cdot \mathrm{cm}$. L'expérience s'effectuera au Paul Scherrer Institute (PSI) et utilisera une version améliorée de celle à l'ILL. Cette sensibilité expérimentale accrue sera obtenue par un meilleur contrôle des effets systématiques et une plus grande densité d'UCN. La nouvelle source de neutron de spallation de PSI devrait permettre d'atteindre une densité supérieure d'environ deux ordres de grandeur dans la chambre du spectromètre EDM par rapport à l'ILL. Des détecteurs rapides seront par conséquent nécessaires.

Le travail présenté ici a consisté dans la comparaison de détecteurs d'UCN du point de vue de leur efficacité et de leur sensibilité au bruit de fond. Trois types de détecteurs ont été testés à l'ILL: le cascade-U (GEM-type), le détecteur à gaz ^{3}He, et des scintillateurs dopés au ^{6}Li. De plus, un nouveau système d'analyse simultanée de spin est présenté. Il consiste en deux systèmes de détection (bras) possédant chacun un spin flipper adiabatique, un analyseur de spin, et un détecteur. Les bras détectent chacun une composante de spin, permettant ainsi un comptage des deux états de spin du neutron.

Le chapitre 2 de ce document présente en premier lieu les motivations pour la mesure de l'EDM du neutron. L'expérience RAL-Sussex-ILL est ensuite décrite. Le chapitre 3 expose le principe des détecteurs UCN en lien avec la recherche de l'EDM du neutron. Les résultats de tests expérimentaux effectués à l'ILL sont présentés. L'objectif a été de comparer les détecteurs du point de vue de leur efficacité de détection ainsi que leur sensibilité au bruit de fond. Le chapitre 4 rapporte les tests expérimentaux effectués pour déterminer les performances des outils utilisés dans l'analyse de spin. Les tests de deux exemples de systèmes d'analyse simultanée sont enfin présentés.

Chapter 2

L'EDM du neutron

2.1 Introduction

2.1.1 Symétries et EDM

La violation de P

En 1950, Purcell et Ramsey argumentent sur la possible existence d'un moment dipolaire électrique (EDM - Electric Dipole Moment) pour les particules élémentaires [1]. Selon eux, des expériences devraient être menées afin de vérifier cette possibilité. De plus, ils soulignent le fait que l'existence d'un EDM pour une particule implique la violation de la symétrie de parité (P). En effet, un système quantique non-dégénéré au repos est uniquement défini par son spin $\vec{s}$. Par conséquent, le moment dipolaire électrique $\vec{d}$ doit être proportionnel à $\vec{s}$ [2]. Lorsqu'un champ électrique $\vec{E}$ est appliqué, l'interaction entre $\vec{d}$ et $\vec{E}$ apparaît dans l'Hamiltonien comme $-\vec{d} \cdot \vec{E}$. En appliquant la transformation P (i.e. l'inversion des coordonnées spatiales), $\vec{d} \rightarrow \vec{d}$ et $\vec{E} \rightarrow -\vec{E}$ de telle sorte que $-\vec{d} \cdot \vec{E}$ change de signe. Par conséquent, toute valeur non nulle de l'EDM indiquerait une violation de P. Purcell et Ramsey décident alors de mettre en place une expérience pour la mesure de l'EDM du neutron d_n [3]. Ce choix repose sur le fait que le neutron ne possède pas de charge électrique. Il ne peut donc pas être accéléré en dehors de la région de mesure sous l'application d'un fort champ électrique, nécessaire pour mettre en évidence le moment dipolaire électrique. Bien que le résultat de leur expérience ait été zéro ($d_n = (-0.1 \pm 2.4) \cdot 10^{-26} e \cdot \mathrm{cm}$ [3]), de nombreuses autres tentatives seront réalisées par la suite.

En 1956, Lee et Yang tentent d'expliquer le fameux puzzle $\theta - \tau$ par la violation de P dans l'interaction faible. Ils proposent notamment un certain nombre d'expériences visant à le prouver. Un an plus tard, Wu *et al.* observe la violation de P grâce à la mesure d'une asymétrie dans la distribution angulaire des électrons émis par des noyaux polarisés de ^{60}Co [4]. L'argument selon lequel la symétrie de parité priverait les noyaux et les particules élémentaires d'un EDM était donc réfuté.

La violation de CP

L'existence d'EDM de particules peut aussi être considérée du point de vue de la symétrie par renversement du temps (T). Comme expliqué précédemment pour P, on note que l'Hamiltonien $-\vec{d}\cdot\vec{E}$ change de signe sous T puisque $\vec{d} \rightarrow -\vec{d}$ et $\vec{E} \rightarrow \vec{E}$. Donc l'existence d'un EDM implique la violation de T.

En 1954, Lüders formule son fameux théorème CPT — aussi connu sous le nom de théorème Pauli-Lüders. Celui-ci stipule l'invariance des lois physiques sous l'action combinée des symétries de conjugaison de charge C, de parité P et de renversement du temps T [5,6]. Il implique en particulier que la symétrie T équivaut à la symétrie CP. Donc la question de l'existence d'EDM de particules est directement liée à celle de la violation CP.

Comme il le fit concernant la symétrie P, Ramsey réitéra en argumentant pour la symétrie CP/T: "...while such arguments are appealing from the point of view of symmetry, they are not necessarily valid" [7]. La question de la symétrie CP/T ne pouvait donc qu'être résolue expérimentalement, avec l'EDM du neutron comme outil très sensible pour la mettre à jour.

Historiquement, la violation de CP fut découverte en 1964 lorsque Christenson *et al.* l'observa dans la désintégration du méson K^0 [8]. De plus en 1967, la violation de CP apparaît comme l'une des conditions nécessaires introduites par Sakharov — avec la non conservation du nombre baryonique et la rupture de l'équilibre thermique initial — pour expliquer la dominance de la matière sur l'antimatière dans notre univers [9]. Aujourd'hui, les sources de violation CP mesurées sont trop faibles pour expliquer l'asymétrie matière-antimatière observée. De nouvelles sources sont nécessaires et pourrait être découvertes par le biais de la mesure de l'EDM du neutron.

Impact théorique de la mesure de d_n

Le modèle actuel utilisé pour décrire la physique des particules est le Modèle Standard (MS). Il comprend la chromodynamique quantique (QCD) et les théories électrofaibles. Chacune contient des termes violant CP: la phase δ du secteur électrofaible, qui apparaît dans la matrice de mélange des quarks, et l'angle θ de QCD. Les prédictions théoriques basées sur la phase δ conduisent à un EDM du neutron autour de $10^{-32} e\cdot\mathrm{cm}$ [2]. A la différence de δ, l'angle θ de QCD est un paramètre arbitraire sans dimension qui doit être fixé. La limite supérieure expérimentale actuelle sur d_n est $|d_n| \lesssim 10^{-26} e\cdot\mathrm{cm}$ [10]. Connaissant d_n, θ est déterminé à moins de 10^{-9} [11]. Cette valeur étonnament faible conduit à ce que l'on appelle le *Strong CP problem.* Celui-ci n'est pas résolu de manière satisfaisante dans le cadre du MS.

Plusieurs extensions du MS ont été introduites avec plus de paramètres et ainsi plus d'opportunités pour violer CP. En conséquence, elles prédisent des valeurs plus grandes de d_n que le MS et sont donc susceptibles d'être contraintes par l'expérience. Par exemple, les modèles de symétrie gauche-droite, dans lesquels les bosons W_R et Z' sont ajoutés aux particules usuelles du MS, prédisent un EDM du neutron aux alentours de $10^{26\pm1} e\cdot\mathrm{cm}$ [12]. Dans les modèles supersymétriques, chaque particule est associée avec un superpartenaire dont le spin diffère de 1/2 (i.e., le nombre de particules est doublé par rapport au MS). Leur prédictions donnent un EDM du neutron dans la gamme $10^{-25} - 10^{-28} e \cdot \mathrm{cm}$ [13].

2.1.2 L'évolution expérimentale de la limite sur d_n

La limite supérieure expérimentale sur d_n n'a pas cessé de diminuer depuis 1950 (Fig. 2.1). La plupart des expériences recherchant l'EDM du neutron utilisent le même principe, i.e. la méthode de Ramsey des champs oscillants séparés [14]. Elles peuvent être divisées en deux groupes: les expériences en ligne et de stockage. Les premières utilisent des faisceaux de neutrons thermiques traversant la région de mesure [3,15–19], et les secondes stockent des neutrons ultra-froids (UCN - UltraCold Neutron) dans des chambres [10, 20–27]. Puisque la vitesse moyenne des neutrons tend vers zéro dans les expériences de stockage, cela a permis de quasiment éliminer un effet systématique important (l'effet $\vec{v} \times \vec{E}$) qui limite la sensibilité des expériences en ligne. Le meilleur résultat obtenu à ce jour a été publié par la collaboration RAL-Sussex-ILL et donne une limite supérieure sur l'EDM du neutron de $|d_n| < 2.9 \cdot 10^{-26} e \cdot \mathrm{cm}$ (90% C.L.) [10].

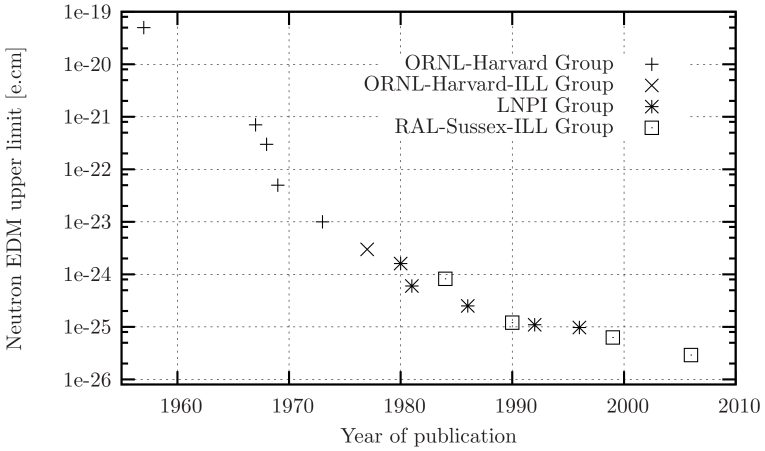

Figure 2.1: Evolution des mesures de l'EDM du neutron depuis 1950. Les résultats sont présentés en fonction du groupe de recherhe impliqué [3, 10, 15–27].

2.2 L'expérience RAL-Sussex-ILL

2.2.1 La source UCN de l'ILL

Les neutrons sont initialement produits par le processus de fission de l'uranium 235. Ils sont tout d'abord refroidis dans le modérateur (D_2O) pour atteindre le régime thermique. Une source froide (20 K) contenant du deutérium liquide (lD_2) placée près du cœur ralentit davantage les neutrons.

La Figure 2.2 montre la manière dont les neutrons sont extraits verticalement de la source froide. A l'entrée de la turbine, seul les neutrons très froids (VCN - Very Cold Neutron) possédant une vitesse d'environ 50 m/s demeurent [28, 29]. Le décalage dans l'espace des phases jusqu'à la région des UCN est dû aux multiples réflections des VCN sur les pales en nickel de la turbine. Celle-ci tourne à la vitesse de 25 m/s. Les UCN sont ensuite disponibles sur quatre lignes. Leur distributions de vitesse s'étendent jusqu'à 20 m/s en piquant à 8-10 m/s selon la ligne [29].

Les densités typiques sont d'environ 100 UCN par cm^3 à l'intérieur de la turbine [29]. Elles valent quelques dizaines d'UCN par cm^3 pour une expérience de stockage [24, 29]. Par exemple, si l'on considère un spectre de stockage avec une vitesse moyenne de 3 m/s, alors le flux d'UCN peut être estimé à $3 \cdot 10^3\,\mathrm{cm}^{-2} \cdot \mathrm{s}^{-1}$.

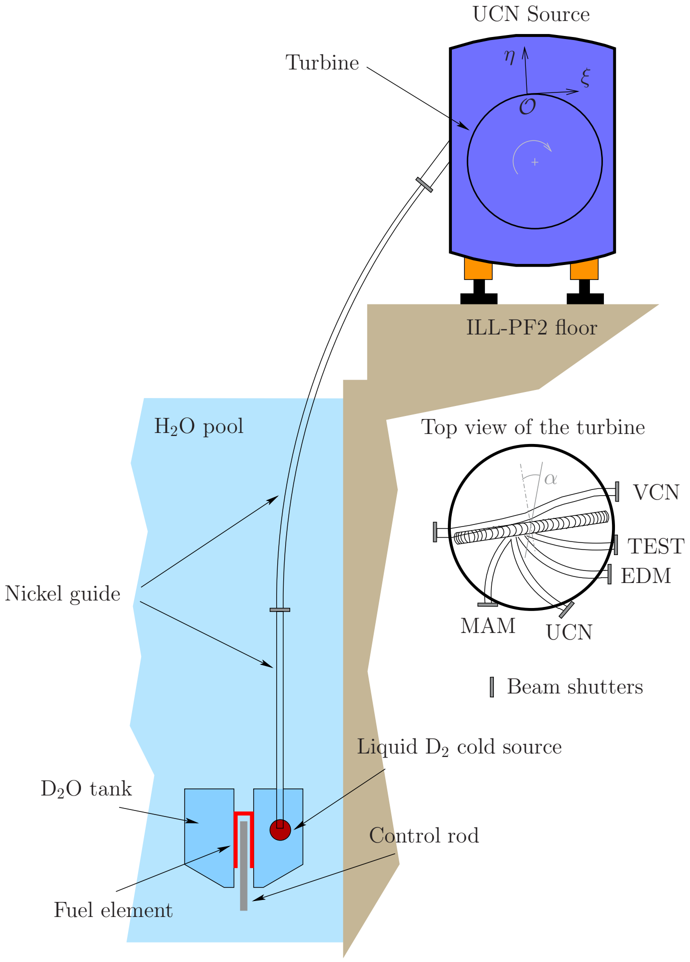

Figure 2.2: Source froide et turbine à l'ILL.

2.2.2 Principe de mesure de l'EDM du neutron

Les UCN sont stockés dans une région où des champs magnétique $\vec{B}_0$ et électrique $\vec{E}$ statiques sont appliqués. De la même manière que le moment magnétique $\vec{\mu}_n$ interagit avec $\vec{B}_0$, l'EDM du neutron $\vec{d}_n$ le fait avec $\vec{E}$. L'Hamiltonien de ces deux interactions s'écrit:

$$H = -\vec{\mu}_n \cdot \vec{B}_0 - \vec{d}_n \cdot \vec{E}. \tag{2.2.1}$$

Puisque l'EDM est aligné selon le spin $\vec{S}$, alors l'Hamiltonien peut se réécrire:

$$H = -(\mu_n \vec{B}_0 + d_n \vec{E}) \cdot \frac{\vec{S}}{S}, \tag{2.2.2}$$

où $S = 1/2$.

La Figure 2.3 montre le schéma de niveaux d'énergie d'un neutron interagissant avec les champs $\vec{E}$ and $\vec{B}_0$. Deux directions du champ électrique sont représentées par rapport au champ $\vec{B}_0$ (i.e. parallèle et anti-parallèle). L'écart entre les niveaux d'énergie du neutron est donné par:

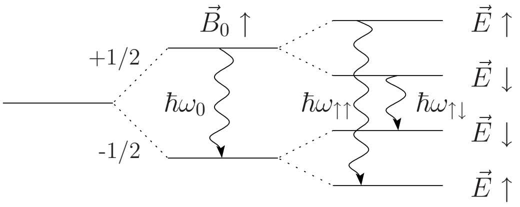

Figure 2.3: Niveaux d'énergie dans un champ magnétique statique $\vec{B}_0$ et pour deux directions du champ électrique $\vec{E}$ par rapport à $\vec{B}_0$. ω_0 est la fréquence de Larmor.

$$\hbar\omega_n = -2\mu_n B_0 \pm 2 d_n E, \tag{2.2.3}$$

où ω_n est la fréquence de précession du neutron. Selon la direction du champ magnétique ($\uparrow$) ou du champ électrique ($\uparrow$ ou $\downarrow$), ω_n peut prendre deux valeurs. On les note $\omega_n^{\uparrow\uparrow}$ ($\omega_n^{\uparrow\downarrow}$) pour le signe $-$ (signe $+$) dans l'équation (2.2.3). En différenciant ces deux valeurs, on trouve:

$$\delta\omega = \omega_n^{\uparrow\uparrow} - \omega_n^{\uparrow\downarrow} = -\frac{4 d_n E}{\hbar}. \tag{2.2.4}$$

Donc la mesure du moment dipolaire électrique du neutron est équivalent à mesurer un décalage en fréquence entre les deux configurations des champs: $\vec{B}_0 \uparrow\uparrow \vec{E}$ et $\vec{B}_0 \uparrow\downarrow \vec{E}$. Par exemple, $d_n = 1 \cdot 10^{-26} e \cdot \mathrm{cm}$ équivaut à un décalage dans la fréquence de précession d'environ 0.1 μHz. En pratique, on mesure la fréquence de precession des UCN par la méthode des champs oscillants séparés introduite par Ramsey [14]. Le principe de cette mesure est décrit plus loin dans ce document p.43.

2.2.3 Description du spectromètre et mesure

Un schéma du spectromètre est donné en Fig. 2.4. Les UCN sont produits par la turbine à ILL/PF2. Ils sont polarisés par transmission dans une fine feuille de fer magnétisée. Ils remplissent ensuite un volume de 20 litres délimité par un cylindre en quartz et les deux électrodes. Une bobine enroulée autour du volume sous vide contenant la chambre UCN crée un champ magnétique uniforme vertical B_0 de environ 1 μT. Il est protégé des perturbations magnétiques extérieures par un blindage constitué de quatre couches de mu-métal (facteur de blindage ~ 10^4 [27]). Un fort champ électrique (~10 kV/cm) est produit par l'application d'une haute tension (positive ou négative) sur l'électrode supérieure. L'électrode du bas reste à la masse. Après avoir rempli la chambre de stockage pendant 40 s, son entrée est fermée pneumatiquement. Ensuite pendant une centaine de secondes, les UCN sont maintenus dans la chambre. La fréquence de précession des neutrons est mesurée par la méthode de Ramsey [14].

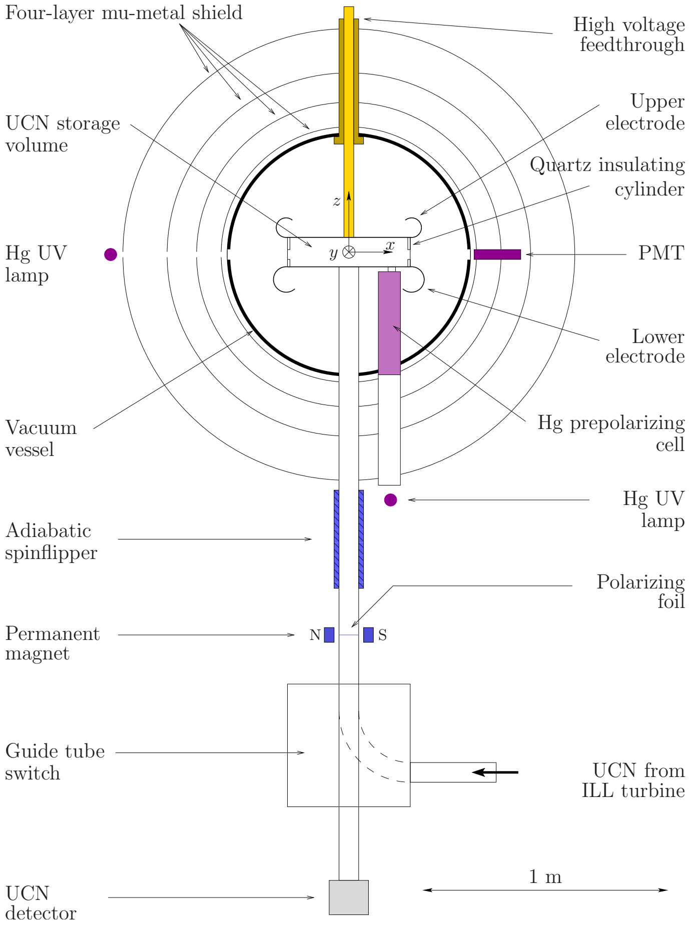

Figure 2.4: Schema de l'expérience RAL-Sussex-ILL at ILL/PF2.

A la fin de la mesure de Ramsey, l'entrée de la chambre est ouverte et les UCN chutent. La feuille d'analyse n'est capable d'analyser qu'un seul état de spin. Ainsi, un spin flipper permet de sélectionner séquentiellement les états de spin. En pratique, le spin flipper est éteint pendant 8 s après l'ouverture de la chambre, puis il est activé pendant 20 s et la période de comptage se termine avec 12 s où le spin flipper est à nouveau éteint.

Deux nombres de coups sont donc enregistrés en fonction de l'état du spin flipper. On les note N_+ et N_-. Le signe $+$ correspond à l'état de spin qui est sélectionné après le premier passage des neutrons à travers le polariseur. On peut montrer que l'EDM d_n du neutron peut s'exprimer en fonction de N_+ et N_- pour les deux configurations des champs magnétique et électrique verticaux [2]:

$$d_n \approx -\frac{\hbar(\Delta N^{\uparrow\uparrow} - \Delta N^{\uparrow\downarrow})}{4\alpha E T N_0}. \tag{2.2.5}$$

où $\Delta N = N_+ - N_-$ a deux valeurs pour les deux configurations des champs. T est la période de précession libre dans la méthode de Ramsey, α repésente l'efficacité de maintenir la polarisation dans tout le système [30], et N_0 est le nombre total de neutrons détectés. L'expression de la sensibilité statistique σ_{d_n} se déduit alors de l'équation précedente:

$$\sigma_{d_n} \approx \frac{\hbar}{2\alpha E T \sqrt{N_0}}, \tag{2.2.6}$$

Les valeurs typiques pour les paramètres dans (2.2.6) étaient $\alpha = 0.6$, $E = 10$ kV/cm, $T = 130$ s and $N_0 = 14000$ neutrons par cycle de 210 s. Ceci conduit à une incertitude statistique de $2 \cdot 10^{-25} e \cdot \mathrm{cm}$ par jour [31].

2.3 Le projet EDM à PSI

Ce projet est divisé en trois phases. La première s'est déroulée entre 2004 et 2008 et est à présent terminée. Elle consistait à utiliser le spectromètre RAL-Sussex-ILL à l'ILL tout en l'améliorant. La seconde phase a débuté en 2009 avec le déménagement du spectromètre à PSI. L'objectif est de l'utiliser avec la nouvelle source UCN à spallation qui devrait augmenter de deux ordres de grandeur la densité d'UCN à l'intérieur de la chambre de stockage par rapport à l'ILL [32]. L'objectif sera de mesurer un EDM aux alentours de $10^{-27} e \cdot \mathrm{cm}$. Parallèlement à cela, un nouveau spectromètre sera construit en tirant avantage des tests et améliorations précédents. L'objectif de cette troisième phase sera de mesurer un EDM cette fois aux environs de $10^{-28} e \cdot \mathrm{cm}$. Plus de détails sont donnés dans [33].

Une partie des améliorations consiste notamment dans le développement de détecteurs rapides capables de faire face à de hauts taux de comptage. De plus, afin de diminuer les dépolarisations au sein de la géométrie, la méthode d'analyse de spin simultanée a été proposée à la place de l'analyse séquentielle décrite précédemment. Ces deux points ont fait l'objet de cette thèse.

Chapter 3

Etude de détecteurs UCN

Le principe d'un détecteur UCN est similaire à celui utilisé pour les neutrons lents. La détection s'effectue en deux étapes. Tout d'abord, les neutrons sont convertis en particules chargées ; pour ce faire, on utilise des noyaux avec une grande section efficace d'absorption (e.g. ^{3}He, ^{6}Li, ^{10}B, ^{235}U, etc). Ensuite, les charges créées sont collectées pour donner un signal contenant l'information de la détection neutronique.

Ce chapitre présente des tests expérimentaux menés à l'ILL (PF2) avec trois types de détecteurs: le détecteur à gaz ^{3}He, le cascade-U (type GEM) et des scintillateurs dopés au ^{6}Li (type GSx). L'objectif a été de les comparer du point de vue de leur efficacité de détection ainsi que leur sensibilité au bruit de fond.

3.1 Caractéristiques requises

Le tableau 3.1 présente la liste des caractéristiques importantes pour le développement de détecteurs UCN. Les ordres de grandeur donnés tiennent compte des besoins pour l'expérience nEDM.

	Paramètre	Ordre de grandeur	Commentaires
a.	Efficacité ϵ	$\epsilon > 50\%$	vitesses < 10 m/s
b.	Taux de comptage maximum	$10^{6} - 10^{7}$ c/s	détecteurs avec ∅ 80 mm
c.	Sensibilité au bruit de fond	$\sim 10^{-3}$ c/s	
d.	Résistance au flux	$> 10^{12}\,\mathrm{cm}^{-2}\,\mathrm{y}^{-1}$	
e.	Vitesse critique v_c	$v_c < 4$ m/s	

Table 3.1: Paramètres importants à prendre en compte pour le développment d'un détecteur UCN.

a. L'efficacité de détection doit être la plus grande possible pour des UCN avec des vitesses inférieures à 10 m/s. Les principales limitations sont: i) la vitesse critique du détecteur ; ii) la présence d'une zone morte avant la détection (e.g. perte par absorption) ; iii) la présence d'une zone morte après la détection (perte des particules chargées résultant de la détection de l'UCN). Ce dernier point est particulièrement important pour le cascade-U.

b. Avec le développement de nouvelles sources plus intenses d'UCN, les détecteurs doivent être capable de faire face aux hauts taux de comptage. Les valeurs données dans le tableau 3.1 prennent en compte la densité attendue pour la nouvelle source à PSI. On considère une densité autour de 1000 UCN par cm^3 à l'intérieur de la chambre de stockage du spectromètre EDM, ainsi qu'une vitesse moyenne de 3 m/s. Par conséquent, le taux de comptage maximal pour un détecteur de 80 mm de diamètre est d'environ 10^7 c/s.

c. Une faible sensibilité au bruit de fond est nécessaire pour les détecteurs situés à proximité de sources UCN. Le bruit de fond gamma mais aussi celui dû aux neutrons thermiques doit être pris en compte. Des mesures à l'ILL (PF2) ont permis d'évaluer à quelques 10^{-3} c/s la sensibilité des détecteurs à gaz ^{3}He et cascade-U.

d. Dans le cas des expériences où les temps de mesures sont importants, on doit prendre en compte les dommages causés à l'intérieur du détecteur soumis au flux. Par exemple, l'acquisition de données sur l'expérience EDM se fait sur plusieurs mois.

e. La vitesse critique v_c du détecteur influence directement son efficacité à basse vitesse. Bien entendu, une valeur nulle serait préférable. Dans la mesure du possible, abaisser la position verticale d'un détecteur peut permettre d'éviter l'effet de la vitesse critique en accélérant les UCN. De plus, des expériences, avec des détecteurs semi-conducteurs utilisant des multi-couches de ^{6}Li/Ti, ont montré la possibilité de mesurer des UCN avec une efficacité de 30-40% dans la gamme de vitesse 2-2.6 m/s [34].

Dans l'expérience nEDM, la détection sera couplée avec l'analyse de spin. Par conséquent, il est aussi important que les détecteurs aient une faible sensibilité aux champs magnétiques. D'une manière générale, tout détecteur doit être aussi robuste que possible, facile à mettre en œuvre et pas cher.

3.2 Etude de l'énergie déposée

3.2.1 Le détecteur à gaz ^{3}He

3.2.1.1 Principe de fonctionnement

Le détecteur à gaz ^{3}He est le détecteur de base pour les UCN. Dans nos tests, nous avons utilisé le type "Strelkov-Dunia-10" dont le schéma de principe est donné Fig. 3.1.

Les UCN pénètrent à l'intérieur du détecteur à travers une feuille d'aluminium de 100 μm d'épaisseur. Le gaz joue à la fois le rôle de convertisseur neutronique et de zone de collection des particules chargées. L'absorption des neutrons est réalisée par le noyau d'^{3}He qui possède une grande section efficace d'absorption thermique

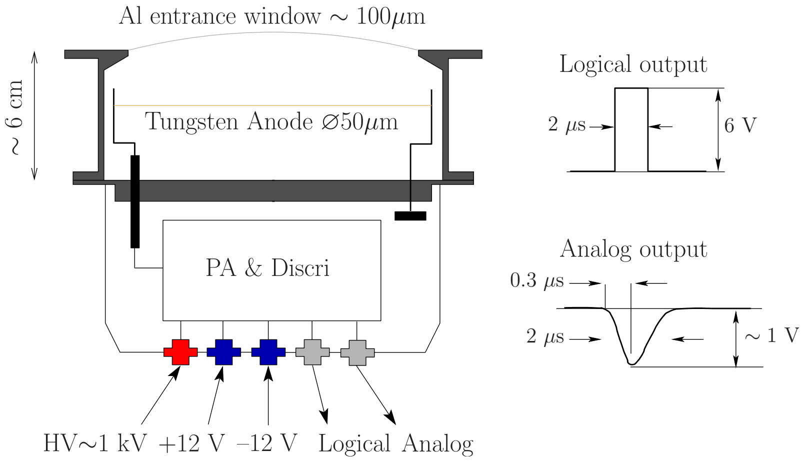

Figure 3.1: Schéma d'un détecteur à gaz ^{3}He type "Strelkov-Dunia-10".

σ_a^{th} de 5330 barn. La capture suit la réaction:

$$\mathrm{n} +^3 \mathrm{He} \longrightarrow \mathrm{p} + \mathrm{t} + 764\,\mathrm{keV}.$$

Les particules chargées résultantes ionisent le gaz Ar/CH_4 ou Ar/CO_2. Les valeurs standards des pressions partielles sont $p(^3He) = 15$ mbar, $p(CH_4/CO_2) = 15$ mbar and $p(Ar) = 1.1$ atm. Les électrons produits par les protons et tritons sont collectés sur une anode de 50 μm de diamètre. Le détecteur possède un préamplificateur et un discriminateur internes. Deux sorties, analogique et logique (TTL), sont disponibles. Le seuil du signal logique peut être contrôlé manuellement.

3.2.1.2 Spectre en amplitude

La durée du signal analogique est typiquement de 1 à 2 μs, ce qui en fait un détecteur lent. Après amplification via un amplificateur de spectroscopie, le signal est codé en amplitude sur 12 bits (ADC812F [35]).

La Figure 3.2 montre un spectre en amplitude mesuré à ILL/PF2 sur la ligne EDM. On observe trois régions. Le bruit électronique et celui dû aux interactions gamma se situe en-dessous du canal 300. Ensuite viennent les événements de bord. Ils apparaissent lorsqu'une des deux particules chargées (p, t) sort du détecteur et ne dépose donc pas toute son énergie. Enfin, lorsque les 764 keV de la réaction de capture sont déposés dans le gaz, un pic est enregistré autour du canal 1800. Sa résolution est d'environ 10%.

La contribution de bruit de fond dans le signal neutron (événements de bords plus pic) représente seulement 1% de la quantité totale de neutrons détectés. Elle est principalement due aux neutrons thermiques. En effet, ce détecteur possède une très faible sensibilité au bruit de fond gamma puisque la densité du volume de détection (gaz) est faible. De plus, des matériaux avec un faible Z sont utilisés (^{3}He, Ar, CO_2).

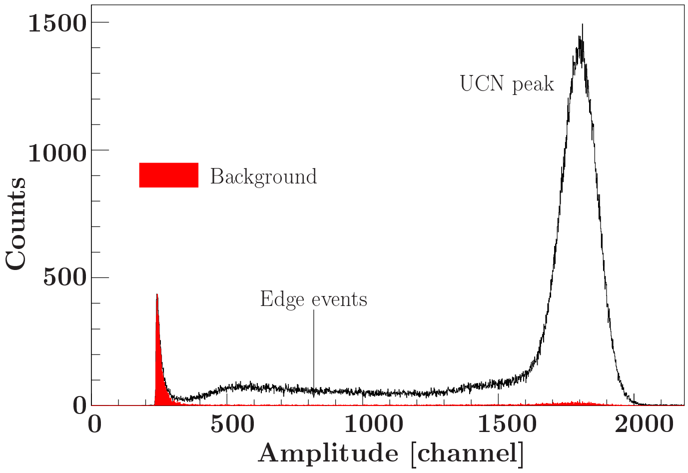

Figure 3.2: Spectre en amplitude d'un détecteur à gaz ^{3}He.

3.2.2 Le cascade-U

3.2.2.1 Principe de fonctionnement

Le cascade-U utilise la technologie GEM [36]. La Figure 3.3 montre une photographie du détecteur (sur la droite). La feuille d'entrée est démontée (sur la gauche). Le carré gris foncé (8 cm x 8 cm) au centre de la feuille d'aluminium (100 μm d'épaisseur) correspond à la couche de ^{10}B utilisée pour convertir les neutrons.

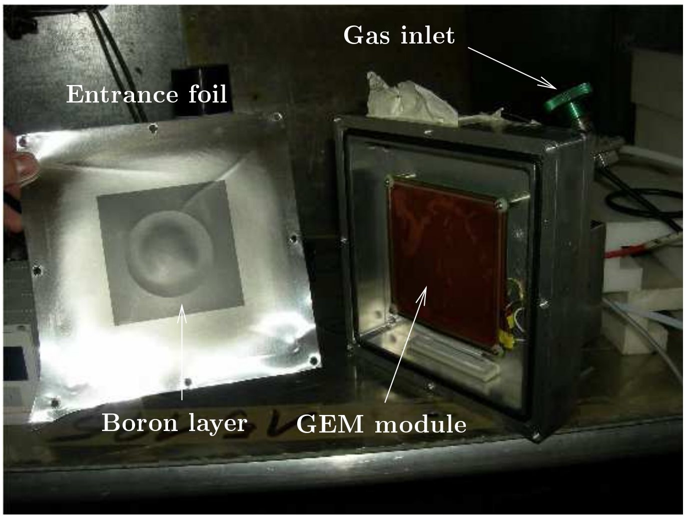

Figure 3.3: Détecteur cascade-U avec la feuille d'entrée en aluminium démontée. Le carré gris foncé correspond à la couche de ^{10}B. L'intérieur du détecteur laisse apparaître le module GEM.

Les UCN sont hautement absorbés par les noyaux de ^{10}B dont la section efficace thermique σ_a^{th} est 3840 barn. Deux réactions de capture peuvent se produire suivant les rapports de branchement 6.4% et 93.6%:

$$\begin{array}{lcll} \mathrm{n} + {}^{10}\mathrm{B} & \longrightarrow & \alpha\ (1.78\ \mathrm{MeV}) + {}^{7}\mathrm{Li}\ (1.01\ \mathrm{MeV}) & [6.4\%] \\ \mathrm{n} + {}^{10}\mathrm{B} & \longrightarrow & \alpha\ (1.47\ \mathrm{MeV}) + {}^{7}\mathrm{Li}\ (0.84\ \mathrm{MeV}) + \gamma\ (0.48\ \mathrm{MeV}) & [93.6\%] \end{array}$$

Les particules α et ^{7}Li résultant de la capture entrent dans un volume de gaz Ar/CF$_4$ (70/30) à une pression de 1 bar. Des paires e^{-}-ion primaires sont produites le long de leur parcours dans le gaz. Un centimètre plus loin, les électrons sont multipliés à proximité des trous du module d'amplification GEM et le traversent. Ils sont finalement détectés par un circuit de $10 \times 10\,\mathrm{cm}^2$ ayant un total de 64 pixels (8 x 8). Ceci permet l'utilisation de l'imagerie 2D. Nous utilisons le signal intégré sur tous les pixels. Pour plus de détails, voir [37].

3.2.2.2 Spectre en amplitude

Le signal provenant du détecteur est amplifié par un amplificateur de spectroscopie puis échantillonné en amplitude avec un codeur 12 bits (ADC812F [35]).

La Figure 3.4 montre trois spectres en amplitude obtenus sur la ligne TEST à PF2. Ils correspondent à trois épaisseurs de la couche de bore: 50 nm, 200 nm et 800 nm.

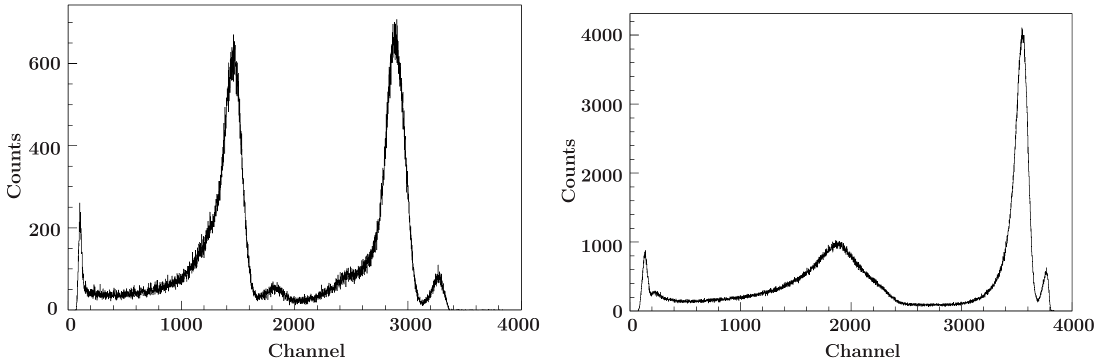

(a) 50 nm (b) 200 nm

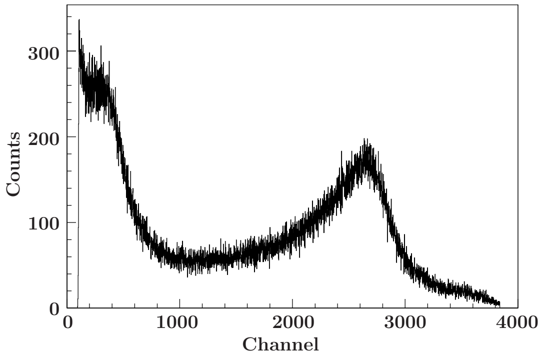

(c) 800 nm

Figure 3.4: Spectres en amplitude du cascade-U pour trois différentes épaisseurs de ^{10}B.

Les quatre pics correspondant aux deux rapports d'embranchement sont bien identifiables dans le cas de l'épaisseur de 50 nm. les deux à bas canal correspondent aux ^{7}Li et les deux autres aux alphas. L'outil de simulation a montré que lorsque l'épaisseur augmente, les particules chargées perdent plus d'énergie dans la couche de bore. Dans le cas d'une épaisseur de 800 nm, les pics se confondent.

3.2.3 Les scintillateurs dopés au ^{6}Li

Les scintillateurs utilisés durant les tests sont produits par Applied Scintillation Technologies (AST). Ils appartiennent à la famille des GS [38]. Pour la détection des UCN, ils ont été utilisés pour la première fois en 2003 par notre groupe du LPC [39].

3.2.3.1 Propriétés des verres GSx

La capture des neutrons est réalisée par le noyau de ^{6}Li (σ_a^{th} = 940 barn). La réaction de capture est la suivante:

$$n +^6 \mathrm{Li} \longrightarrow \alpha\,(2.05\,\mathrm{MeV}) + \mathrm{t}\,(2.73\,\mathrm{MeV}).$$

A l'intérieur du verre, l'alpha et le triton ont respectivement un parcours de 6 et 36 μm. Ces particules chargées activent les centres cérium (Ce^{3+}). Un maximum de lumière émise est obtenu pour une longueur d'onde de 395 nm [38]. Cela permet d'utiliser divers photomultiplicateurs (PM) sans devoir décaler la longueur d'onde. Grâce à leur faible temps de réponse, autour de 50-70 ns, ces scintillateurs peuvent être utilisés pour mesurer de hauts taux de comptage [19].

Le tableau 3.2 résume les caractéristiques des trois scintillateurs qui ont été utilisés dans les tests, soient le GS3, le GS10 et le GS20.

	GS3	GS10	GS20
Concentration de ^{6}Li [%]	0.01	7.5	95
Densité de ^{6}Li [10^{21} at.cm^{-3}]	$6.4 \cdot 10^{-4}$	1.6	20.0
Densité du verre [g/cm^3]	2.66	2.50	2.50
Indice de réfraction	1.58	1.55	1.57
Intensité lumineuse relative	100	85	85
Potentiel de Fermi [neV]	101	85	103
Vitesse critique [m/s]	4.4	4.0	4.4

Table 3.2: Propriétés principales des scintillateurs GS3, GS10 et GS20.

Tandis que le GS10 possède une concentration naturelle de ^{6}Li, le GS3 est déplété et le GS20 dopé en ^{6}Li. Leur densité est proche de 2.5 g/cm^3 et leur indice de réfraction valent environ 1.6. Les concentrations de ^{6}Li données dans le tableau 3.2 sont les valeurs initiales avant la fusion des verres. Les produits finis peuvent avoir une densité de ^{6}Li plus faible [38]. Les potentiels de Fermi (vitesses critiques) sont calculés d'après la composition atomique de chaque scintillateur [38] et des longueurs de diffusion neutroniques pour chaque noyau [40]. Le GS10 possède la vitesse critique la plus faible parmi les verres testés avec 4.0 m/s. Elle reste néanmoins supérieure à celle du détecteur à gaz ^{3}He valant 3.2 m/s. Ce dernier est donc plus efficace à basse vitesse (3-5 m/s) comme nous le verrons par la suite.

3.2.3.2 Mise en œuvre des scintillateurs

Dans les derniers tests effectués, les verres sont couplés directement (i.e. pas de guide de lumière) à un photomultiplicateur de type XP53X2/B (Photonis) avec une embase de type VD202K/03 (type A). La surface d'entrée est recouverte d'une fine couche de 200 nm d'aluminium qui joue le rôle de réflecteur. Le signal de sortie du PM dure 200 ns. Il est amplifié et intégré par un QDC (LeCroy 4300B FERA). Bien que cette méthode fut celle adoptée la plupart du temps, le codage en amplitude a aussi été utilisé. Les deux techniques ont donné des résultats similaires.

L'avantage d'utiliser le ^{6}Li comme convertisseur est la grande quantité d'énergie libérée au sein du scintillateur à la suite d'une capture. Lorsque les deux produits de la réaction sont stoppés dans le verre, une énergie de 4.78 MeV est déposée. En comparaison, une capture neutronique sur un noyau de ^{10}B ne libère au maximum que 2.79 MeV. Dans le cas de l'^{3}He, l'énergie déposée vaut 746 keV. Par conséquent, cela peut permettre de distinger la plupart des signaux neutrons de ceux produits par les rayons gammas, toujours présents à proximité des sources UCN. Pour les verres dopés au ^{6}Li, il a été noté qu'un gamma de 1.5 MeV produit la même quantité de photons que lors d'une capture neutronique accompagnée d'un dépôt total de 4.78 MeV [41]. Néanmoins, le parcours des électrons résultant de l'interaction gamma est de plusieurs millimètres. Par exemple, on a estimé que pour les scintillateurs GS, le parcours d'électrons de 1.5 MeV est d'environ 2.2 mm [42]. Ainsi, en réduisant l'épaisseur des verres à quelques centaines de microns, on peut diminuer notablement la contribution du rayonnement gamma.

3.2.3.3 Spectre en charge/amplitude

On présente ici les distributions mesurées pour les trois scintillateurs GS3, GS10 et GS20. Ensuite, des tests effectués avec des systèmes avec deux scintillateurs superposés sont présentés.

Scintillateurs simples

La Figure 3.5 montre les distributions en amplitude obtenues avec des scintillateurs GS3, GS10 et GS20. Les trois ont une épaisseur de 100 μm. Dans ces tests, aucune couche d'aluminium n'est évaporée sur leur face d'entrée. Dans les cas du GS10 et GS20, de la graisse optique (silicone) a été utilisée à l'interface entre le verre et la photocathode du PM. Les mesures ont été réalisées à ILL/PF2 sur la ligne EDM. La distribution de vitesse a été ralentie en utilisant des guides UCN courbés. Une mesure en temps de vol sur la ligne TEST à PF2 a permis d'obtenir un spectre en vitesse (longitudinale) compris entre 0 et 10 m/s avec ce même système de guides.

On retrouve les mêmes types d'événement que pour le détecteur à gaz ^{3}He mais dans des proportions différentes. Pour la distribution en amplitude du GS10, la proportion d'événements de bord est d'environ 30% par rapport au nombre total de neutrons détectés. La résolution du pic est de 7%. Dans le cas du GS20, les événements de bord sont plus importants. En effet, puisque le GS20 est enrichi en ^{6}Li, les captures de neutrons se font majoritairement sur le bord du scintillateur. Le

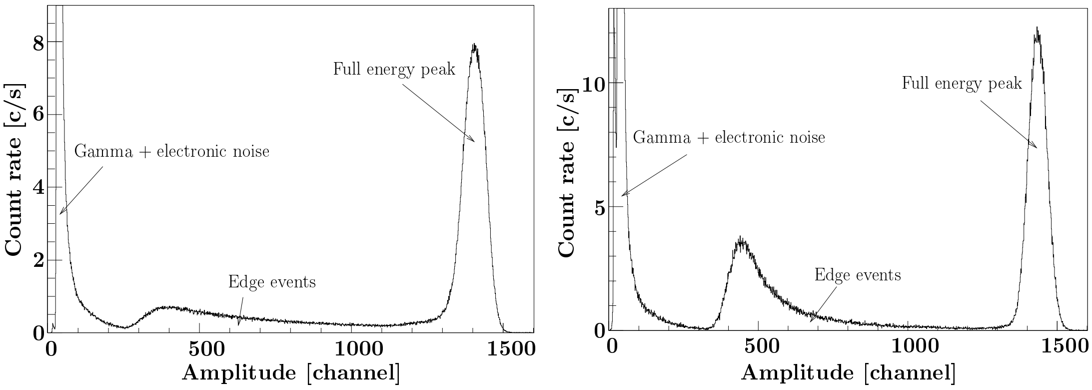

(a) GS10

(b) GS20

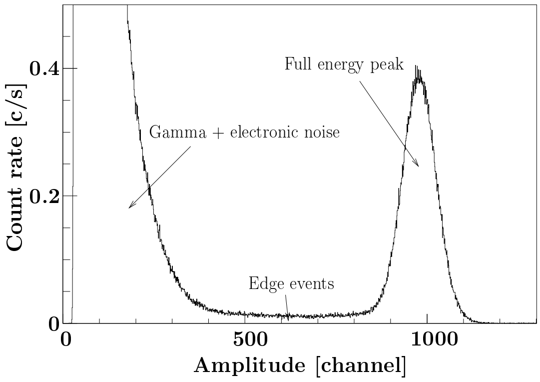

(c) GS3

Figure 3.5: Spectres en amplitude pour des verres GS3, GS10 et GS20. Leur épaisseur est de 100 μm. La mesure a été réalisée sur la ligne EDM (ILL/PF2). La distribution de vitesse est ralentie par le biais de guides courbés.

nombre d'événements de bord vaut 45% du nombre total de neutrons détectés pour le GS20. Concernant le GS3, très peu d'UCN sont détectés (~ 3%) car la densité de ^{6}Li est très faible. Etant donné que nous n'avons pas utilisé de graisse optique pour ce test, la position du pic UCN est plus basse que dans les cas des GS10 et GS20.

Les simulations Monte-Carlo montrent que lorque l'on prend les densités de ^{6}Li données dans le tableau 3.2, on ne retrouve pas les proportions d'événements de bords ni les efficacités obtenues expérimentalement. Par exemple, des mesures avec le GS10 100 μm ont montré qu'il est 25-30% moins efficace qu'un GS10 500 μm (voir le paragraphe 3.4). Or, les simulations avec un contenu en ^{6}Li de 7.5% indiquent qu'une épaisseur de 100 μm de GS10 est suffisante pour mesurer 97% des neutrons incidents (pour la même distribution de vitesse que lors du test expérimental). Pour retrouver les résultats expérimentaux du GS10, la concentration en ^{6}Li a été modifiée à 3.4% dans les calculs. Le tableau 3.3 donne les libres parcours moyens du GS3, du GS10 (3.4% de ^{6}Li) et du GS20. La distribution de vitesse considérée est celle de la ligne TEST. Elle a une composante en vitesse longitudinale comprise entre 0 et 16 m/s et piquant à 8 m/s. La composante transverse est prise entre 0 et 7 m/s.

	GS3	GS10	GS20
Libre parcours moyen [μm]	$6 \cdot 10^4$	50	2

Table 3.3: Libre parcours moyen calculé dans le GS3, le GS10 et le GS20. Le spectre en vitesse UCN des simulations est celui de la ligne TEST.

Scintillateurs doubles

Les scintillateurs doubles ont été développés afin d'améliorer la séparation entre UCN et gammas en récupérant la lumière perdue à cause des événements s'échappant du scintillateur. La Figure 3.6 montre le schéma d'un ensemble GS3/GS20. Les neutrons pénètrent d'abord dans le GS3. Comme il est quasi-transparent aux UCN, ceux-ci n'interagissent pas et sont donc capturés dans le GS20. Ainsi, si les particules chargées (α, t) s'échappent, alors ils déposeront le reste de leur énergie dans le GS3. On peut donc mesurer les 4.78 MeV issus de la capture du neutron. Et les événements de bord sont supprimés.

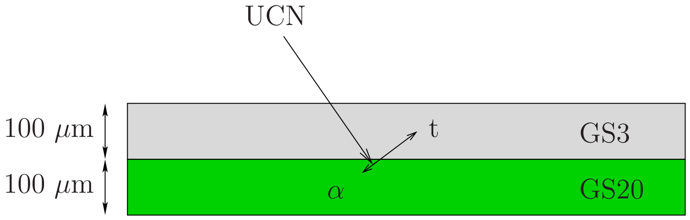

Figure 3.6: Schéma d'une capture UCN au sein d'un ensemble GS3/GS20.

La Figure 3.7 montre le spectre en charge d'un ensemble GS3/GS20. Ce test a été réalisé sur la ligne TEST. Il n'y a pas de graisse optique ni entre les deux verres, ni entre le GS20 et la photocathode du PM. L'épaisseur des deux scintillateurs est de 100 μm. La face d'entrée du GS3 a été recouverte d'une fine couche d'aluminium.

La contribution gamma (plus bruit électronique) est située en-dessous du canal 250. La proportion d'événements de bord est d'environ 3% du nombre total de neutrons détectés. Cela est 8-10 fois moins que dans le cas du scintillateur simple GS10 100 μm. Par conséquent, la séparation entre les signaux UCN et gammas a été améliorée avec le système GS3/GS20.

A l'issue de ces mesures, d'autres tests ont été menés portant sur la collection de lumière de l'ensemble double scintillateur. L'objectif était de comprendre l'origine des deux pics de la Fig. 3.7. Des systèmes GS3/GS10 et GS3/GS20 ont été testés. L'épaisseur des verres est de 100 microns chacun. Leur diamètre est de 1 pouce. Les scintillateurs sont placés au centre des PM de 3 pouces. De la graisse optique est appliquée à l'interface entre les deux scintillateurs et au niveau de la photocathode. De plus, pour ces tests, la distribution de vitesse de la ligne EDM a été ralentie en utilisant des guides courbés. La composante de vitesse longitudinale est alors comprise entre 0 et 10 m/s. On utilise ici l'amplification et le codage en amplitude

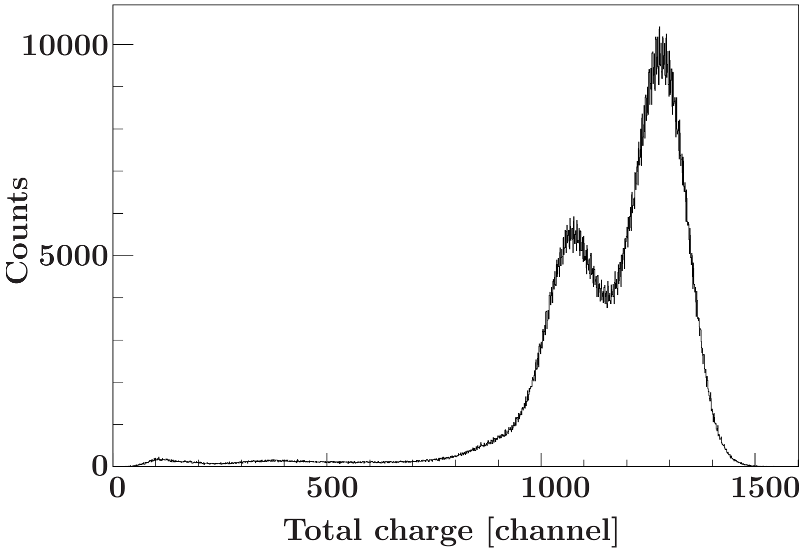

Figure 3.7: Spectre en charge du scintillateur double GS3/GS20.

du signal issu du PM.

La Figure 3.8 montre que l'utilisation de la graisse optique améliore la collection de la lumière. La position moyenne des deux pics augmente lorsque la graisse est appliquée. De plus, ils sont presque complètement superposés pour le GS3/GS20 et forment un seul pic dans le cas du GS3/GS10. Par conséquent, l'existence des deux pics est due à des problèmes de collection de lumière.

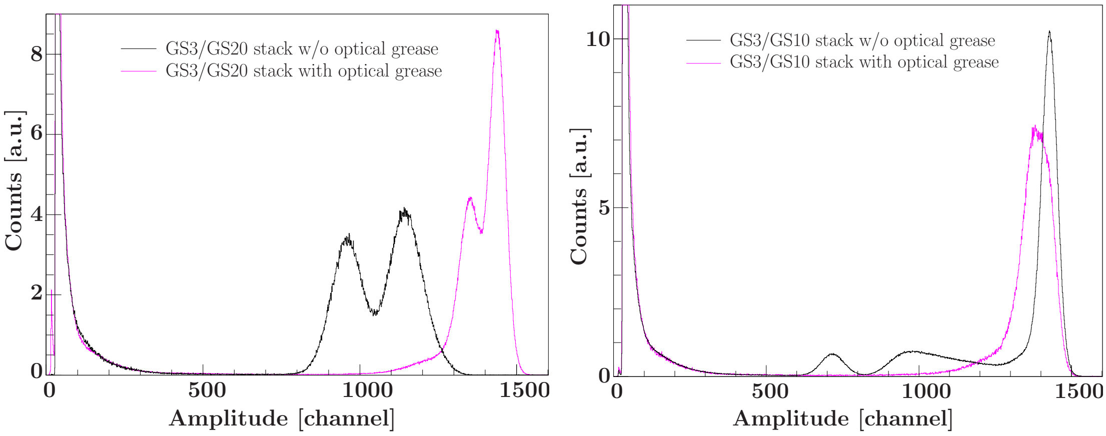

(a) Ensemble GS3/GS20 (b) Ensemble GS3/GS10

Figure 3.8: Effet de la graisse optique pour deux systèmes double scintillateur.

3.3 Sensibilité au bruit de fond

Trois contributions de bruit de fond peuvent être identifiées: i) le bruit électronique, ii) le bruit de fond gamma, et iii) le bruit dû aux neutrons thermiques. Le bruit électronique ainsi que le bruit gamma ont une faible amplitude (ou charge) alors que les signaux correspondant aux neutrons thermiques ont une amplitude (ou charge) plus élevée en se superposant aux signaux UCN.

Les résultats présentés précédemment ont été obtenus en ligne (ligne TEST ou EDM à ILL/PF2). Ici, on cherche à mesurer la sensibilité intrinsèque des détecteurs. Pour ce faire, ils sont placés hors ligne et reposent sur le sol. Un blindage constitué de briques de plomb et de paraffine les entoure. Le tableau 3.4 résume les taux de bruit de fond mesurés pour quatre détecteurs à ILL/PF2. Ils ont été estimés en considérant la région en amplitude (ou charge) qui correspond aux signaux UCN, i.e. la région des événements de bords et du pic de pleine énergie.

Détecteurs	GS10 (100 μm)	GS10 (500 μm)	^{3}He	cascade-U
Taux de comptage [10^{-3} c/s]	130±12	720±25	15±1	20±1

Table 3.4: Mesures des taux de comptage de bruit de fond à ILL/PF2.

Les scintillateurs et les détecteurs à gaz ont la même sensibilité aux neutrons thermiques. Mais vu leur densité plus importante, les verres sont plus sensibles au rayonnement gamma (spécialement dans la région des événements de bords). On peut donc voir que les scintillateurs montrent une sensibilité environ 10 fois plus grande que les détecteurs à gaz.

3.4 Comparaison des efficacités de détection

3.4.1 Scintillateurs GSx

Mesures en ligne

Le tableau 3.5 compare les efficacités de détection entre des scintillateurs GS10 et le détecteur à gaz ^{3}He. Les tests ont été réalisés sur la ligne EDM à ILL/PF2. Le temps de vol était mesuré afin d'extraire le distribution de vitesse longitudinale. A l'entrée des détecteurs était placé un collimateur en polyéthylène de 5 mm d'épaisseur, avec un diamètre d'ouverture de 8 mm. Le détecteur ^{3}He (type Strelkov-Dunia-10) avait été rempli six mois avant ces tests.

Détecteurs	GS10 (100 μm)	GS10 (250 μm)	GS10 (500 μm)
Efficacité /^{3}He	$82.3 \pm 0.3\%$	$91.0 \pm 0.2\%$	$123.6 \pm 0.3\%$

Table 3.5: Efficacités de verres GS10 relatives au détecteur à gaz ^{3}He. Les erreurs sont statistiques.

Le GS10 500 μm est environ 20% plus efficace que le détecteur à gaz ^{3}He. Les scintillateurs plus fins sont moins efficaces puisque les UCN les plus rapides traversent le verre sans être capturés.

Mesures avec le spectromètre nEDM

Nous avons comparé les efficacités de détection des scintillateurs GSx avec le détecteur à gaz ^{3}He sous le spectromètre EDM. Le GS10 100 μm, le GS10 500 μm et un système double GS3/GS20 (100 μm/100 μm) ont été testés. Pour ces mesures, la chambre UCN du spectromètre est remplie pendant 40 s. Ensuite, les neutrons sont stockés pendant τ_s valant 5 ou 100 s afin d'obtenir des distributions de vitesse respectivement rapide ou lente à la sortie de la chambre [43]. Le tableau 3.6 montre les efficacités des scintillateurs par rapport au détecteur à gaz ^{3}He.

Détecteurs	GS10 (100 μm)	GS10 (500 μm)	GS3/GS20
Efficacité /^{3}He (τ_s = 100 s)	$88.1 \pm 0.3\%$	$94.5 \pm 0.8\%$	$81.6 \pm 0.6\%$
Efficacité /^{3}He (τ_s = 5 s)	$91.7 \pm 2.3\%$	$100 \pm 2.9\%$	$84.8 \pm 2.7\%$

Table 3.6: Efficacités relatives entre les scintillateurs GSx et le détecteur à gaz ^{3}He. Les mesures ont été réalisées sous le spectromètre EDM. Les erreurs sont d'origine statistique et prennent en compte la soustraction du bruit de fond.

Le GS10 500 μm est plus efficace que le GS10 100 μm. Néanmoins, à la différence des mesures en ligne précédentes, l'efficacité relative est seulement ici de 7-8%. Ceci est dû au fait que la distribution de vitesse est globalement plus lente que pour les tests sur la ligne EDM. En conséquence, moins d'UCN traversent dans le cas du GS10 100 μm.

Pour la distribution de vitesse lente (τ_s = 100 s), le détecteur à gaz ^{3}He est plus efficace que les scintillateurs. Pour le spectre rapide (τ_s = 5 s), il est toujours plus efficace sauf dans le cas du GS10 500 μm qui a une efficacité de détection équivalente. On peut noter que ce dernier a une efficacité relative à l'^{3}He plus faible dans le cas d'un spectre lent que d'un spectre rapide. C'est sans doute à cause de sa vitesse critique qui est plus importante. On le voit d'ailleurs également pour le GS10 100 μm et le GS3/GS20. Le détecteur à gaz ^{3}He a la vitesse critique la plus faible avec 3.2 m/s. Au contraire, celle du GS10 vaut 4.0 m/s et celle du GS3/GS20 vaut 4.4 m/s.

Néanmoins, cela ne peut pas expliquer complètement le fait que le GS3/GS20 soit encore 15% moins efficace que le détecteur gazeux pour la distribution en vitesse rapide. Récemment des tests ont été réalisés sur la ligne EDM montée avec un guide courbé pour avoir une composante en vitesse longitudinale plus lente comprise entre 0 et 10 m/s. Ils ont montré que le GS3/GS20 était environ 20% moins efficace que le scintillateur simple GS20. Comme le GS3 et le GS20 ont la même vitesse critique (4.4 m/s), alors les neutrons doivent être perdus durant la transmission à l'intérieur du GS3. Cela pourrait donc expliquer la différence obtenue lors de ces tests sous le spectromètre EDM.

3.4.2 Cascade-U

Les résultats de deux séries de tests sont montrés dans le tableau 3.7. Les mesures ont été menées sur la ligne TEST avec détermination du temps de vol. Dans la première série, un GS10 500 μm est comparé au cascade-U dont la face d'entrée possède un dépôt de ^{10}B de 200 nm d'épaisseur. Dans la seconde série, le même GS10 a été testé avec le cascade-U muni de feuilles avec des dépôts de ^{10}B de 50 et 800 nm. Les résultats de simulations sont aussi donnés à titre de comparaison.

Casc. (200 nm)	Casc. (50 nm)	Casc. (800 nm)
80±1 %	54.1±0.1 %	69±3 %
Simulated results		
87 %	47 %	72 %

Table 3.7: Efficacités relatives entre cascade-U et GS10 500 μm.

Le cascade-U avec un dépôt de 200 nm de bore est plus efficace que les autres configurations avec 50 et 800 nm de bore. Mais il est toujours moins efficace de 20% par rapport au GS10 500 μm. Ce résultat est cohérent avec les mesures réalisées dans [44].

Les simulations ont montré qu'il existe une gamme d'épaisseur (260-300 nm) pour laquelle l'efficacité absolue du détecteur plafonne à 82%. Ceci s'explique par le fait que la couche de bore joue le rôle de zone morte: soit la couche est trop fine et les neutrons traversent, soit elle est trop épaisse et les particules chargées (α, ^{7}Li) sont stoppées à l'intérieur. Les résultats des calculs du tableau 3.7 sont proches de ceux mesurés. Les différences peuvent être dues à la qualité de la feuille d'aluminium ou au dépôt de bore. Par exemple, des impuretés dans la feuille d'aluminium ou une couche de bore inhomogène peuvent directement influencer l'efficacité du détecteur.

3.5 Conclusions

Les tests expérimentaux rapportés ici ont permis de comparer trois types de détecteurs. L'inconvénient du cascade-U est sa zone morte en entrée qui diminue significativement (~ 20%) son efficacité de détection. Le scintillateur GS10 peut être compétitif en terme d'efficacité avec le détecteur à gaz ^{3}He. Il reste néanmoins plus sensible au bruit de fond (gamma) (d'un facteur 10 au moins) que ce dernier. L'ensemble double scintillateur GS3/GS20 a permis de remédier à cela. Néanmoins, les mesures ont montré qu'il restait moins efficace de 15-20% par rapport au détecteur à gaz ^{3}He.

Chapter 4

Analyse de spin d'UCN

Ce chapitre rapporte les tests expérimentaux effectués pour déterminer les performances des outils utilisés dans l'analyse de spin. Ils constituent un travail préliminaire au développement d'un système d'analyse simultanée de spin. Deux exemples ont été testés et seront décrits à la fin de ce chapitre.

4.1 Description des outils

4.1.1 Le polariseur/analyseur

4.1.1.1 Principe

La polarisation/analyse de spin utilise l'interaction du moment magnétique du neutron avec un champ magnétique. Lorsque le neutron entre dans une région où règne un champ magnétique, il subit le potentiel $-\vec{\mu} \cdot \vec{B}$. Sa valeur dépend de l'état de spin du neutron. Dans une gamme d'énergie donnée, seule une composante de spin peut pénétrer la région magnétique. Dans nos expériences, on utilise une feuille magnétisée pour polariser/analyser les UCN [45]. Cette feuille est faite d'un substrat d'aluminium sur lequel est déposé une fine couche de fer. Cette dernière est magnétisée par l'application d'un champ magnétique externe. Pour le fer, la magnétisation vaut à saturation environ 2 Tesla [46, 47].

La Figure 4.1 illustre le principe de polarisation/analyse de spin d'UCN. Le couplage des deux états de spin du neutron avec le champ magnétique interne crée deux potentiels $V_F^{\uparrow}$ et $V_F^{\downarrow}$. Dans la gamme d'énergie définie par ces deux valeurs, les neutrons ayant un spin up ($\uparrow$) sont réfléchis alors que ceux avec un spin down ($\downarrow$) sont transmis. Le tableau 4.1 donne les gammes en énergie pour différentes magnétisations dans la couche de fer.

B [T]	$V_F^{\downarrow}$ [neV]	$V_F^{\uparrow}$ [neV]	$v_c^{\downarrow}$ [m/s]	$v_c^{\uparrow}$ [m/s]
1	149.7	270.3	5.4	7.2
1.5	119.6	300.5	4.8	7.6
2	89.4	330.6	4.1	8.0

Table 4.1: Potentiels de Fermi dans le fer magnétisé.

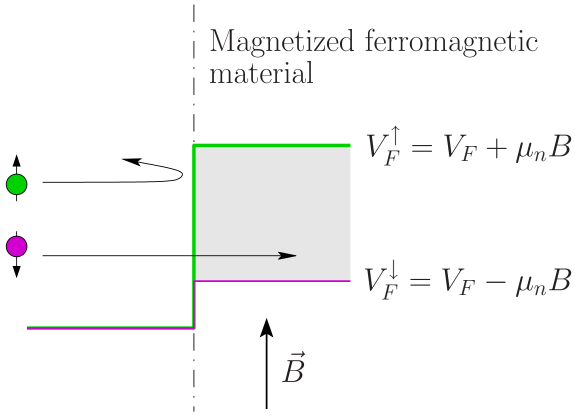

Figure 4.1: Principe de polarisation/analyse par transmission au travers d'une feuille magnétisée. La région colorée représente la gamme d'énergie où le système est efficace puisqu'un seul des deux états de spin peut pénétrer.

4.1.1.2 Mise en œuvre

En pratique, le substrat d'aluminium a une épaisseur entre 13 et 100 μm. Des dépôts de fer avec une épaisseur comprise entre 200 nm et 1 μm ont été testés. Ils ont été réalisés par évaporation (LPC) ou sputtering (PSI). La Figure 4.2 montre une photographie du système de magnétisation des feuilles de polarisation/analyse. Des aimants permanents en AlNiCo ou/et en NdFeB ont été utilisés pour le champ magnétique extérieur. Ils reposent sur un cadre en fer. L'intensité du champ magnétique au centre du sytème a été mesurée à 200-400 Gauss selon la configuration des aimants. Un tel champ d'excitation doit normalement permettre d'atteindre la saturation à l'intérieur du fer [46,47].

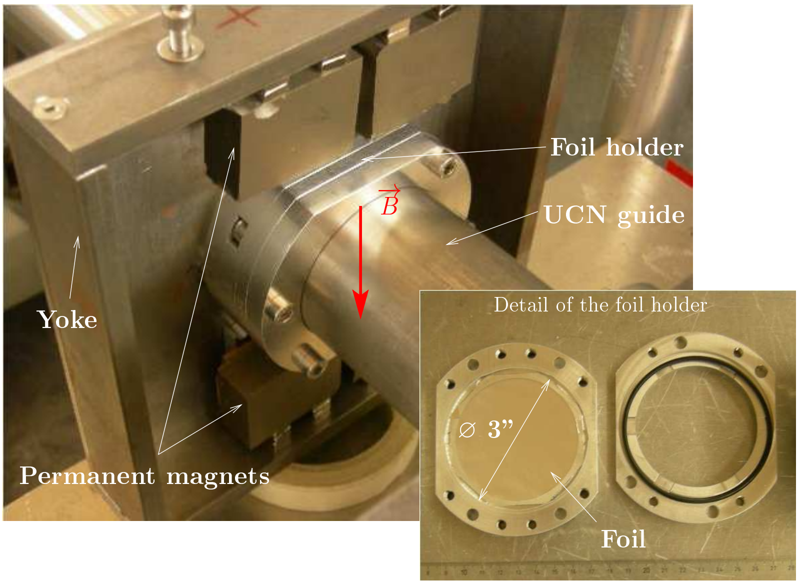

Figure 4.2: Mise en œuvre du système de polarisation/analyse.

4.1.2 Le spin flipper adiabatique

4.1.2.1 Principe

Le principe du spin flipper adiabatique a été étudié à de nombreuses reprises (voir par exemple [48–50]). Il permet de basculer dans l'état de spin opposé les neutrons le traversant avec une efficacité très proche de 100%. Deux champs magnétiques sont nécessaires. Le premier est un gradient statique dont l'intensité diminue/augmente à mesure que le neutron avance dans la zone de spin flip. Le second champ magnétique est perpendiculaire et tourne/oscille à une fréquence choisie pour que la résonance (i.e. l'inversion du spin) intervienne au centre du spin flipper. Si les champs magnétiques sont choisis de telle manière que la condition d'adiabaticité est respectée, alors le spin des neutrons se renverse complètement. Cette condition est validée lorsque la fréquence de précession des neutrons ω_e autour du champ magnétique effectif (somme des deux précédemment définis) est bien supérieure à la fréquence de rotation Ω du champ effectif dans le repère lié au neutron. En général, on définit le paramètre d'adiabaticité η comme le rapport ω_e/Ω. Le modèle sinus-cosinus [50] permet d'en donner une approximation:

$$\eta = \frac{\gamma_n \, L \, A}{\pi \, v}, \tag{4.1.1}$$

où γ_n est le rapport gyromagnétique, A l'amplitude du champ oscillant, L la longueur du spin flipper et v la vitesse du neutron. Les simulations ont montré qu'avec η valant 6, une efficacité de spin flip de 90% pouvait être obtenue. On peut donc considérer que la condition adiabatique est validée pour toute valeur de η supérieure à 6.

4.1.2.2 Mise en œuvre

La Figure 4.3 montre la mise en œvre pratique du spin flipper adiabatique.

Deux options ont été testées pour produire le gradient magnétique. Tout d'abord, une cage dont les barreaux sont remplis d'aimants permanents a été utilisée (voir Fig. 4.3). Le gradient obtenu par ce système est de 0.2 Gauss/cm. La cage est placée de telle manière que le champ est uniforme le long de l'axe vertical, i.e. au-dessus et au-dessous de guide du spin flipper. La seconde option a été d'utiliser le champ de fuite des systèmes de polarisation/analyse [50, 51].

Le champ magnétique oscillant est produit par une bobine de cuivre enroulée autour d'un guide en plastique. Une feuille de cuivre est insérée à l'intérieur pour permettre la transmission des neutrons. Un courant oscillant d'environ 1 A est envoyé dans la bobine. Cela correspond à un champ de 5 Gauss pour une bobine de 100 tours sur 24 cm. Dans ce cas, le calcul de η d'après l'équation (4.1.1) donne 350 pour une vitesse de 20 m/s. Comme $\eta \gg 1$, la condition d'adiabaticité est remplie pour 20 m/s, mais aussi pour toutes les vitesses plus faibles puisque η augmente.

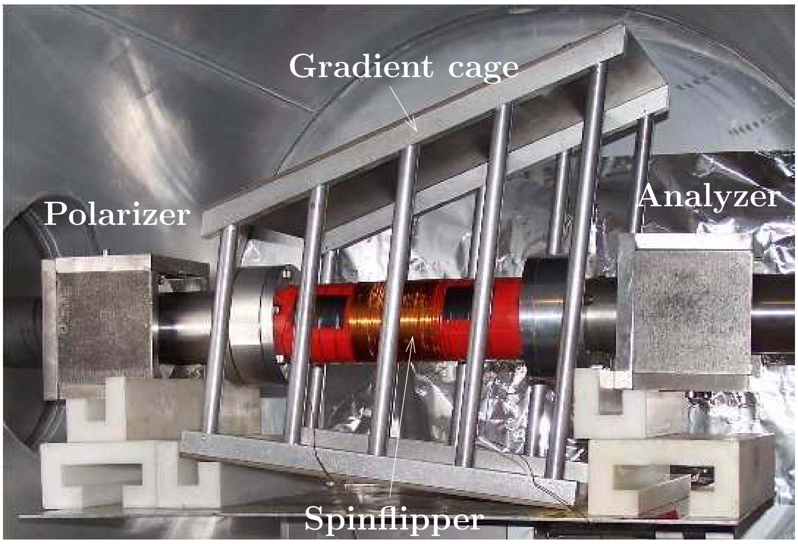

Figure 4.3: Mise en œuvre de l'analyse de spin classique.

4.2 Mesure de l'efficacité de polarisation/analyse en ligne simple

La Figure 4.4 montre le schéma de la mesure. Un chopper est utilisé afin de mesurer le temps de vol. Les neutrons sont polarisés puis traversent la zone de spin flip. Une fois analysés, ils sont enfin détectés. On suppose que le polariseur et l'analyseur sont identiques puisque les systèmes de magnétisation le sont. De plus les feuilles proviennent du même échantillon. Lors du montage, une attention particulière a été apportée pour ne pas avoir de zone de champ magnétique nul entre le polariseur et l'analyseur. Cela pourrait créer des dépolarisations.

La fréquence de résonance du spin flipper est déterminée en variant la fréquence du champ oscillant. Puisque le polariseur et l'analyseur sont traversés par la même composante de spin, le taux de comptage minimum indique qu'un maximum de neutrons voient leur spin basculer. Typiquement, les fréquences de résonance étaient trouvées autour de 15 kHz avec la cage-gradient montée. Comme on l'a vu précédemment, l'efficacité de spin flip est en pratique très proche de 100%. Cela a été vérifié expérimentalement avec nos systèmes (polariseur/analyseur, spin flipper). En faisant cette approximation, on arrive à une expression simple pour l'efficacité de polarisation [51]. Elle est représentée par l'asymétrie suivante:

$$p \approx \frac{I_0 - I_1}{I_0 + I_1}. \tag{4.2.1}$$

où I_0 (I_1) est l'intensité du faisceau mesurée lorsque le spin flipper est éteint (alimenté).

La Figure 4.5(a) montre les distributions de vitesse obtenues avec le montage de la Fig. 4.4. Deux mesures ont été réalisées avec le spin flipper éteint et alimenté. Pour ce dernier cas, une coupure est clairement visible autour de 7 m/s. En dessous,

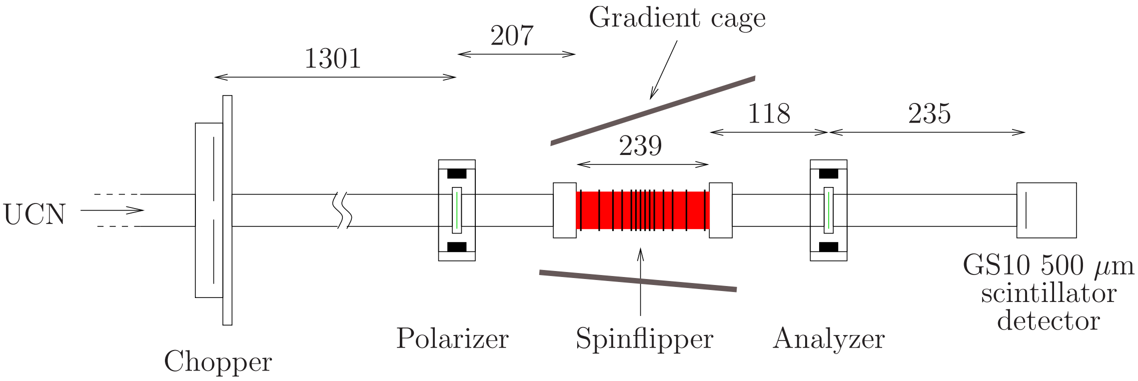

Figure 4.4: Schéma de l'analyse de spin utilisé pour la mesure de l'efficacité de polarisation. Les distance sont en mm.

aucun UCN n'est détecté vu que le spin flipper est activé. La Figure 4.5(b) trace l'asymétrie d'après l'équation (4.2.1) en fonction de la vitesse longitudinale. Pour des neutrons ayant des vitesses inférieures à 7 m/s, sa valeur est supérieure à 90%.

La gamme de vitesse dans laquelle l'analyse de spin peut être effectuée est liée à l'intensité de la magnétisation à l'intérieur des feuilles de polarisation/analyse. On a vu que pour le fer, cette valeur est de 2 Tesla. Elle correspond à une gamme de vitesse comprise entre 4.1 et 8 m/s (voir le tableau 4.1). Ici, l'intervalle de vitesse est plus petit et pourrait être dû à une saturation incomplète dans les feuilles.

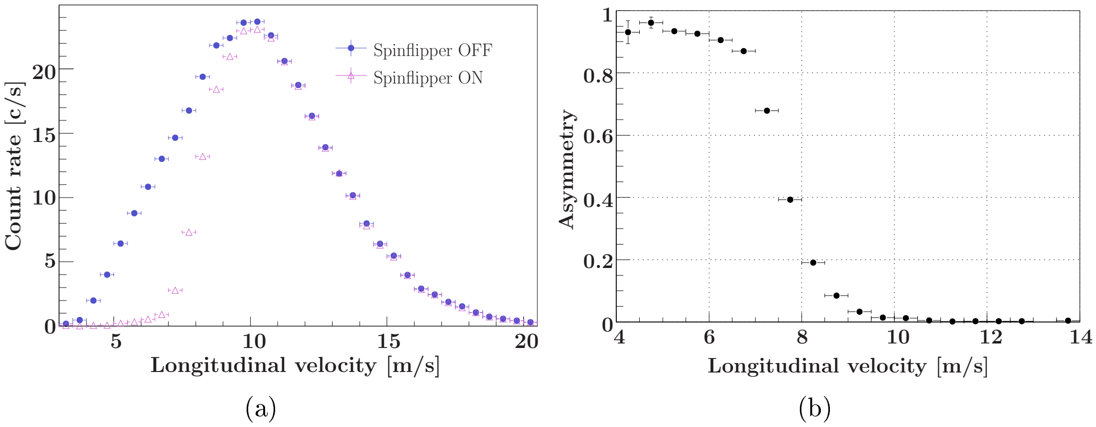

(a) (b)

Figure 4.5: Résultats d'une mesure de polarisation réalisée sur la ligne EDM à ILL/PF2.

4.3 Analyse simultanée des deux composantes de spin

Deux systèmes d'analyse simultanée des deux composantes de spin du neutron ont été testés sur la ligne TEST. Leur transmission ainsi que leur efficacité d'analyse de spin ont été mesurées.

4.3.1 Motivations et principe

La motivation principale pour le développement d'un système d'analyse simultanée est de permettre de compter plus de neutrons que dans la méthode d'analyse séquentielle utilisée jusqu'à présent sur le spectromètre EDM. L'idée est notamment de s'affranchir des pertes neutrons qui existent pour cette dernière lors des phases de comptage de chaque composante de spin.

La Figure 4.6 montre deux systèmes simultanés que l'on a placé sous la chambre de stockage du spectromètre EDM. Pour simplifier, nous appellerons ces systèmes "Y" d'après leur forme de "Y" renversé. Chaque "bras" de ce Y constitue un système d'analyse complet muni d'un spin flipper, d'un analyseur et d'un détecteur. Supposons que l'on active l'un des spin flippers en gardant l'autre éteint. De plus, considérons un neutron spin down entrant dans le bras où le spin flipper est alimenté. Au niveau de l'analyseur, le neutron arrive dans l'état up. Il est alors réfléchi et son spin est à nouveau basculé. l'UCN retourne alors soit dans le guide d'arrivée, soit dans l'autre bras. Lorsqu'il réussit à entrer dans le bras où le spin flipper est éteint, il est alors analysé puis détecté.

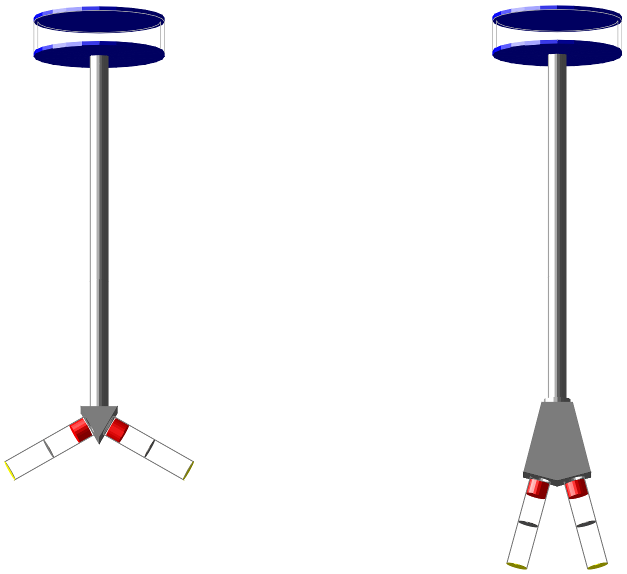

(a) Géométrie EDM avec le Y_{120} (b) Géométrie EDM avec le Y_{30}

Figure 4.6: Systèmes d'analyse simultanée associés à la géométrie EDM (position verticale). (a) Y avec un angle de 120° entre les deux bras et (b) avec un angle de 30°.

4.3.2 Mise en œuvre du système Y

La Figure 4.7 montre les deux systèmes d'analyse simultanée de spin en position horizontale.

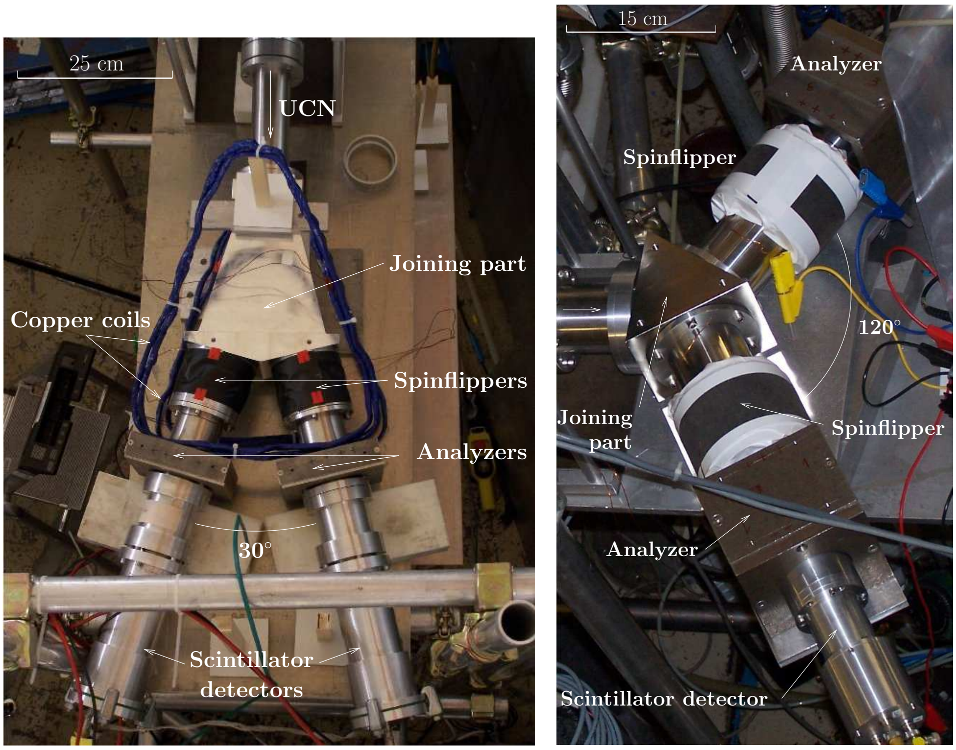

(a) Y_{30} (b) Y_{120}

Figure 4.7: Mise en œuvre des systèmes Y.

Ils sont faits en acier inoxydable (316L). Puisque c'est un matériau magnétique, des feuilles de cuivre polies à la main sont insérées dans les deux systèmes dans les parties guidant les UCN. Les feuilles d'analyse sont faites d'un support de 100 μm d'aluminium (Goodfellow, pureté 99%) sur lequel est déposée par sputtering une couche de 200 nm de fer.

La longueur effective des spin flippers a été réduite à 5 cm. La distance entre les spin flippers et les feuilles d'analyse est de 10 cm. Celle entre les analyseurs et les détecteurs est de 14 cm. La longueur totale de chaque bras (depuis la partie centrale jusqu'au détecteur) vaut 40 cm.

Les détecteurs utilisés dans les deux bras sont des scintillateurs GS10. Ils ont une épaisseur de 500 μm pour le bras droit et 100 μm pour le gauche(1).

4.3.3 Tests de transmission

La transmission des Y peut être mesurée en réalisant deux expériences. La première est une mesure de référence sans Y que l'on fait pour chaque détecteur. La seconde est réalisée avec Y. Aucune feuille n'est placée dans le faisceau. Les spin flippers ne sont pas utilisés ici (ils sont inactifs).

Puisque les deux bras sont identiques, seul le taux de comptage mesuré avec le

---

(1) Au moment de ces tests, nous ne disposions pas de deux détecteurs identiques.

bras gauche (GS10 100 μm) est utilisé. La Figure 4.8(a) montre les distributions de vitesse pour le bras gauche mesurée avec les systèmes Y_{30} et Y_{120}. La mesure de référence faite avec le GS10 100 μm est aussi tracée. On constate que la distribution de vitesse obtenue avec le Y_{120} est très fortement coupée. Les neutrons possédant une vitesse longitudinale au-delà de 10 m/s ne sont pas transmis. Ils sont perdus en majorité dans la partie centrale joignant les deux bras.

La transmission est calculée en divisant le spectre en vitesse du bras gauche mesuré avec le Y_{30} et le Y_{120} par la distribution de référence. Ceci impose de multiplier par 2 le taux de comptage du bras gauche puisque le détecteur de droite n'est pas considéré$^{(2)}$. La Figure 4.8(b) représente les courbes de transmission des Y. La transmission du Y_{30} est d'environ 47% entre 4 et 11 m/s, puis elle augmente jusqu'à 60% entre 12 et 15 m/s. Une telle géométrie est plus intéressante pour conserver les UCN avec une grande vitesse longitudinale grâce au faible angle entre les deux bras. Au contraire, le Y_{120} tue tous les UCN ayant une vitesse longitudinale entre 10 m/s et 15 m/s. Sa transmission est inférieure à 20% pour des vitesses inférieures à 10 m/s. Celle du Y_{30} est dans tous les cas meilleure.

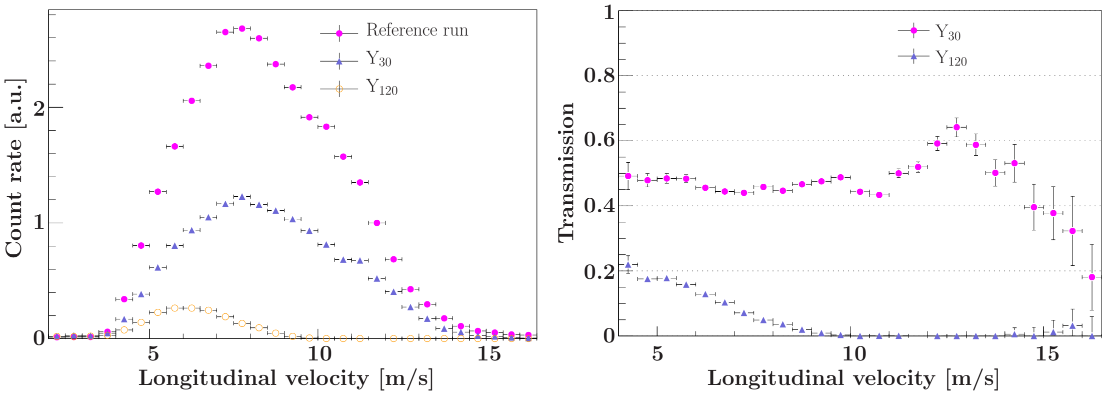

(a) (b)

Figure 4.8: Résultats des mesures de transmission pour les systèmes Y. La distribution de vitesse de référence mesurée avec le GS10 100 μm est donnée. Celles des Y ont été multipliées par 2 pour pouvoir les comparer directement à la mesure de référence.

4.3.4 Tests d'analyse de spin

Pour ces mesures, on ajoute un polariseur avant les Y et deux analyseurs. Un champ magnétique statique est créé entre le polariseur et les analyseurs afin de maintenir la polarisation. Le gradient magnétique est produit par le champ de fuite des systèmes de magnétisation des analyseurs. Seul le Y_{30} a été testé ici étant donné la très faible transmission du Y_{120} sur la ligne TEST.

---

(2) Une autre méthode serait de sommer les taux des deux bras et de diviser le résultat par la moyenne des runs de référence obtenus pour chaque détecteur. La transmission calculée avec cette méthode est la même que celle déterminée à partir de la première méthode.

La Figure 4.7(a) présentée plus haut montre le Y_{30} en fonctionnement. Deux runs sont réalisés: pour le run 1, le spin flipper de gauche est activé et le droit est éteint; pour le run 2, la configuration opposée des flippers est prise. Les asymétries (cf. équation (4.2.1)) de chaque bras peuvent ainsi être extraites pour estimer l'efficacité d'analyse du Y.

La Figure 4.9 montre les spectres en vitesse mesurés pour chaque bras avec leur spin flipper respectif activé ou éteint. Le détecteur de droite (GS10 500 μm) est plus efficace à haute vitesse que celui de gauche (GS10 100 μm). Par conséquent, plus d'UCN sont détectés à hautes vitesses (specialement au-dessus de 9 m/s).

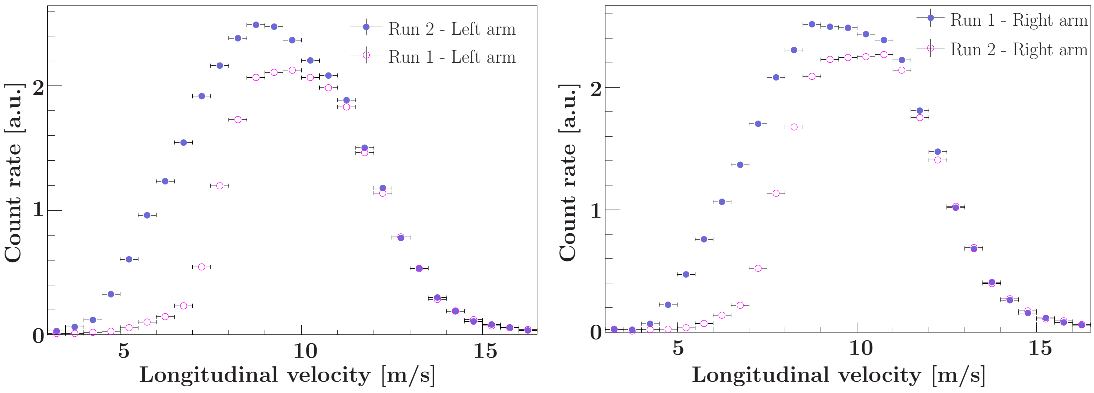

(a) Bras gauche

(b) Bras droit

Figure 4.9: Distributions de vitesse mesurées avec le Y_{30}.

Les asymétries correspondantes sont présentées sur la Fig. 4.10. Elles sont similaires entre elles avec une valeur autour de 80% pour des vitesses inférieures à 7 m/s. Durant l'expérience, cette valeur n'a pas pu être améliorée malgré le soin apporté

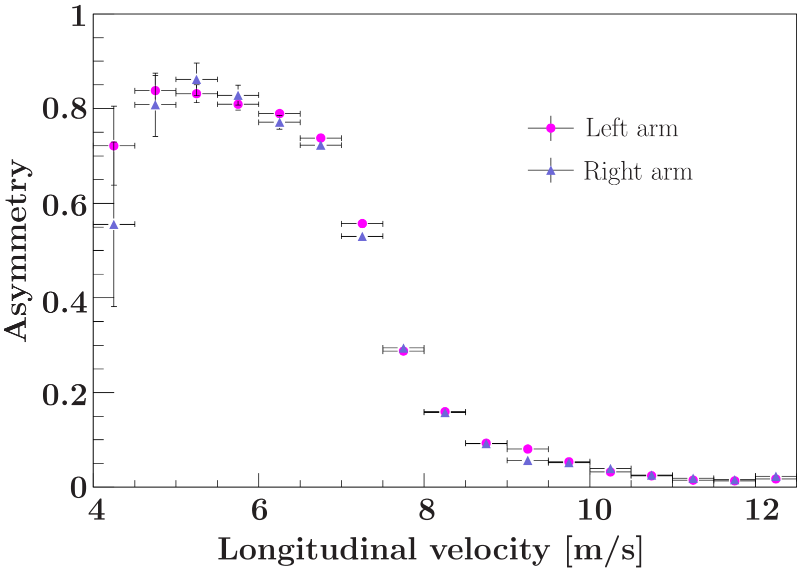

Figure 4.10: Efficacités de polarisation pour chaque bras mesurées avec le Y_{30}.

au montage. Des valeurs identiques ont été mesurées en remplaçant le Y par un de ces bras. La configuration était alors celle de la Fig. 4.4. Aucune amélioration n'a été possible dans ces tests non plus.

4.4 Conclusions

Les résultats principaux concernant l'analyse de spin ont été présentés. Les polariseurs/analyseurs ainsi que spin flippers ont prouvé leur efficacité. On a vu que mesurer une efficacité de polarisation/analyse autour de 90% est possible.

Les systèmes d'analyse simultanée de spin ont été testés sur la ligne TEST à ILL/PF2. La surface interne des guides a été réalisée avec des feuilles de cuivre. La transmission du Y_{30} a été mesurée autour de 50% alors que celle du Y_{120} est inférieure à 20%. La mesure simultanée des deux états de spin a été réalisée avec le Y_{30}. Les deux bras ont une efficacité d'analyse de 80%.

Conclusions et perspectives

Le moment dipolaire électrique du neutron d_n a joué un rôle crucial dans l'étude des symétries P et CP/T pour les particules élémentaires. La limite supérieure sur d_n a diminué continuellement ces soixante dernières années. Cela a permis de contraindre, voire d'écarter, de nombreuses extensions possibles du Modèle Standard de la physique des particules. Le nouveau projet de PSI propose d'améliorer la limite expérimentale sur d_n à 10^{-28} $e \cdot$cm. Ce sera possible grâce à la nouvelle source de neutron de spallation. La densité d'UCN attendue est d'environ deux ordres de grandeur supérieure à celle de l'ILL dans la chambre de stockage du spectromètre EDM. Des détecteurs rapides seront donc nécessaires.

Trois types de détecteurs ont été testés à l'ILL durant cette thèse: le détecteur à gaz ^{3}He, le cascade-U et des scintillateurs dopés au ^{6}Li (GSx). Parmi les scintillateurs, le GS10 est compétitif avec le détecteur à gaz ^{3}He lorsqu'il est testé sous le spectromètre EDM. En effet, tandis que le GS10 500 μm est d'une efficacité comparable à l'^{3}He, un GS10 de 100 μm est environ 10% moins efficace que ce dernier sous le spectromètre. Le GS10 reste néanmoins plus sensible aux gammas d'un ordre de grandeur environ que les détecteurs à gaz. Un système de double scintillateur GS3/GS20 a permis d'améliorer la séparation entre signaux UCN et gammas. La proportion d'événements de bords a été diminuée d'un ordre de grandeur par rapport au GS10 100 μm. Le GS3/GS20 reste 20% moins efficace que le détecteur à gaz ^{3}He lorsque la mesure est effectuée sous le spectromètre EDM. Des tests ont montré que cette différence d'efficacité serait due à la transmission au travers du GS3. Le cascade-U a été testé pour trois épaisseurs de ^{10}B sur la face d'entrée du détecteur: 50, 200 et 800 nm. Celle de 200 nm a permis d'atteindre une efficacité de 80% par rapport au GS10 500 μm. Les simulations Monte-Carlo ont montré un plafonnement à 82% de l'efficacité absolue. Les épaisseurs optimales de ^{10}B ont été calculées dans la gamme 260-300 nm.

Les tests expérimentaux sur l'analyse de spin ont montré qu'une efficacité de polarisation/analyse de 90% peut être atteinte avec nos systèmes d'aimantation. Le spin flipper a été mesuré avec une efficacité compatible avec 100%. Concernant le système d'analyse simultanée de spin, la transmission du Y_{30} a été mesurée autour de 50% alors que pour le Y_{120}, elle est inférieure à 20%. Une mesure d'analyse simultanée a été effectuée avec le Y_{30} et a montré que les deux bras avaient la même efficacité d'analyse de spin de 80%.

Un système de détection consistant en plusieurs PM associés à des ensembles double scintillateur est actuellement en cours de développement au LPC. Afin d'améliorer la collection de la lumière, chaque double scintillateur sera assemblé par adhésion moléculaire.

Le système d'analyse simultanée de spin requiert plusieurs améliorations. La surface interne des parties guidant les neutrons doit être recouverte d'un matériau (non-magnétique) avec un haut potentiel de Fermi. Par exemple, un revêtement fait de NiMo permettrait d'obtenir une vitesse critique autour de 6.5 m/s. L'efficacité d'analyse de spin de 80% doit être améliorée. Enfin, des tests doivent être réalisés à PSI sous le spectromètre EDM. Une comparaison entre les deux méthodes d'analyse de spin (séquentielle/simultanée) pourrait ainsi être faite.

Part II

Technical details...in english

Chapter 5

Introduction

Particle electric dipole moments (EDM) are sensitive probes in the search for time reversal symmetry violation (T-violation). For the neutron EDM d_n, the experimental sensitivity has improved by a factor of 10^6 over the last fifty years. The non-existence of the EDM at the tested level has ruled out many of the possible extensions to the Standard Model of particle physics. The most recent limit on d_n has been measured at the Institut Laue-Langevin (ILL). An in-vacuum room-temperature Ramsey resonance experiment was used with stored ultracold neutrons (UCN). The measurement set an upper limit of $|d_n| < 2.9 \cdot 10^{-26}\ e \cdot \mathrm{cm}$.

This thesis is part of a new project which goal is to push the experimental limit on d_n down to a level of $10^{-28}\ e \cdot \mathrm{cm}$. The experiment will be performed at the Paul Scherrer Institute (PSI) using a new version of the room-temperature experiment of ILL. The higher experimental sensitivity will be obtained with a better control of systematic effects and a higher UCN density. The latter will be provided by the new spallation source at PSI. The expected gain is about two orders of magnitude with respect to the UCN density at ILL within the UCN storage chamber. Fast UCN detectors are therefore required.

The work presented here has consisted in comparing UCN detectors focusing on their efficiency of detection and their background sensitivity. Three kind of detectors have been tested at ILL: the cascade-U detector (GEM-type), the standard ^{3}He gas detector, and the ^{6}Li-doped glass scintillators. Moreover, a new system of simultaneous spin analysis is presented. It consists of two independent detection systems (arms) which are each made of an adiabatic spin flipper, a spin analyzer, and a detector. The arms detect opposite spin components, allowing the simultaneous counting of both neutron spin orientations.

The introductive part of this document presents the motivations for the neutron EDM search (chapter 6). The principle of the RAL-ILL-Sussex experiment and an overview of the ongoing projects searching for a neutron EDM are given. The chapter 7 presents the UCN source of ILL and PSI and the basic of the UCN properties.

The second part concerns the UCN detectors. Chapter 8 presents their characteristics in connection with the measurement of the neutron EDM. In chapter 9, Monte-Carlo simulations of detectors are detailed focusing on the energy deposition and the detection efficiency. The chapter 10 reports measurements performed at ILL where detectors have been compared with respect to their detection efficiency and their sensitivity to background.

The last part is devoted to the study of spin analyzing systems. Chapter 11 details the principle of UCN polarization as well as that of the adiabatic spin flipper. In chapter 12, systems for sequential and simultaneous spin analysis are compared through Monte-Carlo simulations. Both are considered below the EDM spectrometer. The UCN losses and the analyzing efficiencies are discussed. Chapter 13 reports experimental results about the performances of the devices used for UCN spin analysis (i.e. polarizer, analyzer and spin flipper). The tests of two systems for simultaneous spin analysis are finally described.

Chapter 6

The neutron EDM

6.1 Introduction

6.1.1 Early history and motivations

The question of parity violation

In 1950, Purcell and Ramsey argued on the possible existence of electric dipole moment (EDM) for elementary particles [1] indicating that it should be checked experimentally. They also underlined that the existence of a particle EDM would demonstrate the violation of the parity symmetry (P). Indeed, since a non-degenerate quantum system can only be characterized in its rest frame by its spin $\vec{s}$, the electric dipole moment $\vec{d}$ must be proportional to $\vec{s}$ [2]. When an electric field $\vec{E}$ is applied, the interaction between $\vec{d}$ and $\vec{E}$ appears in the Hamiltonian as $-\vec{d}\cdot\vec{E}$. Under P transformation (inversion of space coordinates), $\vec{d}\rightarrow\vec{d}$ and $\vec{E}\rightarrow-\vec{E}$ such that the term $-\vec{d}\cdot\vec{E}$ changes sign. Thus any non-zero value of the EDM would indicate P violation. As a result, Purcell and Ramsey decided with J. H. Smith to search for the electric dipole moment of the neutron [3]. This particle is an efficient tool for such a study since it has no electric charge and then it is not accelerated out of the measurement region under a strong electric field. Although the result of this experiment was consistent with zero ($d_n = (-0.1\pm 2.4)\cdot 10^{-26} e\cdot\mathrm{cm}$ [3]), the signal for further decisive experiments was sent.

In 1956, Lee and Yang proposed the non-conservation of parity in the weak interaction in order to explain the famous $\theta-\tau$ mesons puzzle [52]. They also mentioned possible experiments which would reveal P violation. One year later, parity non-conservation was observed by Wu *et al.* in the weak interaction thanks to the measurement of an asymmetry in the angular distribution of electrons coming out of ^{60}Co polarized nuclei [4]. As a consequence, the argument that parity symmetry would prevent nuclei and elementary particles to have an EDM was ruled out.

The search for CP violation

The existence of particles EDM can also be considered from the point of view of the time-reversal symmetry T. As explained for P symmetry, one can see that the

Hamiltonian $-\vec{d}\cdot\vec{E}$ changes sign under T since $\vec{d} \to -\vec{d}$ and $\vec{E} \to \vec{E}$. Thus, T violation is also necessary for particles EDM to exist.

Furthermore in 1954, Lüders formulated his famous CPT theorem — also known as Pauli-Lüders theorem — which states the invariance of physics law under charge conjugation C, parity P and time-reversal T operations [5,6]. This theorem implies particularly that T symmetry is equivalent to CP symmetry. Therefore the question of the particles EDM existence is directly linked to that of CP violation.

As he did about the arguments in favor of P symmetry, Ramsey repeated for CP/T symmetry: "...while such arguments are appealing from the point of view of symmetry, they are not necessarily valid" [7]. Thus this question of CP/T symmetry could only be answered experimentally and the search for a neutron EDM would provide a very sensitive probe.

Historically, CP violation was observed for the first time in 1964 by Christenson *et al.* in the K^0 meson decay [8]. Moreover in 1967, CP violation appeared to be one of the three necessary conditions introduced by Sakharov — with the non-conservation of the baryon number and the breaking of the initial thermal equilibrium — in order to explain the dominance of matter over antimatter in our universe [9]. Today, the measured sources of CP violation are too small to explain the matter-antimatter asymmetry observed in the universe. Additional sources are needed and may be found with the measurement of the neutron EDM.

Theoretical impact

The current model used to describe the particles physics is the Standard Model (SM) which embeds both quantum chromodynamic (QCD) and electroweak theories. Each of these contains CP-violating terms: the phase δ from the electroweak sector — which appears in the Cabibbo-Kobayashi-Maskawa (CKM) quark mixing matrix — and the QCD angle θ. The theoretical predictions from the phase δ lead to a neutron EDM d_n of about $10^{-32} e \cdot \mathrm{cm}$ [2]. In contrast to δ, the QCD angle θ is an arbitrary dimensionless parameter which has to be tuned. Thanks to the current experimental upper bound on d_n: $|d_n| \lesssim 10^{-26} e \cdot \mathrm{cm}$ [10], θ is actually fine-tuned to less than 10^{-9} [11]. This so unexpectedly small value is known as the *Strong CP problem* which is not satisfactorily solved within the framework of the Standard Model.

Various extensions of the SM have been introduced with more parameters and so more opportunities for CP-violating phases. Consequently, they predict larger values for d_n than the SM, typically in the range accessible by the experiments. For example, left-right symmetric models, in which right-handed W_R and Z' bosons are added to the usual particles of the SM, predict nEDM in the range $10^{26\pm1} e \cdot \mathrm{cm}$ [12]. In supersymmetric models, every particle is associated with a superpartner whose spin differs by 1/2 (i.e., the number of particles is doubled with respect to the SM). Their predictions gives nEDM in the range $10^{-25} - 10^{-28} e \cdot \mathrm{cm}$ [13].

6.1.2 The experimental evolution of the limit on d_n

The experimental upper limit on d_n has decreased continuously since 1950 (Fig. 6.1). Most of the nEDM experiments have used the same measurement principle, namely the Ramsey's method of separated oscillatory fields [14]. They can be divided into two types: the *beam* and the *storage* experiments. The first use thermal neutron beams passing through the measurement region [3,15–19], and the second, ultracold neutrons (UCN) (cf. chapter 7) which are confined in storage chambers [10,20–27]. Since the mean velocity of the neutrons tends to zero in storage experiments, it has enabled to almost eliminate a critical systematic effect — the so-called $\vec{v} \times \vec{E}$ effect — which limits the sensitivity of the "beam" experiments. The best result achieved so far was published in 2006 by the RAL-Sussex-ILL collaboration and gives an upper limit on the neutron EDM of $|d_n| < 2.9 \cdot 10^{-26} e \cdot \mathrm{cm}$ (90% C.L.) [10]. We will describe the RAL-Sussex-ILL apparatus and discuss some of the systematics effects in section 6.2.

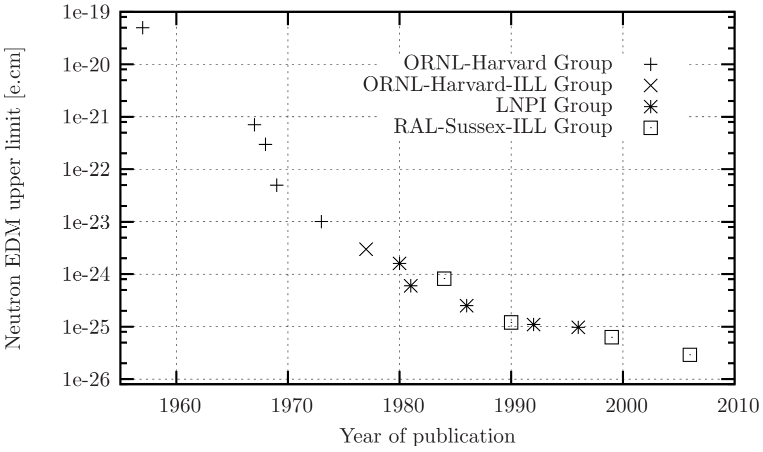

Figure 6.1: History of the published nEDM measurements indicating the different institutions involved [3,10,15–27].

6.2 The RAL-Sussex-ILL experiment

6.2.1 The principle of the nEDM measurement

UCN are stored in a region where parallel static magnetic $\vec{B}_0$ and electric $\vec{E}$ fields are applied. The neutron magnetic dipole moment $\vec{\mu}_n$ interacts with $\vec{B}_0$ leading to an interaction energy of $-\vec{\mu}_n \cdot \vec{B}_0$. Similarly, the interaction between the EDM $\vec{d}_n$ and the electric field $\vec{E}$ can be written as $-\vec{d}_n \cdot \vec{E}$ such that the Hamiltonian of both interactions is given by:

$$H = -\vec{\mu}_n \cdot \vec{B}_0 - \vec{d}_n \cdot \vec{E}. \tag{6.2.1}$$

As the neutron is a non-degenerate quantum mechanical system, its electric dipole moment is aligned with the spin $\vec{S}$ such that one can now write the Hamiltonian as:

$$H = -(\mu_n \vec{B}_0 + d_n \vec{E}) \cdot \frac{\vec{S}}{S}, \tag{6.2.2}$$

where $S = 1/2$.

Figure 6.2 shows the scheme of the energy levels of a neutron interacting with $\vec{E}$ and $\vec{B}_0$ fields. Two directions of the electric field relative to $\vec{B}_0$ are drawn (i.e. parallel and antiparallel). The split between the neutron energy levels is given by:

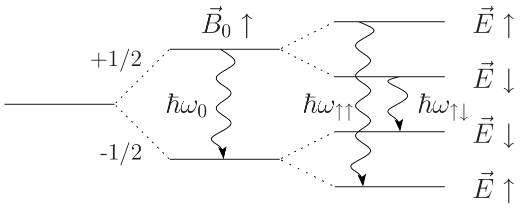

Figure 6.2: Energy levels of neutrons in a static magnetic field $\vec{B}_0$ and for the two directions of an electric field $\vec{E}$ relative to $\vec{B}_0$. ω_0 is the Larmor angular frequency.

$$\hbar\omega_n = -2\mu_n B_0 \pm 2 d_n E, \tag{6.2.3}$$

where ω_n is the precession angular frequency of the neutron. Depending on the relative orientations of the electric and magnetic fields (i.e. parallel $\uparrow\uparrow$ or antiparallel $\uparrow\downarrow$), this frequency takes two values which are written $\omega_n^{\uparrow\uparrow}$ ($-$ sign in 6.2.3) or $\omega_n^{\uparrow\downarrow}$ ($+$ sign in 6.2.3). Differentiating these two values leads to the nEDM measurement through the relation:

$$\delta\omega = \omega_n^{\uparrow\uparrow} - \omega_n^{\uparrow\downarrow} = -\frac{4 d_n E}{\hbar}. \tag{6.2.4}$$

Therefore the measurement of the neutron electric dipole moment d_n is equivalent to the determination of a slight frequency shift between the two fields configurations $\vec{B}_0 \uparrow\uparrow \vec{E}$ and $\vec{B}_0 \uparrow\downarrow \vec{E}$. For example, $d_n = 1 \cdot 10^{-26} e \cdot \mathrm{cm}$ is equivalent to a precession frequency shift of about 0.1μHz.

6.2.2 The Measurement

Description of the apparatus and measurement procedure

A scheme of the apparatus is shown in Fig. 6.3. Ultracold neutrons, provided by the ILL/PF2 turbine, are polarized through a thin magnetized iron foil (see chapter 11). They fill a 20-liter storage volume delimited by an insulating quartz cylinder and the upper and lower electrodes. A coil wounded around the vacuum vessel creates a uniform vertical magnetic field B_0 of ~1 μT which is protected from external magnetic perturbations by a four-layer mu-metal shield (~ 10^4 shielding factor [27]). The strong electric field (~10 kV/cm) is produced by applying high voltage (positive or negative) on the upper electrode whereas the lower one remains grounded. After a

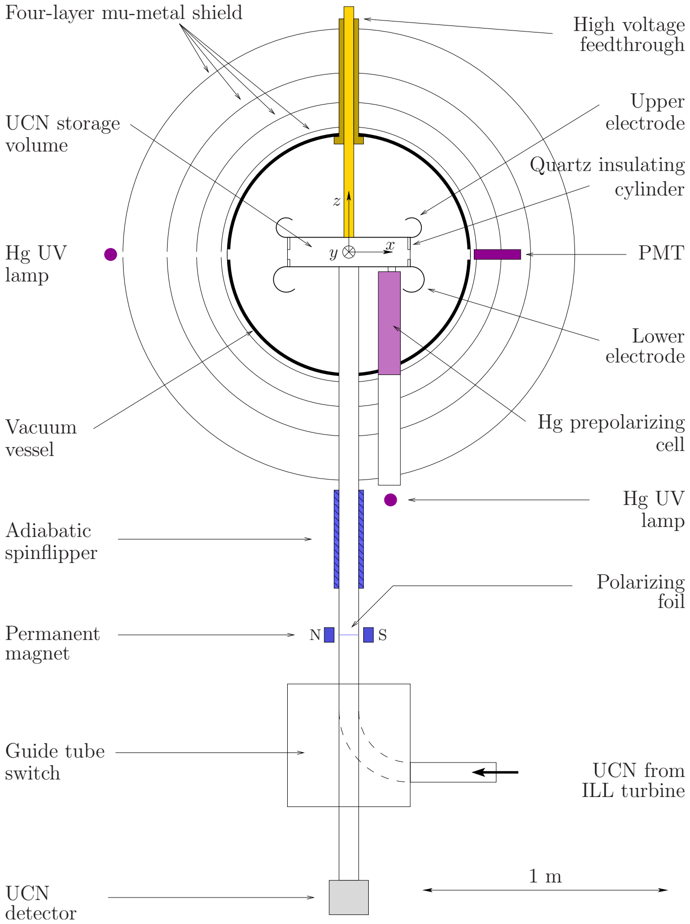

Figure 6.3: Scheme of the RAL-Sussex-ILL experiment at ILL/PF2.

filling of about 40 s, the entrance door of the storage chamber is closed. Then during about hundred seconds, UCN are kept in the storage volume. The neutron resonant frequency is measured by the so-called Ramsey magnetic resonance technique of separated oscillating fields [14] (see below).

At the end of the Ramsey measurement, the entrance door of the chamber is open and UCN fall down. The polarizing foil is able to analyze only one spin state. Thus, the use of a spin flipper coil (see chapter 11) enables to select which of the spin states is going to be analyzed by this foil. Practically, the spin flipper is off during the first 8 seconds after the chamber opening, then it is switched on for the next 20 seconds and the counting sequence ends with 12 seconds with spin flipper off.

Two numbers of counts can be registered as a function of the spin flipper state. In the following, they will be denoted as N_+ and N_-. The $+$ sign refers to the spin state which is selected after the first passage of the neutrons through the polarizing foil.

The principle of the Ramsey method

The Ramsey magnetic resonance technique is applied to UCN polarized along $\vec{B}_0$, i.e. along the z axis. It can be summarized through the following steps:

1. UCN are submitted to an oscillating magnetic field B_{RF} during a short time τ. This field beats in the xy plane at a frequency ω very close to the neutron Larmor frequency ω_0. At the resonance ($\omega = \omega_0$), the duration τ and the strength B_{RF} follow the relation $-\gamma_n B_{RF}\tau = \pi/2$, where γ_n is the neutron gyromagnetic ratio. The neutron spin then rotates by $\pi/2$ into the xy plane. This is called a $\pi/2$-pulse;
2. At the end of the pulse, the spin precess freely during a period $T \sim 100$ s. They rotate in the xy plane about the static magnetic field $\vec{B}_0$;
3. Another identical $\pi/2$-pulse, coherent with the first one, is then applied. If the frequency of this oscillating pulse is the same than the neutron precession frequency, then they rotate a further $\pi/2$ radians out of the xy plane into the direction antiparallel to the magnetic field $\vec{B}_0$.

In the nEDM experiment, the UCN also feel a strong electric field during the whole Ramsey sequence. If the neutron EDM exists, its interaction with the electric field will produce a slight frequency change $\Delta\omega = \omega - \omega_0$. It will be integrated during the whole precession time T to give a total phase shift that equals to $\Delta\omega T$. As a consequence, the second RF pulse will not be as efficient to rotate the spins as in the on-resonance case. For example, a phase difference of π would rotate back the spins to their initial orientation. This can be further seen in Fig. 6.4 which shows the evolution of the spin up counts N_+ as a function of the RF field frequency. One can see that, at resonance, a maximum of neutrons are flipped so that N_+ is minimal and N_- maximal; if one looks a bit after, N_+ has a maximum for a phase difference of π (in fact, this is true for a phase shift of $(2k+1)\pi$).

The determination of the resonant frequency

The usual experimental procedure to determine the resonant frequency is to work at the maximum of sensitivity of the Ramsey pattern, that is for $\Delta\omega T = \pi/2$. At these points, a small frequency change will imply a large variation in the difference of the neutron counts for the two orientations of the electric field. Figure 6.5 shows a zoomed picture of the Ramsey patterns for N_+ and N_- about the resonant frequency. The blue points indicates the working conditions.

The central valley can be approximated by [43, 53]:

$$N_\pm(\Delta\omega) = \frac{N_0}{2}(1 \mp \alpha\cos(\Delta\omega T)), \tag{6.2.5}$$

where N_0 is the total number of detected neutrons ($N_0 = N_+(\Delta\omega) + N_-(\Delta\omega)$). α is the visibility of the central fringe defined as:

$$\alpha = \frac{N_{max} - N_{min}}{N_{max} + N_{min}}. \tag{6.2.6}$$

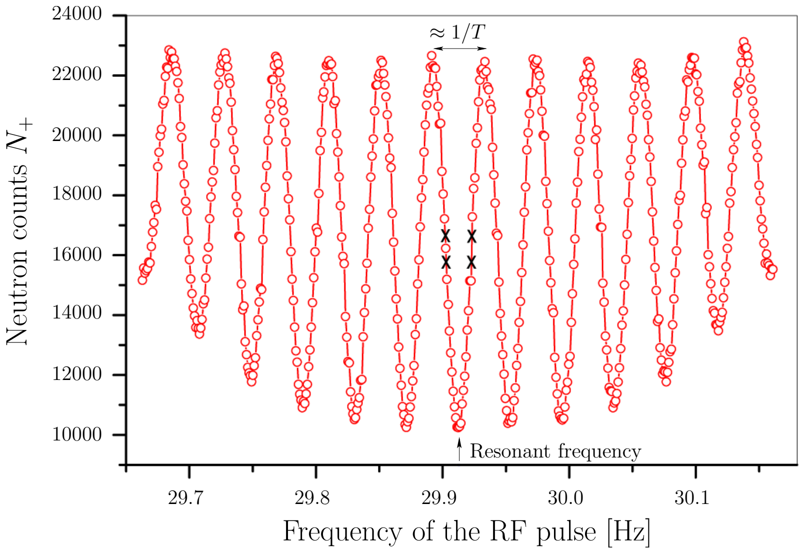

Figure 6.4: Ramsey pattern from the RAL-Sussex-ILL apparatus for the N_+ number of counts [27].

α is representative of the polarization efficiency [30]. The minimum value N_{min} in Fig. 6.4 is greater than zero due to the polarizer inefficiency and/or depolarization effects during the whole measurement.

In order to relate the neutron EDM d_n to what we really measure during the experiment (i.e. the numbers of detected neutron N_+ and N_-), one can express from equation (6.2.5) the shift $\Delta\omega$ as a function of the difference $\Delta N = N_+ - N_-$:

$$\Delta\omega \approx \frac{\pi}{2T} + \frac{\Delta N}{N_0 \alpha T}. \tag{6.2.7}$$

The statistics here corresponds to two Ramsey cycles, one with $B \uparrow\uparrow E$ and another with $B \uparrow\downarrow E$. Assuming that the other conditions of these measurements are exactly the same — i.e. same number of neutrons N_0, same α and precession time T — then one obtains at resonance:

$$\Delta\omega^{\uparrow\uparrow} - \Delta\omega^{\uparrow\downarrow} \approx \frac{\Delta N^{\uparrow\uparrow} - \Delta N^{\uparrow\downarrow}}{N_0 \alpha T}, \tag{6.2.8}$$

which is nothing else than the frequency change $\delta\omega$ of equation 6.2.4. Thus d_n can be written as [31]:

$$d_n \approx -\frac{\hbar(\Delta N^{\uparrow\uparrow} - \Delta N^{\uparrow\downarrow})}{4\alpha E T N_0}. \tag{6.2.9}$$

6.2.3 Statistical uncertainty and systematic effects

Statistical sensitivity

From Eq. 6.2.9, one can derive the uncertainty σ_{d_n} on the nEDM due to the counting statistics [31]:

$$\sigma_{d_n} \approx \frac{\hbar}{2\alpha E T \sqrt{N_0}}, \tag{6.2.10}$$

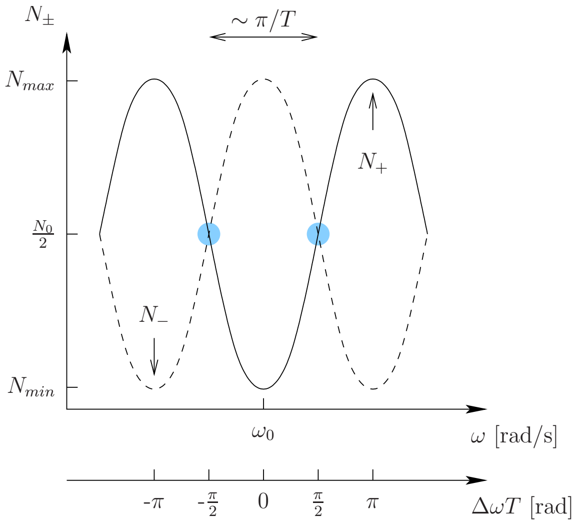

Figure 6.5: Zoom-in of the central fringe of the Ramsey pattern. The points indicates the working conditions for the determination of the resonant frequency ω_0.

The typical values of the parameters in equation (6.2.10) were $\alpha = 0.6$, $E = 10$ kV/cm, $T = 130$ s and $N_0 = 14000$ neutrons per cycle of about 210 s. This leads to a statistical uncertainty of about $2 \cdot 10^{-25} e \cdot \text{cm}$ per day [31].

All these parameters may be essentially improved. The statistical sensitivity is increased if more UCN are detected [31]. This motivates the ongoing construction of new UCN sources. Moreover the visibility α needs to be as much as possible close to 1. This means more efficient ways to polarize, maintain and analyse the neutron spin. Then one could also increase the electric field, but care must be taken of leakage currents which can induce false EDM signals. But the main issue remains in the monitoring of magnetic fields in the whole system which can create systematic effects during measurements.

Systematic effects

Systematic effects have been dramatically reduced by the use of a ^{199}Hg comagnetometer [43,54] to correct the changes in magnetic field. Fig.6.3 shows the cell where mercury atoms are polarized by optical pumping. They enter the same volume as the UCN and feel the Ramsey sequence. The average magnetic field in the storage chamber is measured during the free precession period by the use of an UV light. Its measured intensity is directly related to the mercury precession frequency.

Other effects may create additional systematic uncertainties by slightly modifiying the vertical magnetic field seen by the UCN and hence impacting on the precession frequency. Here are some of the main effects:

- $\vec{v} \times \vec{E}$ effect: A particle with velocity $\vec{v}$ moving in $\vec{E}$ and $\vec{B}_0$ fields will see in its rest frame a modified magnetic field $\vec{B}'$ which is, to first order in v/c:

$$\begin{aligned} \vec{B}' &= \vec{B}_0 + \overrightarrow{\Delta B}, \\ &= \vec{B}_0 - \frac{\vec{v} \times \vec{E}}{c^2}. \end{aligned} \tag{6.2.11}$$

Assuming that the electric field is not perfectly parallel to $\vec{B}_0$, which is considered along z, one can write:

$$\begin{aligned} B'^2 &= {B'_z}^2 + {B'_{xy}}^2, \\ &= (B_0 + \Delta B \sin\theta)^2 + (\Delta B \cos\theta)^2, \end{aligned} \tag{6.2.12}$$

where θ is the angle between $\vec{E}$ and $\vec{B}_0$ in the plane perpendicular to $\vec{v}$. Expanding this equation and noting that $\Delta B \ll B_0$ and $\theta \ll 1$, one finds the following expression for the field length in the rest frame of the UCN:

$$B' \approx B_0 + \Delta B\,\theta + \frac{\Delta B^2}{2B_0}, \tag{6.2.13}$$

which leads to the following precession frequency shift:

$$\Delta\omega \approx -\gamma_n \left(\Delta B\,\theta + \frac{\Delta B^2}{2B_0} \right), \tag{6.2.14}$$

where the first term on the right-hand side is proportional to ΔB and so to E. As a consequence, it follows the electric field during its reversal and can be interpreted as an EDM signal (1). When an ensemble of UCN is considered, the effect of this term comes from either average centre-of-mass motion — i.e. neutrons can warm due to the vibrating walls or by nanoparticles scattering (cf. chapter 7) — or from rotation of the UCN inside the storage chamber. The corresponding uncertainty on the EDM is very small for trapped UCN and has been estimated in the RAL-Sussex-ILL experiment to about $10^{-27} e \cdot \mathrm{cm}$ [10]. There is also the last term which does not give any false EDM signal since it is proportional to E^2. However, one notes that a change in the magnitude of the electric field during its reversal would produce a correlated shift in frequency which would also add some uncertainty in the EDM measurement. This was negligible in the RAL-Sussex-Experiment.

- Geometric phase effect: This is the result of the combination of the $\vec{v} \times \vec{E}$ effect with a vertical magnetic field gradient $\partial B_0/\partial z$ which produces a rotating magnetic field which then shifts the larmor precession frequency of the trapped UCN [55].
- Leakage currents: Currents that flow from an electrode to the other along the cylindrical shape of the quartz bottle (i.e. these are helical currents) will create a vertical magnetic field which is correlated with the electric field direction. So it will not be distinguishable from an EDM.

---

(1) One should note that this term does not violate T symmetry since $\vec{v}$ changes sign under T reversal and so does $\overrightarrow{\Delta B}$. This causes the Hamiltonian $-\vec{\mu}_n \cdot \overrightarrow{\Delta B}$ to be conserved under T.

- Oscillating fields: Some ripples on the high-voltage may induce alternating currents which can then create a rotating magnetic field that modifies the Larmor precession frequency of the neutrons in the storage chamber.

Finally, The overall uncertainty due to systematics effects has been carefully estimated to $0.7 \cdot 10^{-26} e \cdot \mathrm{cm}$ by the RAL-Sussex-ILL collaboration [10].

6.3 Future experiments

Here is a brief introduction on the ongoing research in the world concerning the neutron electric dipole moment. Indeed intensive efforts are produced by several teams in order to improve the statistical sensitivity and to control more efficiently the systematics. All the experiments presented below use the Ramsey method to determine the neutron EDM.

6.3.1 Cryogenic experiments

CryoEDM @ ILL

This experiment is being performed at the Institut Laue-Langevin by the RAL-Sussex-Oxford-Kure-ILL group. Here UCN are produced in superfluid liquid Helium (LHe) at 0.5 K by single-phonon downscattering of a 8.9 Å cold neutron beam [56]. This production process enables to get higher densities ($\sim 250\,\mathrm{cm}^{-3}$) than in their previous room temperature experiment ($\sim 10\,\mathrm{cm}^{-3}$). Since LHe has higher resistivity than vacuum, it enables them to reach stronger electric fields (~ 40 kV/cm). SQUID magnetometry will monitor the magnetic field inside a double storage chamber setup, in which electric fields are in opposite directions inside both cells. Such a double system will prevent some annoying systematics. For example, these are effects like uncorrected magnetic field drifts which could occur with a single cell during the electric field reversal. New detectors have also been developed to work in the LHe environment [57]. They are silicon solid state detectors (see chap. 8) coated with a thin layer of ^{6}LiF.

This collaboration planned to improve by two orders of magnitude the present experimental limit.

nEDM experiment @ SNS

UCN production is the same that for CryoEDM. The major difference remains in the use of polarized ^{3}He atoms as comagnetometer and spin analyzer.

Indeed it appears that the neutron absorption cross section σ_a in the reaction n(^{3}He,p)t is spin-dependent. If the spins of the neutron and ^{3}He are parallel, there is no reaction ($\sigma_a^{th} \sim 0$ b) whereas if they are antiparallel, the reaction rate is twice that of the unpolarized reaction ($\sigma_a^{th} \sim 10.6$ kb) [58, 59]. Moreover the resulting fission products (t,p) create scintillation light in LHe that can be detected. This means that in the step 3 of the Ramsey measurement — neutron and ^{3}He oscillate respectively at their own Larmor frequency in the plane perpendicular to the static magnetic field — one would detect a signal beating at a frequency which is the difference of the two angular frequencies of the neutrons and ^{3}He atoms.

The neutron EDM would be measured by a change in this frequency after reversal of the electric field direction relative to the static magnetic field. And this will be corrected by the SQUID signal measuring the ^{3}He magnetization.

The goal of this experiment is to gain two orders of magnitude on the present limit [60].

6.3.2 Room temperature experiments

Both previous experiments imply new R&D developments since they work at very low temperatures and use new UCN production method. Here two future experiments working at room temperature are presented. They involve important improvements on magnetic field control and cancellation of systematics.

nEDM experiment @ ILL

This experiment is lead by the PNPI group [61]. UCN are produced by the ILL-PF2 source (see section 7.2.1). They are polarized by a superconducting polarizer [62] and are filled in 4 sets of double storage chambers. The magnetic field will be stabilized by 16 cesium magnetometers [63]. New solid state detectors which include spin analysis have been built [64]. The goal of this project is to reach a precision on the neutron EDM of about $10^{-27} e \cdot \mathrm{cm}$.

nEDM experiment @ PSI

This project is presently using the RAL-Sussex-ILL apparatus which is now located at PSI. It will exploit the future high density spallation UCN source which is under construction to reach a nEDM of $\sim 10^{-27} e \cdot \mathrm{cm}$ (more details of the source are presented in section 7.2.2). In parallel, this project also planned to build a new spectrometer by taking advantage of the initial tests and developments performed on the present set-up. The goal will be to improve an order of magnitude further the experimental limit on d_n. More details are given in [33].

This thesis has been carried out within this experiment. The UCN density inside the EDM spectrometer is expected to be improved by two orders of magnitude due to the new UCN source [32]. This will require fast UCN detectors. Moreover, the simultaneous spin analysis has been proposed instead of the sequential method. The goal is to decrease the depolarizations within the system with a faster spin analysis. These points have been studied in this thesis.

Chapter 7

Ultracold neutrons

This chapter describes briefly some fundamental properties of ultracold neutrons. It is also a reference for the physics implemented in the codes developed during this thesis to simulate the interaction of ultracold neutrons with matter and fields (i.e. absorption, reflections, spin tracking...). Further details on the UCN physics can be found in [53, 65].

7.1 Introduction

Ultracold neutrons are usually defined by their ability to be totally reflected at any angle of incidence from a wide variety of materials. This is due to their extremely low kinetic energies which are typically below 335 neV. It corresponds to velocities lower than 8 m/s, temperatures below 4 mK and wavelengths higher than 500 Å. Consequently, it becomes possible to store UCN in chambers for long periods and to study neutron properties.

7.2 UCN production

Two UCN sources are briefly discussed. All the tests reported in this document were performed at the ILL/PF2 instrument. Details about the flux intensity and the velocity distributions available at ILL are given. Then the PSI project of an intense source is presented since it is planned to provide UCN to the future neutron EDM experiment at PSI (see section 6.3) which motivated this thesis.

7.2.1 The ILL UCN source

Fast neutrons (energy ~2 MeV) are initially produced in a reactor core through the fission process of uranium 235. They are then downscattered in the surrounding moderator (heavy water) in order to give slower (mainly thermal) neutrons. The flux intensity of thermal neutrons has been estimated to be about 1.5×10^{15} $\mathrm{cm}^{-2}\cdot\mathrm{s}^{-1}$ [66]. To cool further down the energy spectrum of the thermal neutrons, an additional moderator, a liquid deuterium cold source (lD_2) at $T = 20$ K, is placed close to the fuel element. Fig. 7.1 illustrates the slowing down of the thermal spectrum which produces an increase of slow neutrons.

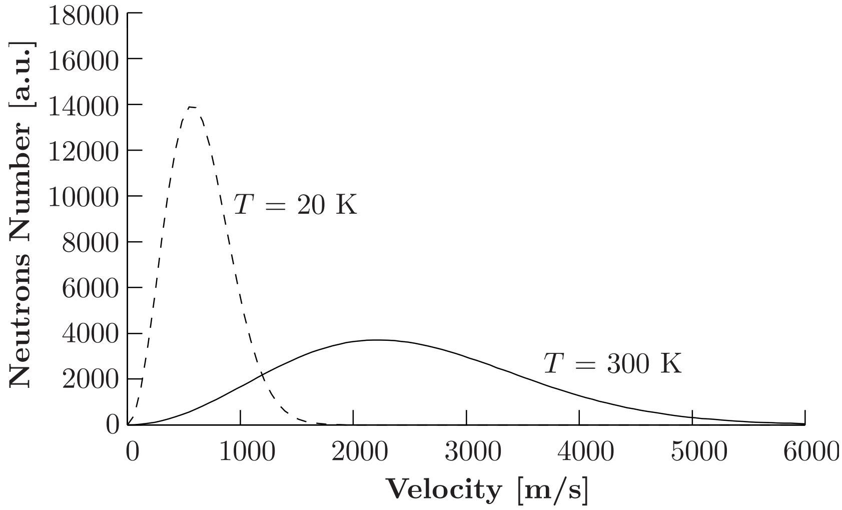

Figure 7.1: Slowing down of the thermal neutron spectrum ($T = 300$ K) by the liquid D_2 cold source ($T = 20$ K). A Maxwellian velocity distribution of temperature T is usually a good approximation (i.e. neutrons are considered in equilibrium with the moderator) [53]. Moreover, note that only a fraction of the thermal neutrons are cooled down. The result is an increase of the slow neutrons number in the lD_2 source.

Figure 7.2 shows how neutrons are vertically extracted from the lD_2 source. At the entrance of the so-called Steyerl's turbine, only very cold neutrons (VCN), with velocity of about 50 m/s, remain [28, 29]. The phase space shift to the UCN region is produced by multiple reflections of the incoming VCN on the nickel blades of the turbine which turns at the velocity of 25 m/s. UCN are then available on four different ports. The last one is dedicated to VCN experiments.

The typical UCN densities has been measured as ~100 UCN per cm^3 inside the turbine [29] and to a few tens of UCN per cm^3 for typical storage experiments [24,29]. For instance, if one considers a storage spectrum with a mean velocity of 3 m/s, then the equivalent UCN flux can be evaluated to $\sim 3 \cdot 10^3\,\mathrm{cm}^{-2} \cdot \mathrm{s}^{-1}$.

Figure 7.3, extracted from [29], shows an example of velocity spectra obtained at the exit ports of the turbine. The coordinate frame used for the measurement (see Fig. 7.2) is ($\mathcal{O}$, ξ, η, α) where ξ is the axis along the direction of blade motion, η is perpendicular to ξ and α is the angle about η. $\alpha = 0$ gives the direction perpendicular to ξ and η. Time-of-flight (TOF) measurements were carried out along the axis given by α. Since even the best guide tubes can only contain UCN with velocities $\lesssim 8$ m/s (see Table 7.1 in section 7.3), one can conclude from these spectra that the real limitations (specially on the lateral distribution) will be imposed by the guide tubes which are used to extract UCN towards experiments. Indeed we generally use stainless steel guide tubes between the source and experiments which limit the lateral velocity distribution (perpendicular to the tube axis) below 6 m/s (see Table 7.1). In contrast, the axial component remains what we see on Fig. 7.3 with a velocity

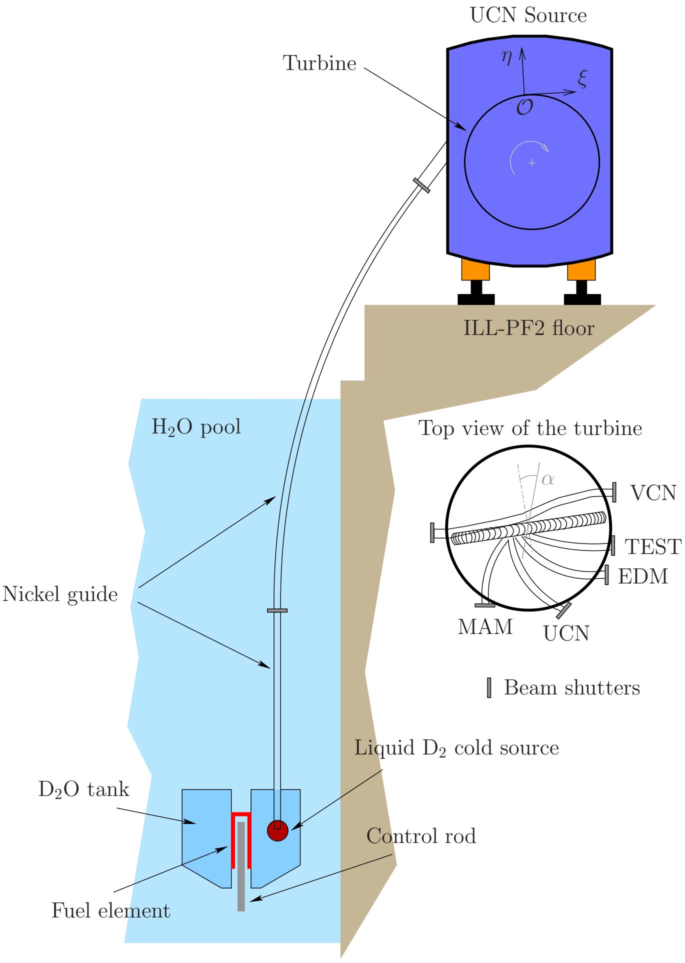

Figure 7.2: UCN production at ILL. VCN ($v \sim 50$ m/s) are selected from the liquid D_2 source through a long curve guide. These neutrons are then decelerated by collisions on the turbine blades. UCN are finally available at 4 exit ports – called TEST, EDM, UCN and MAM. A bypass of the feeding beam enables to use VCN in a dedicated area at PF2.

range which depends on the UCN ports.

7.2.2 The PSI UCN source

The principle of the UCN production (see Fig. 7.4) is based on the spallation process of a pulsed proton beam with a high intensity (2 mA, 600 MeV). The beam interaction with a heavy target (mainly lead) produces fast neutrons ($\sim$ 2 MeV) which are cooled down in heavy water ($T \sim 300$ K) and then in a solid deuterium cold source ($T \sim 5$ K). The proton beam is applied during a few seconds and UCN fill a storage vessel with a volume of about 2 m^3. When the density of UCN reaches a saturated value in the vessel, the shutter of the source is closed. UCN are then available during about 800 s till the next proton pulse.

Simulations gave an expected density of a few 1000 UCN per cm^3 inside the

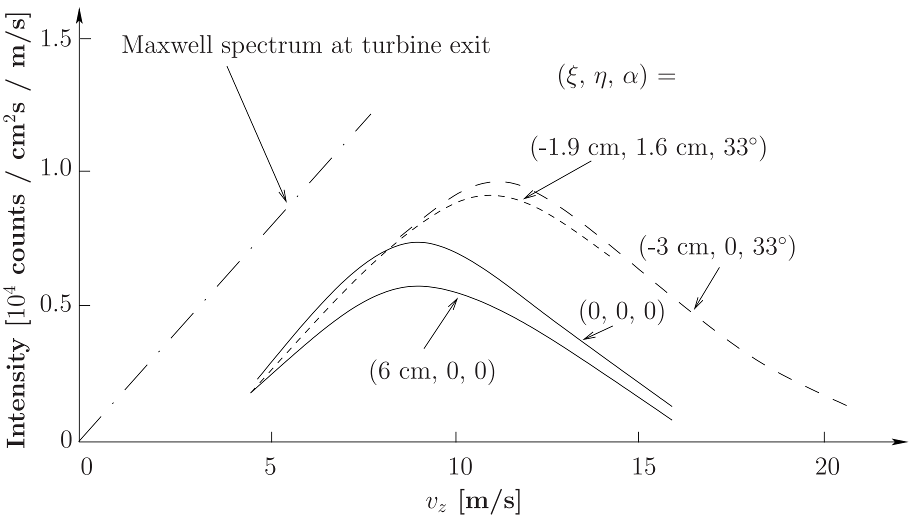

Figure 7.3: Velocity spectra from time-of-flight (TOF) data. The frame ($\mathcal{O}$, ξ, η, α) is shown on Fig. 7.2. v_z is the velocity component along the guide tube used in [29]. Indeed TOF measurements only give the longitudinal component $v_z = \Delta z/\Delta t$ where Δz is the distance-of-flight and Δt is the TOF.

storage volume [32]. Assuming a UCN density of about 1000 cm^{-3} and a mean velocity of 3 m/s, the delivered UCN flux is about $3 \cdot 10^5 \text{cm}^{-2} \cdot \text{s}^{-1}$.

The UCN source should be launched for early 2010. Further information are available at [67].

7.3 UCN interactions

7.3.1 The gravitational interaction

Despite its weakness, the effect of the gravitational interaction on ultracold neutrons is not negligeable. In the earth's gravitational field of strength g, the potential energy of a UCN at height h is given by:

$$V_g = m_n g h, \tag{7.3.1}$$

where m_n is the neutron mass. This corresponds to a differential potential energy of about 102 neV/m. Therefore, a UCN with a kinetic energy of 200 neV is unable to go beyond 2 m height from its initial position. Inversely, UCN can be accelerated by falling in the gravitational field.

7.3.2 The strong interaction

The strong interaction between a neutron and a nucleus can be described by a strong attractive potential with a depth of about 40 MeV and a short range R of a few 10^{-15} m.

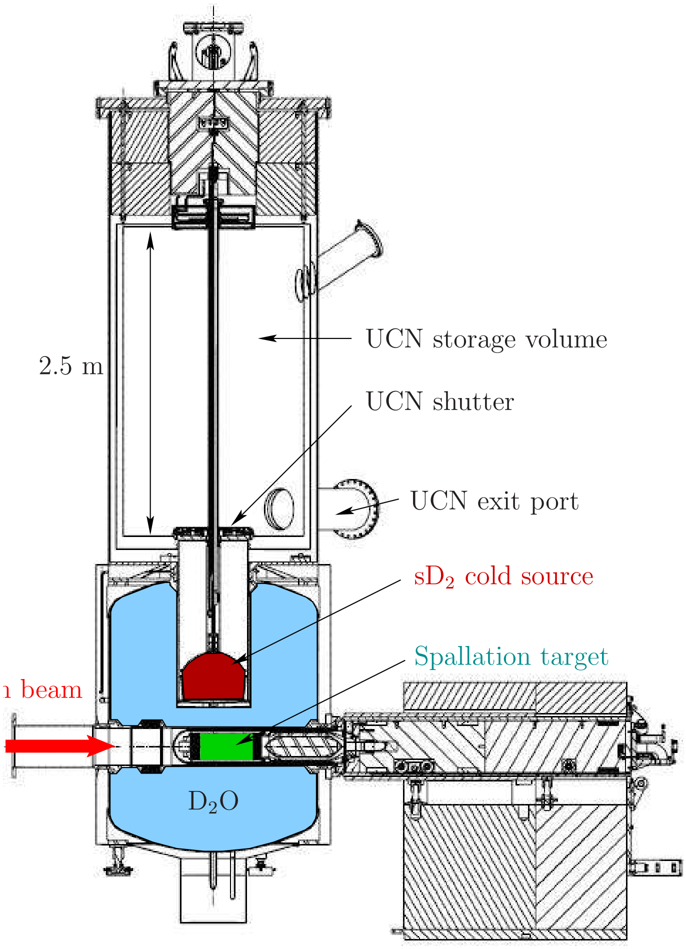

Figure 7.4: Future UCN production at PSI. A proton beam with a high power (600 MeV, 2 mA) interacts with a heavy spallation target made of lead (mainly). Resulting neutrons are thermalized in the moderator (D_2O) and furthermore inside the solid deuterium cold source at ~6 K to the UCN range. The proton beam is switched on during a few seconds, but this is sufficient to fill the two cubic meter storage vessel.

In the scattering process of a slow neutron, the total wave function of the scattered neutron, far from the nucleus, may be written as the sum of an incident plane wave and an outgoing spherical wave. Assuming that the incident particle goes along the z axis, then one has:

$$\begin{aligned}\psi(r \gg R) &= \psi_{incident} + \psi_{scattered}, \\ &\approx e^{ikz} + f(\theta)\frac{e^{ikr}}{r}. \end{aligned} \tag{7.3.2}$$

The quantity $f(\theta)$ is the scattering amplitude and contains all the information of the interaction between the neutron and the strong potential. Since the slow neutrons energies (< 1 eV) are far below the strong potential depth (~ 40 MeV), the perturbation theory is not suitable to describe the scattering of such neutrons by a

Element	V_F [neV]	v_c [m/s]
H_20	-14.7	-
Polyethylene	-8.7	-
Al	54	3.2
Si	54	3.2
Quartz (SiO_2)	90	4.1
DPS	162	5.6
Cu	168	5.7
Stainless Steel (316)	185	5.9
Fe	210	6.3
Be	252	6.9
^{58}Ni	335	8.0

Table 7.1: Fermi potentials and critical velocities of common materials.

nucleus. Fermi solved this problem by introducing a pseudo-potential of the form:

$$U_F(\vec{r}) = \frac{2\pi\hbar^2}{m_n} b\delta^{(3)}(\vec{r}), \tag{7.3.3}$$

where b is the bound nucleus scattering length and m_n the neutron mass. One notes that for a usual case of $b > 0$, the Fermi pseudo potential is repulsive whereas the strong interaction is actually attractive.

The mean Fermi potential

For a material, the expression (7.3.3) has to be averaged since the UCN will interact with an ensemble of nuclei. The resulting mean Fermi potential, or simply Fermi potential, can be written as:

$$V_F = \frac{2\pi\hbar^2}{m_n} Nb, \tag{7.3.4}$$

where N and b are respectively the number density and the bound scattering length of the material. We often use the velocity correspondance of V_F that is the critical velocity $v_c = \sqrt{2V_F/m_n}$. Table 7.1 gives some values of V_F and v_c for commonly used materials.

The UCN interaction with a material can thus be described by a quantum mechanical problem with a potential step of height V_F which characterizes that material. A neutron impacting on some substance will have basically two possibilities depending on its normal velocity $v_\perp$ to the surface compared with the critical velocity v_c. Either it is reflected for $v_\perp < v_c$ or transmitted for $v_\perp > v_c$. But as we are dealing with quantum mechanics, a small probability of transmission (resp. reflection) remains for the case $v_\perp < v_c$ (resp. $v_\perp > v_c$) [53].

Transmitted UCN

The most important interactions that a UCN undergoes when it is transmitted through a material are:

i) The *absorption* by a nucleus. This process is characterized by the absorption cross section σ_a which is found to be, for slow neutrons ($E \leq 1$ eV), inversely proportional to the neutron velocity v inside the medium. This holds when the neutron wavelength is much greater than the region where the interaction responsible for the absorption acts [68].

ii) The *inelastic upscattering.* This process occurs when a UCN scatters inelastically with a thermally vibrating nucleus. In this case the neutron gains so much energy that it is no longer in the UCN energy range. It is then lost from the system at the next collision. As for the absorption, the upscattering process can be characterized by the cross section σ_{inel}, also proportional to $1/v$ for low neutron energies [69].

Given that these two processes have the same dependence — for an experimental justification of the $1/v$ law for UCN see for example [70] —, one can define a general cross section $\sigma_{tot} = \sigma_a + \sigma_{inel}$ which characterizes the interactions of an incident UCN flux ϕ in some medium. After a distance $\mathrm{d}x$, the outgoing flux will be attenuated as:

$$\mathrm{d}\phi = -\phi\sigma_{tot}N\mathrm{d}x, \tag{7.3.5}$$

with N the number density of the medium. Thus the transmitted flux for a thickness x is, after integration:

$$\phi(x) = \phi_0 e^{-x/\ell}, \tag{7.3.6}$$

where $\ell = N\sigma_{tot}$ is the interaction length inside the material and ϕ_0 is the flux at the entrance of the material.

Reflected UCN

The resolution of the Schrödinger equation for a one-dimensional potential step of height V_F shows that the wavefunction penetrates a little bit in the step for UCN with $v_\perp < v_c$. Thus one has to take into account the fact that the absorption and upscattering may occur during this penetration. Indeed, this is done by adding artificially W as an imaginary part of the potential such that the new step height is given by $U = V_F - \mathrm{i}W$. This loss probability can be expressed by the non-conservation of the current density $\vec{j}$ such that:

$$\frac{\partial\rho(\vec{r},t)}{\partial t} + \mathrm{div}\vec{j}(\vec{r},t) = \frac{-2W}{\hbar}\rho(\vec{r},t) \tag{7.3.7}$$

In other words, the probability density $\rho(\vec{r},t)$ at some point $\vec{r}$ decays exponentially with time t at a rate $1/\tau_{loss} = 2W/\hbar$ [53]:

$$\rho(\vec{r},t) = \rho(\vec{r},0)e^{-t/\tau_{loss}}. \tag{7.3.8}$$

In fact, equations (7.3.6) and (7.3.8) express the same attenuation in different ways. By comparing, it follows that a correct description of the losses is given by setting:

$$W = \frac{\hbar}{2}vN\sigma_{tot}. \tag{7.3.9}$$

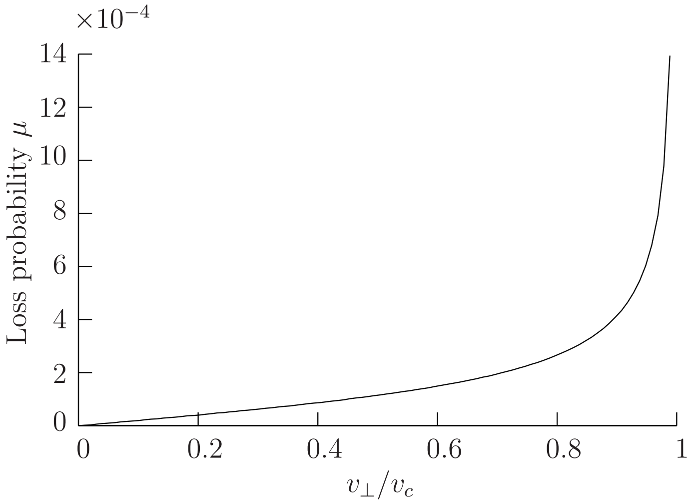

Figure 7.5: Loss probability μ as a function of $v_\perp/v_c$ for a common loss factor of $\eta = 10^{-4}$.

Since $\sigma_{tot} \propto 1/v$, one notes that W becomes independent of the neutron velocity v in the medium. The fact that losses can happen during reflection makes the probability of reflection $|R|^2$ slightly smaller than 1.

For a one-dimensional potential step, the amplitude of the reflected wave is given by:

$$R = \frac{\sqrt{E_\perp} - \sqrt{E_\perp - U}}{\sqrt{E_\perp} + \sqrt{E_\perp - U}}, \tag{7.3.10}$$

where $E_\perp$ is the energy of the incident neutron perpendicularly to the medium. Given that $W \ll V_F$ for most materials (this is not true for strong absorbers), one can expand the equation (7.3.10) such that the probability of reflection can be approximated by:

$$|R|^2 \approx 1 - 2\eta\sqrt{\frac{E_\perp}{V - E_\perp}} = 1 - \mu(E_\perp), \tag{7.3.11}$$

where $\eta = W/V_F$ is the loss factor and $\mu(E_\perp)$ is the wall probability per bounce. Figure 7.5 shows graphically the behaviour of μ as a function of $v_\perp/v_c$. Indeed, from (7.3.11) we find:

$$\mu(\xi) = 2\eta\sqrt{\frac{\xi^2}{1-\xi^2}}, \quad \text{with} \quad \xi = \frac{v_\perp}{v_c}. \tag{7.3.12}$$

One can see that the probability of loss remains very weak for $v_\perp < v_c$ and increases tremendously after this limit to reach almost 100% losses for $v_\perp > v_c$. That explains the expression *critical* for the velocity v_c.

The precise understanding of UCN losses is specially important in storage experiments using material traps (e. g. in the search for the EDM or the lifetime of the neutron). Indeed, for UCN which have velocities below the critical velocity of the material of the chamber, the only possibility of losses should occur, as it was mentioned previously, during the first 100 Å inside the potential step. Since the strong absorbers (e.g. ^{3}He, Cd, Gd [71]) are difficult to encounter in nature, the main effect would be inelastic upscattering (heating) due to impurities on the surface of the cell. This was shown in 1978 [72] where thermal neutrons have been registered escaping from the trap. It turned out from this study that hydrogen impurities (H has a large inelastic cross section ~80 b) were the more probable cause of this inelastic phenomenon. But the problem was that the quantity of hydrogen needed to explain the observed losses would have been too high. Since then, other effects have been shown in order to explain the "anomalous" losses inside storage traps. In [73, 74], a slight increase (~100 neV) of the UCN energy has been demonstrated. The scattering upon nanoparticles weakly attached to the wall surface [75, 76] have been developed to explain this small heating. Nevertheless, it was recently shown [77] that this phenomenon can not explain the UCN anomalous losses due to the low probability of such a weak energy transfer compared with the level of UCN losses.

Thus the UCN anomalous losses are still unexplained. This little summary shows that despite the fact that UCN storage can be well understood at first sight, since it is a quantum mechanical problem with one potential step, experiments induce a lot of questions and difficulties which have not been totally solved yet.

7.3.3 The magnetic interaction

The potential energy V_m of a neutron in a magnetic field $\vec{B}(\vec{r},t)$ is:

$$V_m = -\vec{\mu}_n \cdot \vec{B}(\vec{r},t), \tag{7.3.13}$$

where $\vec{\mu}_n$ is the magnetic dipole moment of the neutron. The amplitude of this interaction is about 60.3 neV/T. This makes very useful the use of ferromagnetic foils to polarize (or analyze) the spin of UCN (see chapter 11). Indeed, an incoming UCN on a magnetized medium will see the following potential:

$$\begin{aligned} V &= V_F + V_m, \\ &= \frac{2\pi\hbar^2}{m_n} Nb \mp \mu_n B(\vec{r},t), \end{aligned} \tag{7.3.14}$$

where we use the expression (7.3.4) of the Fermi potential. the $\mp$ correspond to the two orientations of the neutron magnetic dipole moment relative to the magnetic field. This means that the probability of reflection of the UCN on a magnetized material is spin-dependent.

Since we have mentioned above the storage of UCN in bottles, it should be emphasized here the possibility of magnetic storage of ultracold neutrons which have the advantage not to suffer from contact losses like for material traps. Basically, if one creates a region of space where the magnetic interaction $V_m < 0$, then the confinement of UCN becomes possible. For more details on that subject, see [53,65] and references therein.

Chapter 8

Overview of UCN detectors

This chapter is devoted to the current status about detector development in UCN physics. The basic requirements of these detectors will be precised in connection with the measurement of the neutron EDM.

8.1 Introduction

A UCN detector is based on the same methods used for slow neutron detection. In principle, the detection can be described in two steps. First neutrons are converted to charged particles; for this step, nuclei with a high neutron absorption cross section (e.g. ^{3}He, ^{6}Li, ^{10}B, ^{235}U, etc) are used. Then, the created charges are collected to give a signal indicating the neutron detection. One of the main difference between UCN detection and detection of higher energy neutrons is the existence of the critical velocity v_c for UCN. This implies to use materials with a low Fermi potential. Another difference is the thickness of the detector. Since the absorption cross section becomes extremely large for UCN, a small amount of detection material is sufficient. Moreover, this enables not to detect higher energy neutrons which may create background signals in UCN detection.

Up to now, the most common UCN detector is the ^{3}He gas counter which combines high detection efficiency and low sensitivity to background [65]. Its main limitation comes from its pulse duration (about 2 μs without special readout systems) which prevents its use at high rates with the electronic readout used so far. Indeed, an intensive detector development has been made concerning other kind of detectors in connection with the advent of new intense UCN sources. Studies on silicon solid state detectors [34, 57, 64, 78, 79], ^{6}Li-glass scintillators [39] and Gas electron multiplier (GEM) detectors (i.e. namely Cascade-U detector) [37] have been recently carried out. All these detectors are able to face with higher rates than the standard ^{3}He gas detector. Note that, apart from the silicon detectors, all kind of detectors discussed below have been used during our experimental tests.

8.2 Detector requirements

It is interesting to evaluate the needs when developping new UCN detectors. Table 8.1 shows the list of the important requirements with some rough values.

	Requirement on	Order-of-magnitude	Comments
a.	Efficiency ϵ	$\epsilon > 50\%$	for velocities < 10 m/s
b.	Maximum UCN rates	$10^6 - 10^7$ c/s	detector with ⌀ 80 mm
c.	Intrinsic background	$\sim 10^{-3}$ c/s	
d.	Radiation hardness	$> 10^{12}\,\mathrm{cm}^{-2}\,\mathrm{y}^{-1}$	
e.	Critical velocity v_c	$v_c < 4$ m/s	

Table 8.1: Basic requirements for the development of UCN detectors.

a. The detector efficiency has to be as high as possible for UCN velocities below 10 m/s. The main limiting factors are: i) the critical velocity of the detector ; ii) the presence of a dead layer prior to the UCN detection region (UCN loss) ; iii) the presence of a dead layer after the UCN detection region (loss of charged particles resulting from the neutron detection). This point has been studied in details for the cascade-U detector in section 9.3).

b. High count rate capabilities becomes a necessity with the arrival of new intense UCN sources. The values given in table 8.1 come from the expected UCN density at the future PSI source (cf. section 7.2.2). Considering a density about a few 1000 UCN per cm^3 inside the storage chamber of the nEDM spectrometer and a mean UCN velocity of 3 m/s, the maximum count rate for a detector of 80 mm diameter is about 10^7 c/s.

c. A low sensitivity to background is required for detectors that will be used close to UCN sources. Gamma but also thermal neutrons background should be considered. ILL measurements at PF2 lead to a few 10^{-3} c/s for ^{3}He gas detector and cascade-U detector.

d. In the case of experiments with long measuring times, one has to take into account the damage created within the detector due to the neutron detection. For instance, the neutron EDM experiment will be performed during several months.

e. The critical velocity v_c of the detector impacts directly on its efficiency at low velocities. Lowering the detector enables to avoid the effect of the critical velocity by accelerating the UCN. Moreover, some experiments with silicon solid state detectors using ^{6}Li/Ti multilayers have shown the possibility of detecting UCN with an efficiency about 30-40% in the velocity range 2-2.6 m/s [34].

For the nEDM experiment, the UCN detection will be coupled to UCN spin analysis. It is therefore important that the detectors get a low sensitivity to magnetic fields. Finally, any detector should be as robust as possible, easy to handle and not expensive. In the following, we give more details on the principle of detection and the characteristics of UCN detectors we have used during our tests at ILL.

8.3 Gas detectors

8.3.1 The ^{3}He detector

The ^{3}He detector is the basic detector in UCN physics. However, unless the readout electronics be segmented, it is no longer suitable with the new generation of intense UCN sources.

Working principle

A sketch of the ^{3}He gas detector is given in Fig. 8.1. UCN enter into the detector through a 100 μm thick Al entrance window. Then they travel inside a gas volume which is, at the same time, the converter and the charge collecting region. The neutron absorption is performed by ^{3}He nuclei which have a high thermal absorption cross section σ_a^{th} of 5330 barn. The capture reaction is the following:

$$\mathrm{n} +^3\mathrm{He} \longrightarrow \mathrm{p} + \mathrm{t} + 764\,\mathrm{keV}.$$

The resulting charged particles ionize an admixture of Ar/CH_4 or Ar/CO_2. Standard values for the partial pressures are $p(^3He) = 15$ mbar, $p(CH_4/CO_2) = 15$ mbar and $p(Ar) = 1.1$ atm. The electrons produced by the protons and tritons are collected on a 50 μm tungsten anode. The detector has an internal preamplifier and a discriminator. Two output signals are available: an analog and a logical output (TTL). The threshold of the logical output can be controlled manually. The duration of the analog pulse is typically 1-2 μs.

Typical performances

With the single channel readout system, the ^{3}He gas detector will not be able to cope with the count rates available at the future UCN sources. However some of their characteristics can be taken as reference for the development of new detectors with high rate capabilities. Their neutron/gamma discrimination is easy and very successful. Since they use low Z material at low density (gas state), their sensitivity to gamma background is very low. Their critical velocity is one of the lowest available (v_c(Al) = 3.2 m/s).

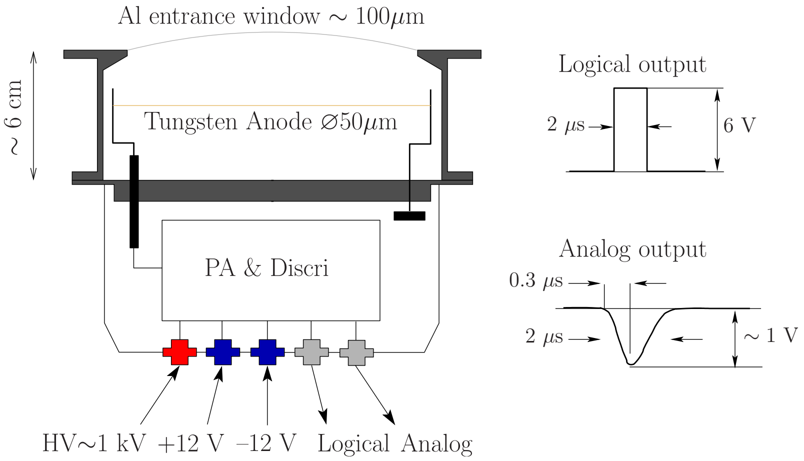

Figure 8.1: Sketch of a "Strelkov-Dunia-10" ^{3}He gas detector.

8.3.2 The Cascade-U detector

Working principle

The Cascade-U is based on the GEM technology [36]. Its sketch is shown on Fig. 8.2. The converter is a thin ^{10}B layer coated by electron beam evaporation onto a 100 μm aluminium entrance window. UCN are highly absorbed by the boron nuclei ($\sigma_a^{th} =$ 3840 barn). Two capture reactions may occur with the respective branching ratios of 6.4% and 93.6%:

$$\begin{array}{lcll} \mathrm{n} + {}^{10}\mathrm{B} & \longrightarrow & \alpha\ (1.78\ \mathrm{MeV}) + {}^{7}\mathrm{Li}\ (1.01\ \mathrm{MeV}) & [6.4\%] \\ \mathrm{n} + {}^{10}\mathrm{B} & \longrightarrow & \alpha\ (1.47\ \mathrm{MeV}) + {}^{7}\mathrm{Li}\ (0.84\ \mathrm{MeV}) + \gamma\ (0.48\ \mathrm{MeV}) & [93.6\%] \end{array}$$

The α or the ^{7}Li particles enter in the gas volume which is continuously filled with Ar/CF$_4$ (70/30) at 1 bar. Primary e^{-}-ion pairs are produced along their track. One centimeter away, the electrons are multiplied close to the holes of a GEM foil. Then they are guided through and finally drift to the readout structure. It has a surface of about $10 \times 10\,\mathrm{cm}^2$ and has a total of 8×8 pixels. This enables to use 2D-imaging. The integrated signal over all pixels can also be used for neutron counting. For more details see [37].

Typical performances

Thanks to its readout electronics, the count rate capabilities of this detector can be as high as 10^7 c/s/cm^2. The detection efficiency has been estimated by simulations and is about 80% for UCN with velocities close to 4 m/s [44]. It shares with the ^{3}He gas detector a very low sensitivity to background (gamma + thermal neutrons) as well as magnetic fields.

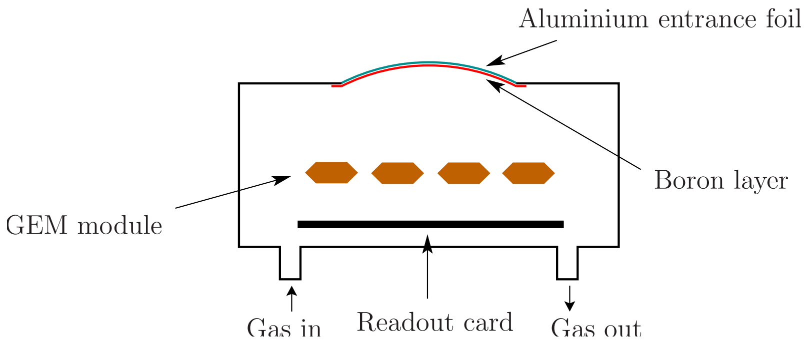

Figure 8.2: Sketch of the Cascade-U detector.

8.4 Silicon solid state detectors

These detectors have recently been put forward in UCN physics [57, 64]. They all use ^{6}Li nuclei (σ_a^{th} = 940 barn) as UCN converter. A layer of ^{6}LiF is used. The neutron capture follows the reaction:

$$\mathrm{n} +^6\mathrm{Li} \longrightarrow \alpha\,(2.05\,\mathrm{MeV}) + \mathrm{t}\,(2.73\,\mathrm{MeV}).$$

The resulting charge products are detected with a silicon semiconductor. A relative efficiency of about 80% to the ^{3}He gas counter has been measured at ILL-PF2 with such detector [57]. Moreover it has been shown recently that defects of the charge collection and energy resolution occur under a neutron dose of $8 \cdot 10^9$ neutrons [57]. This can be a problem for long term experiment like nEDM.

Recent developments

Silicon detectors with a ^{6}LiF converter were successfully tested by two groups involved in nEDM searches, namely the CryoEDM collaboration [57] and the PNPI group [64]. Both collaborations combine UCN spin analysis with UCN detection. The main difference is that the silicon detectors in CryoEDM are used at liquid helium temperatures whereas the PNPI colleagues work at room temperature.

Recently, a solid state detector with ^{6}Li/Ti multilayer converter has been developped to be used at liquid helium temperatures [34, 80, 81]. The use of a multilayer converter with titanium (V_F = -48 neV) has enabled to decrease the critical velocity of the detector with a non-zero detection efficiency of about 30% at 2 m/s (from cold neutron reflectivity measurements [34]).

A group from Technical University of Munich has also studied UCN multilayer converters based on ^{6}LiF/^{62}Ni and ^{6}LiF/Ti [78, 82–84]. By emphasizing the problem of oxygen impurities which oxidizes ^{6}Li and Ti and may form compounds with high critical velocity, they developed an ultra-high evaporation plant for multilayer deposition to avoid this issue.

8.5 Scintillator detectors

The scintillator detectors are ^{6}Li-doped scintillators. Those used in this thesis are from Applied Scintillation Technologies (AST). They belong to the GS families [38]. They were first tested with UCN in 2003 at ILL by our group [39].

8.5.1 GSx glass scintillators properties

The UCN detection is performed thanks to the ^{6}Li converter. Within the glass, the resulting α and triton activate the Cerium Ce^{3+} sites and blue light is emitted with a maximum wavelength at 395 nm. This enables the use of several types of photomultiplier tubes without wavelength shifters. The obvious reason for developing such a detector is the high count rates that can be registered due to a very short decay time about 50-70 ns [38].

Table 8.2 shows the characteristics of three scintillators, namely the GS3, GS10 and GS20.

	GS3	GS10	GS20
^{6}Li enrichment [%]	0.01	7.5	95
^{6}Li density [10^{21} at.cm^{-3}]	$6.4 \cdot 10^{-4}$	1.6	20.0
Density [g/cm^{3}]	2.66	2.50	2.50
Refractive index	1.58	1.55	1.57
Relative light output	100	85	85
Fermi potential [neV]	101	85	103
Critical velocity [m/s]	4.4	4.0	4.4

Table 8.2: Main properties of three scintillators. The Fermi potentials (critical velocities) are calculated from the atomic composition of each scintillator [38] and the neutron scattering lengths [40].

Whereas the GS10 has a natural content in ^{6}Li, the GS3 is depleted and the GS20 is doped in ^{6}Li. Their density are close to 2.5 g/cm^{3} and the refractive index are about 1.6. It has to be noted that the ^{6}Li contents given in table 8.2 are the initial values before the melting of the glasses. The finished product may have a lower and varying ^{6}Li content [38].

Practically, the scintillators are coupled to Photonis XP53X2/B photomultiplier tubes used with the VD202K/03 voltage divider (A type). The output pulse duration is about 200 ns. The radiation hardness has been measured. The scintillator did not show any signal deterioration under a neutron dose of 10^{13} cm^{-3} [39]. The entrance surface of the scintillator is coated with a 200 nm thick aluminium layer which acts as a reflector. Table 8.2 shows that the critical velocity of the scintillators is quite high, above 4 m/s.

Chapter 9

Monte Carlo simulation of UCN detectors

9.1 Introduction

Monte Carlo simulations have been performed to investigate two types of UCN detectors: the cascade-U and the ^{6}Li-doped glass scintillators. The studies focus on the energy deposition and the detection efficiency. We also studied the possibility of stacking two ^{6}Li-doped scintillators (GSx). The GS3/GS20 and GS10/GS20 stacks are investigated.

9.2 Set-up of the simulations

9.2.1 Initial velocity distributions

The velocity distributions used in these simulations are based on measurements made at ILL/PF2.

Initial transverse component

As noted in chapter 7, the UCN velocity spectrum emitted in the peripheral direction of the turbine is wide ($\gtrsim 20$ m/s for $\alpha = 33°$ in Fig. 7.3). This implies that the strongest limitation over the transverse velocity component is given by the guide tubes used in the experiment. Typically, using stainless steel guide tubes (i.e. $v_c \approx$ 6 m/s) leads to a resulting transverse velocity spectrum limited at about 6 m/s. Figure 9.1(a) shows the initial transverse velocity component used in the simulations.

Initial longitudinal component

Experimentally, the longitudinal velocity distribution can be determined by performing time-of-flight measurements. Figure 9.1(b) shows the simulated initial distribution which is based on experiments made at ILL/PF2. Figure 9.2 plots the

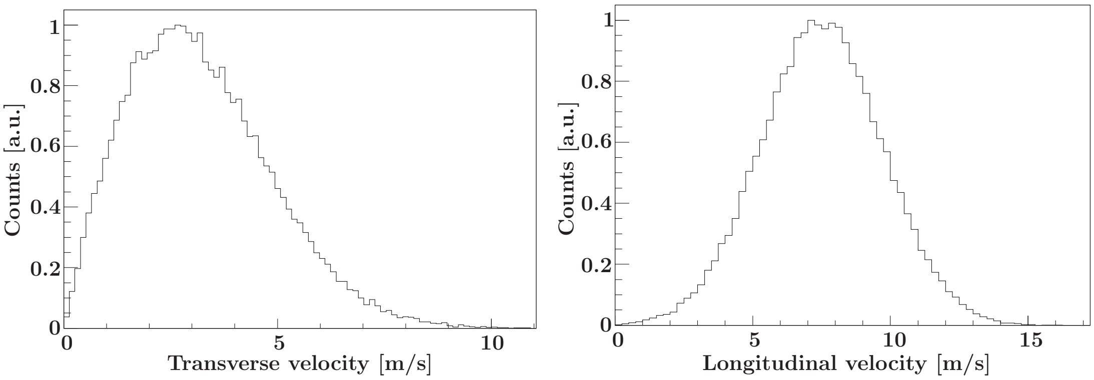

(a) Initial transverse component (b) Initial longitudinal component

Figure 9.1: (a) Initial transverse and (b) longitudinal velocity distributions in the simulations.

resulting longitudinal distribution at the time of detection (black line). The measured distribution is superimposed (circles). It has been obtained with a 500 μm thick GS10 scintillator detector at the TEST beamline.

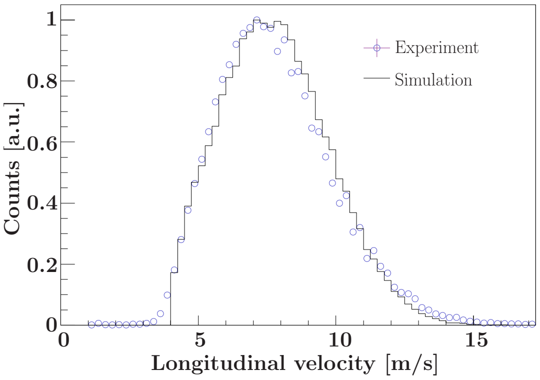

Figure 9.2: Longitudinal velocity distributions measured experimentally (circles) and obtained in the simulations with a GS10 detector (black line).

9.2.2 The physics of the UCN detection

The codes developed to simulate UCN interactions within a given detector material are based on the physical processes described in chapter 7. Materials (GSx, ^{10}B) are characterized by a set of properties: Fermi potential (V_F), loss factor (η), absorption cross section for thermal neutrons (σ_a^{th}). The latter is used to calculate the UCN absorption cross section σ_a from the $1/v$ law.

A UCN is shot according to the initial velocity distributions presented above. Then, at the detector surface, it may be reflected or transmitted. In the last case, absorption may occur with charged products emission:

- The reflection and transmission processes:
  Whether a UCN is reflected or transmitted depends on its velocity component

$v_\perp$ normal to the surface of the material. v_c is its critical velocity deduced from the parameter V_F.
- For $v_\perp \leq v_c$, the neutron is reflected according to equation (7.3.11). The loss probability is calculated from the loss factor η which depends on the material (cf. expression (7.3.12)).
- For $v_\perp > v_c$, the neutron still has a small probability to be reflected. Equation (7.3.11) is used for the calculation. The UCN is transmitted otherwise.

- The neutron capture:
  Inside the detector material, the absorption probability is calculated from the exponential law $1 - \exp(-N\sigma_a x)$, where N is the atomic density, σ_a the UCN absorption cross section and x the current depth of the neutron inside the material. In the following, $\ell_n = (N\sigma_a)^{-1}$ denotes the UCN mean free path. Note that the transmission from the media 1 to the media 2 modifies the normal velocity component such that $v_{\perp_2} = \sqrt{v_{\perp_1}^2 - v_c^2}$.

- Energy deposition of the charged particles:
  For the nuclei used in these simulations (i.e. ^{6}Li, ^{10}B), the resulting charged products are emitted in opposite directions. They release their energy according to their Bragg curve determined with SRIM calculations [85].

This algorithm has been used to simulate the UCN detection by the cascade-U detector and some GSx scintillators.

9.3 The cascade-U detector

As explained in chapter 8, the cascade-U detector has an entrance foil made of aluminium (100 μm thick). Directly onto the internal face of this foil, a thin layer of ^{10}B is deposited. The ^{10}B-crystal density of 2.16 g/cm^3 is used in the calculations. Considering the initial velocity distribution of Fig. 9.1, the UCN mean free path ℓ_n inside the ^{10}B layer is about 80 nm. Once the UCN is captured by a ^{10}B nucleus, charged fission products are emitted according to the reaction n(^{10}B,α)^{7}Li. Then they deposit their energy inside the Ar/CF$_4$ counting gas.

9.3.1 Energy deposition

In order to simulate the energy deposition within the ^{10}B, the Bragg curves of the α and ^{7}Li have been determined with the SRIM software [85]. Table 9.1 shows the mean ranges of these particles according to their energies in the reaction n(^{10}B,α)^{7}Li.

In the simulation, the α and triton particles travel a fixed distance according to the ranges given in table 9.1. When they escape from the boron layer to the counting gas, the Bragg curves are used to calculate the partial energy loss. The ranges of the (α,t) in the gas are lower than 7 mm. It is much smaller than the depth of the gas volume (~60 mm). Therefore, the particles are considered to deposit all their remaining energy once they penetrate inside the counting gas.

	^{7}Li		α	
Energy [MeV]	0.84	1.01	1.47	1.78
Mean range inside ^{10}B [μm]	1.8	2.1	3.6	4.4
Mean range inside Ar/CF$_4$ (1 bar) [mm]	~3	~3	~6	~7

Table 9.1: Results of SRIM calculations for the α and ^{7}Li inside the ^{10}B layer and the Ar/CF$_4$ counting gas.

Figure 9.3 shows the simulated energy deposition spectra for three boron layers. The widths of the peaks take into account an energy straggling (i.e. a mean-square deviation of the energy loss) inside the Ar/CF$_4$ counting gas. The Bohr formula is used to calculate the deviation [86, 87]:

$$\sigma_B^2 = 4\pi\, e^4 z^2 \overline{Z} N \Delta r, \tag{9.3.1}$$

with e the electron charge, z the atomic number of the projectile, $\overline{Z}$ is the mean atomic number of the target, N is the number of target atoms and Δr is the path within the Ar/CF$_4$ gas. It should be noted that this deviation of the energy loss is an upper limit. Moreover the media considered here is a gas (i.e. a small number of collisions). Consequently it is expected to have no important energy transfert of the ions. Therefore the energy straggling should be low. For example, an α with an energy of $E_\alpha = 1.78$ MeV has a path of ~7 mm in the gas. This gives a deviation of σ_B ~20 keV $\ll E_\alpha$. Thus the straggling has a negligeable effect on the energy deposition spectra.

For a boron layer of 50 nm, four peaks are clearly distinguishable. They correspond to the energies available by the reaction n(^{10}B,α)^{7}Li: 0.84, 1.01, 1.47 and 1.78 MeV. When the thickness increases, the energy loss of the α and the triton inside the ^{10}B layer becomes more important. This causes a shift towards the low energies for the thicknesses 200 and 800 nm.

9.3.2 The UCN detection efficiency

9.3.2.1 Influence of the ^{10}B thickness

Table 9.2 summarizes the percentages of losses and detected UCN for three boron layer thicknesses: 50, 200 and 800 nm.

It clearly reveals two main source of losses: i) the UCN may cross the ^{10}B layer without being captured; and ii) the charged particles, α or ^{7}Li, may not be able to escape from the ^{10}B layer, leading to no energy deposition within the gas. Both losses depend on the ^{10}B thickness. Figure 9.4 shows their variation as a function of the ^{10}B layer thickness.

An optimal range between 260 and 300 nm is obtained for a minimal loss percentage of about 11%. Adding the unavoidable losses due to the reflection and transmission through the aluminium foil (about 7%), the absolute efficiency of the cascade-U detector is found to be about 82% at best [88]. This result is highly dependent on the initial velocity distribution.

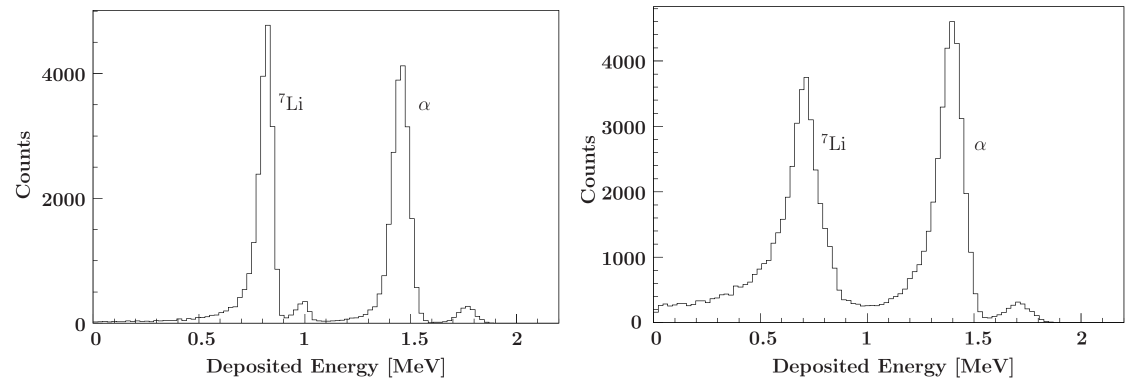

(a) For a boron layer of 50 nm

(b) For a boron layer of 200 nm

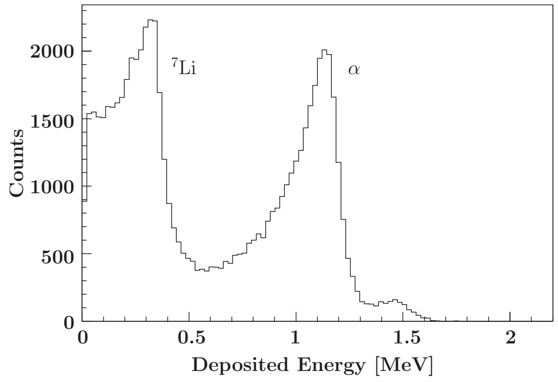

(c) For a boron layer of 800 nm

Figure 9.3: Energy deposition spectra for three different boron layers.

9.3.2.2 Efficiency vs velocity

Following the previous remark, it is interesting to study the absolute detection efficiency as a function of the longitudinal velocity (see Fig. 9.5). For a ^{10}B thickness of 50 nm, the maximum efficiency achieved is only about 60%. This is due to the UCN which go through the layer without interacting with a ^{10}B nucleus. The fact that the efficiency decreases when the velocity increases is due to the $1/v$ dependence of the absorption cross section σ_a. For thicker boron layers, the maximum efficiency increases until about 85% for 200 nm (about the optimal thickness). When the boron layer thickness increases again, the second loss mechanism becomes important. The neutrons have to interact deeply within the boron layer to enable the fission products to escape. On average, the larger the UCN velocity the higher the efficiency.

9.4 The GSx scintillator detectors

9.4.1 Preliminary calculations

GSx glass scintillators are doped with ^{6}Li which has an absorption cross section of a few 10^5 barns at UCN energies. The neutron capture reaction leads to the

	50 nm	200 nm	800 nm
UCN lost by reflection on Al or ^{10}B	3.2	3.3	3.2
UCN lost in Al	3.6	3.6	3.5
UCN lost by transmission through Al+^{10}B	**49.1**	8.2	0.0
Non-escaping α and ^{7}Li events	0.6	4.8	**27.1**
Detected UCN	43.6	80.2	66.2

Table 9.2: Results of the Cascade-U simulations. Numbers are percentages of the total number of UCN shot in the simulations.

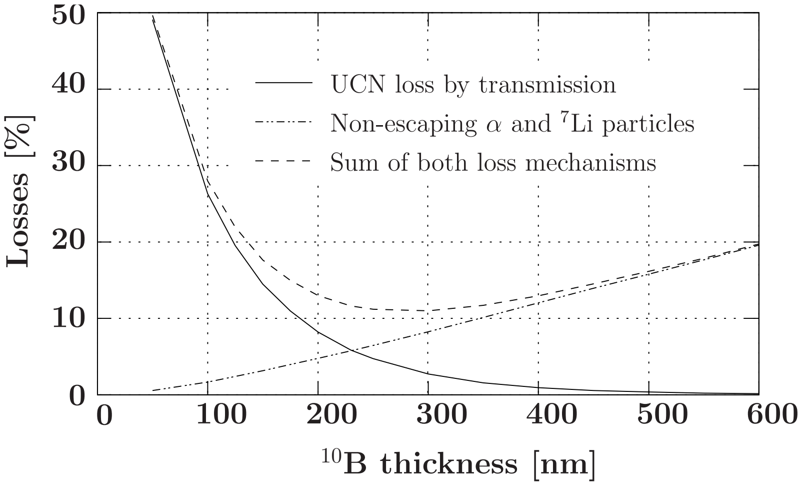

Figure 9.4: Percentage of UCN losses as a function of the ^{10}B layer thickness.

production of an alpha of 2.05 MeV and a triton of 2.73 MeV. Table 9.3 shows their ranges within a GSx glass obtained with the SRIM software [85]. The path of the alpha ℓ_α is six times lower than that ℓ_t of the triton.

	α	triton
Energy [MeV]	2.05	2.73
Mean range [μm]	6	36

Table 9.3: Results of SRIM calculations for the α and triton inside a GSx glass.

During our experiments, three types of scintillator have been tested: the GS3, GS10 and GS20. The main difference between them is the ^{6}Li enrichment which is respectively 0.01%, 7.5% (i.e natural lithium content) and 95% of the whole lithium content (cf. table 8.2). Experimentally, the 100 μm thick GS10 is about 25-30% less efficient than the 500 μm thick GS10 (see the next chapter). In contrast, the simulations with a ^{6}Li content of 7.5% show that 100 μm of GS10 is sufficient to stop about 97% of the neutrons (with a similar velocity distribution than in the experiment). As a result, a ^{6}Li content of 3.4% instead of 7.5% has been used in these simulations for the GS10 in order to better reproduce the experimental

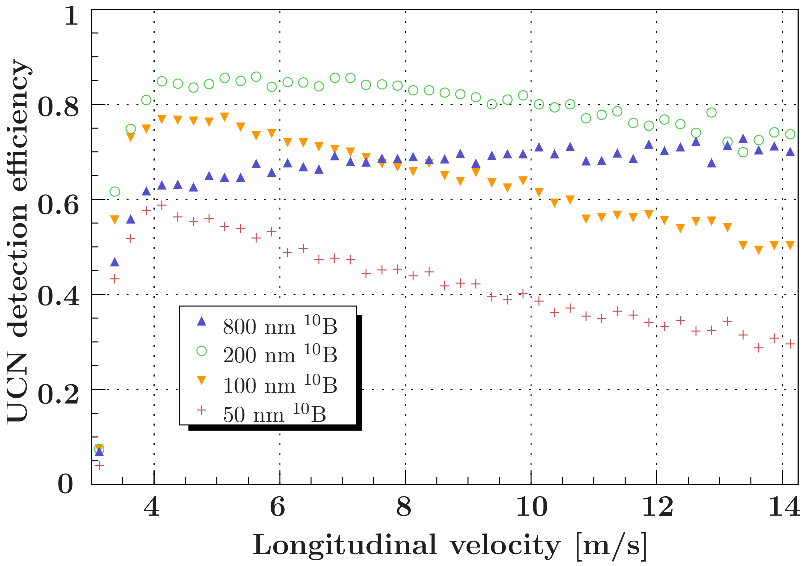

Figure 9.5: Cascade-U detection efficiency as a function of the UCN longitudinal velocity calculated for different boron layer thicknesses.

observations. The other contents are unchanged. Table 9.4 shows the UCN mean free path inside three GSx scintillators for the initial conditions given in section 9.2.1.

	GS3	GS10	GS20
UCN mean free path ℓ_n [μm]	$6 \cdot 10^4$	50	2

Table 9.4: UCN mean free path in three GSx scintillators. The initial velocity distribution is given in Fig. 9.1. The GS10 has a ^{6}Li content of 3.4%.

The ranges of the (α,t) particles (see table 9.3) and the UCN mean free path in the GS3, GS10 and GS20 glasses (see table 9.4) can be compared. For the GS20, the α and triton will often escape from the entrance surface since ℓ_n(GS20) is smaller than their ranges. It will still be the case for the GS10, but in a less important way. For the GS3, a thicker glass (i.e. a few centimeters) has to be chosen to be efficient for UCN detection. In that case, both alpha and triton will be stopped within the scintillator (except for the few UCN captures close to the surfaces).

9.4.2 Energy deposition

9.4.2.1 Single scintillators

Figure 9.6 shows the energy deposited inside GS10 and GS20 scintillators. Realistic parameters have been taken in the simulations: resolutions of 10% for the entire detectors (i.e. scintillator plus photomultiplier) (cf. section 10.6.1.1), and thicknesses about several hundred of microns. The *edge events* correspond to neutron captures occuring close to the entrance of the detectors: the alpha or triton particles may escape from the glass. When both are stopped within the scintillator, a full energy deposition is recorded at 4.78 MeV. For the GS10, the amount of edge events represents about 13% of the total number of neutron detected. For the GS20, it is about 78%. Moreover, more triton particles are escaping from the GS20 since it has a longer range than the alpha.

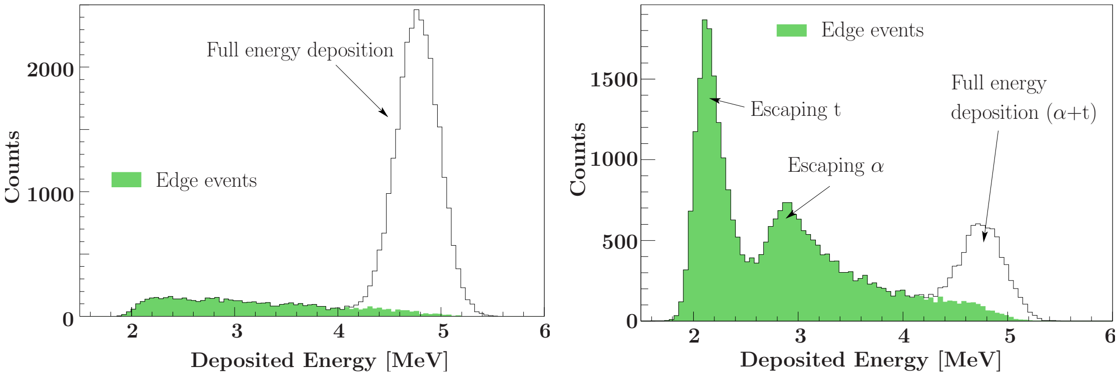

(a) 500 μm thick GS10 (b) 100 μm thick GS20

Figure 9.6: Energy deposition spectra for GS10 and GS20 scintillators. The GS10 has a ^{6}Li content of 3.4%.

Figure 9.7 shows the UCN capture depth as a function of the energy deposition within the scintillators. The proportion of edge events within the GS10 is less important than inside the GS20. UCN interact more deeply ($\ell_n(\text{GS10}) > \ell_n(\text{GS20})$) leading to more full energy events. For the GS20, UCN are captured mainly close to the entrance face. Since the alpha particles have a smaller range than the tritons, they can deposit almost all their energy. That explains why more counts are recorded for them than for the tritons.

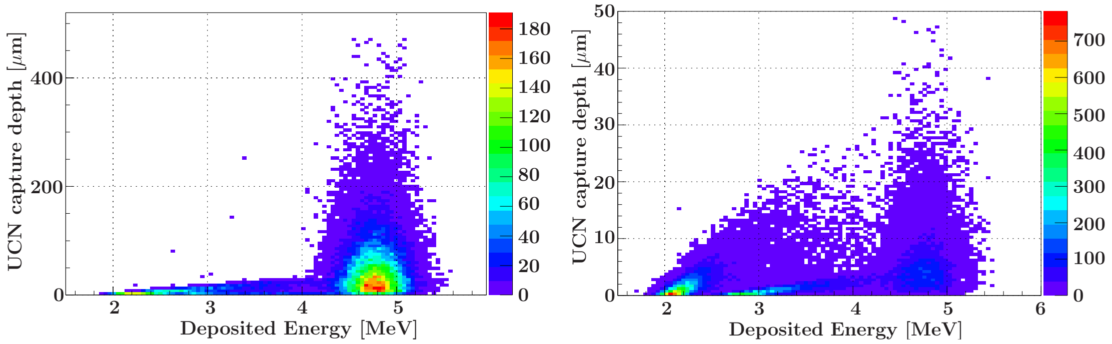

(a) 500 μm thick GS10 (b) 100 μm thick GS20

Figure 9.7: UCN capture depth as a function of the energy deposition for GS10 and GS20 scintillators. The GS10 has a ^{6}Li content of 3.4%.

9.4.2.2 The GS3/GS20 scintillator stack

The energy released after a neutron capture by a ^{6}Li nucleus is quite large (4.78 MeV). But in pratice, the edge events may be merged at low energies with electronic noise and gamma radiations. It is then difficult to recognize the neutron signal in this region. To solve this problem, a bilayer scintillator has been proposed. Its goal is to get back the energy of the escaping charged particles.

Figure 9.8 shows a scheme of a GS3/GS20 stack. The system is made of two scintillator layers: the first one is a GS3 which is almost transparent to UCN ; the second one is a GS20 which performs the neutron capture. Both thicknesses are equal to 100 μm (1). With this set-up, if a fission product (α, t) escapes from the GS20, it is then stopped in the GS3 such that one may measure the whole deposited energy. The edge event contribution will therefore be suppressed.

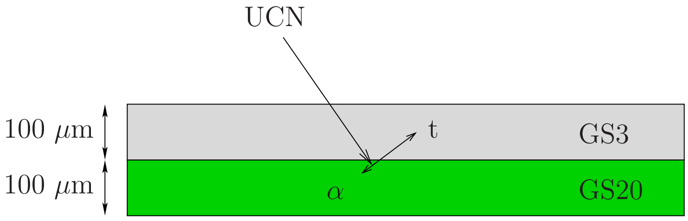

Figure 9.8: Scheme of a UCN capture within a GS3/GS20 bilayer scintillator.

Figure 9.9 shows the simulated energy deposition in a GS3/GS20 stack where both layers have a thickness of 100 μm. The contact between the scintillators is supposed to be perfect: no surface profile nor contact defects (gap) are considered. The energy distribution within the GS20 glass is similar to that presented in Fig. 9.6(b). About 77% of the UCN captures lead to escaping alpha or triton particles. More tritons escaped from the GS20 since they have a longer path. As a result, the alpha peak (2.05 MeV) is higher than the triton one (2.73 MeV). The deposited energy distribution inside the GS3 is mirrored from that of the GS20. It stops all the escaping particles. Finally, by summing both contributions, almost all the events are found about 4.78 MeV. Therefore, the amount of edge events can be decreased and the UCN/gamma discrimination may be improved by this way. Further experimental tests are presented in the next chapter.

9.4.3 Velocity dependence of the energy deposition

From a general point of view, the velocity dependence of a detector could be interesting for nEDM experiments where some systematic effects are velocity-dependent (see chapter 6). Whereas a standard time-of-flight set-up is difficult or impossible

---

(1) Note that, in principle, a GS10 could also work as a second scintillator layer. But due to its longer UCN mean free path (50 μm) compared with GS20 (2 μm), its thickness should be larger than 100 μm in order to get the maximum UCN efficiency. As discussed in the next chapter, a larger thickness implies more gamma interactions.

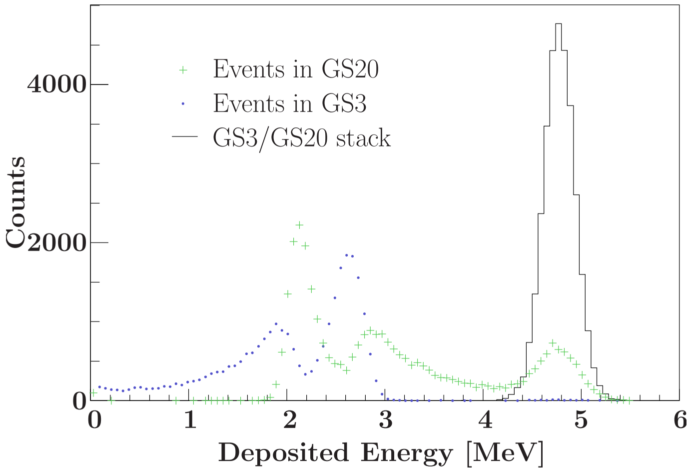

Figure 9.9: Deposited energy spectra in the bilayer scintillator GS3/GS20. The energy deposition inside the GS20 (crosses) and GS3 (dots) are plotted. The black line is the resulting deposition inside the GS3/GS20 stack.

to implement due to geometry considerations, a detector sensitive to UCN velocity could be very useful.

9.4.3.1 Single scintillators

The first way to study the velocity dependence of the energy deposition may be to plot directly the energy deposition as a function of the longitudinal velocity distribution. Figure 9.10 shows this 2D histogram for a 500 μm thick GS10 and a 100 μm thick GS20 scintillators.

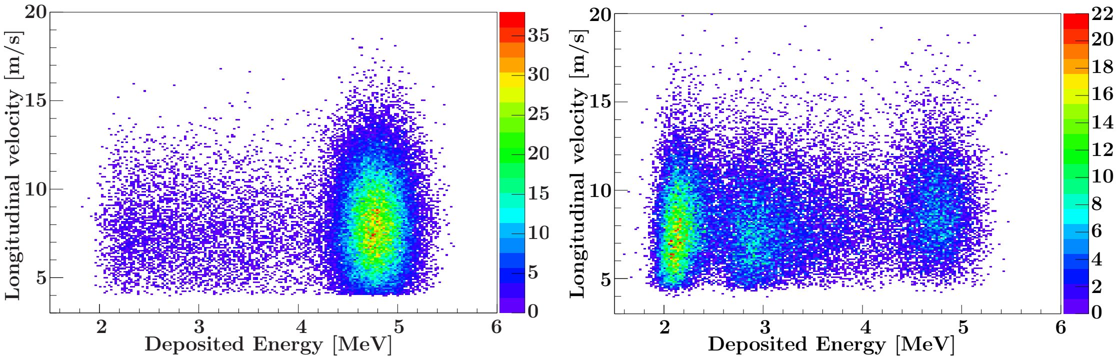

(a) 500 μm thick GS10
(b) 100 μm thick GS20

Figure 9.10: Longitudinal velocity as a function of the energy deposition for GS10 and GS20 scintillators. The GS10 has a ^{6}Li content of 3.4%.

For the GS10 glass, the edge events spread on the range 4-12 m/s whereas the full energy events are located within 4-16 m/s roughly. The faster neutrons interact more deeply and lead to a deposition of 4.78 MeV. Thus there is a slight velocity dependence. For instance, one may imagine that the edge events would correspond to the lower velocity neutrons, say in the range 4-12 m/s, and the full energy events would be located between 12 and 16 m/s. This is obviously not the case since UCN interact randomly with respect to an exponential law. In the case of the GS20, the edge events cover the full velocity range 4.4-16 m/s. The full energy peak is slightly shifted towards the high velocities as compared with the edge events. Therefore the counts between 4.4 and 5.5 m/s can be considered to be mainly edge events (i.e. deposition between 2 and 4 MeV).

Another way to investigate the velocity dependence of the energy deposition is to change the initial velocity distribution. Figure 9.11 shows the three velocity distributions used.

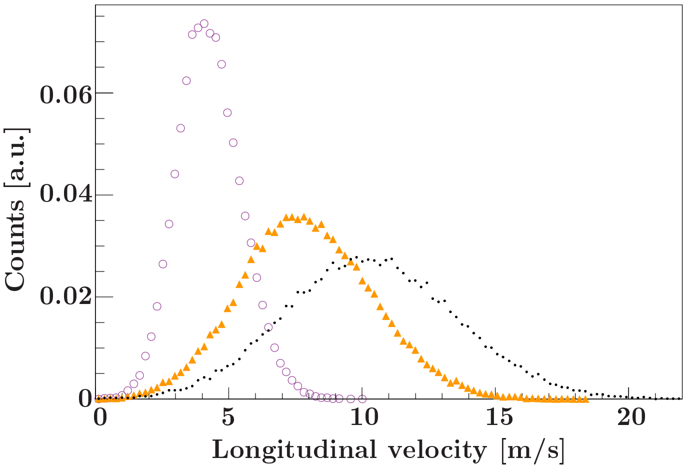

Figure 9.11: Initial longitudinal velocity distributions used to study the velocity dependence.

The slower distribution has a maximum at 4 m/s and spreads until 8 m/s. The medium one is located about 8 m/s and vanishes at 16 m/s (this is the standard distribution in the previous calculations). The higher velocity spectrum is about 10 m/s with velocities until 20 m/s. They are normalized to unit area.

Figure 9.12 shows the corresponding energy depositions for these three velocity distributions and for both GS10 and GS20 scintillators. They are also normalized to unit area.

No significant change in the energy deposition can be seen for the GS10 glass. In contrast, the UCN have a short mean free path inside the GS20 (about 2 μm); the amount of egde events is consequently very sensitive to a change in the incoming velocity spectrum. Table 9.5 gives the number of edge events as a percentage of the total number of UCN detected. The ratio between the number of edge events and the amount of events which give a complete deposition (at 4.78 MeV) is calculated.

For both detectors the amount of edge events varies as a function of the velocity distribution. The slower it is, the more edge events are recorded within the detector. Most of the UCN interact deeply inside the GS10 (the ratio edge/full is lower than

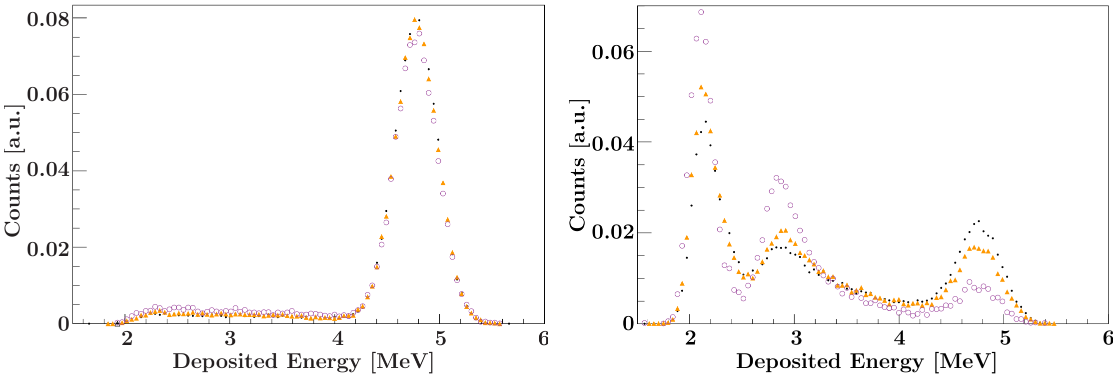

(a) Corresponding deposited energy spectra (b) Detected velocity distributions

Figure 9.12: Energy depositions for a 500 μm thick GS10 and a 100 μm thick GS20 scintillators. ∘-markers denote the lower velocity distribution with mean velocity close to 4 m/s, ▴-markers for the intermediate one with mean velocity about 8 m/s and ▪-markers for the higher distribution with mean velocity about 10 m/s. The GS10 has a ^{6}Li content of 3.4%.

	GS10(∘)	GS10(▴)	GS10(▪)	GS20(∘)	GS20(▴)	GS20(▪)
Edge events [%]	16.8	12.7	11.0	92.8	83.3	77.7
Ratio Edge/Full	0.2	0.14	0.12	12.5	5	3.4

Table 9.5: Amount of edge events for the three velocity distributions presented in Fig. 9.11.

0.2). That explains why there are no significant effect depending on the velocity distribution. In contrast, most of the UCN detected inside the GS20 are due to edge events (the ratio edge/full is higher than 3).

9.4.3.2 The GS10/GS20 scintillator stack

Velocity measurement

Monte-Carlo simulations of a GS10/GS20 stack have been performed to investigate the velocity dependence of its energy deposition. Since each scintillator has a different ^{6}Li content, their UCN efficiency is different. This has been shown in Fig. 9.16 for single GS10 and GS20 glasses. The detection efficiency of the 100 μm thick GS10 is dependent on the UCN velocity, being more efficient for low than for high velocities. Therefore, in a GS10/GS20 stack, the GS10 layer would be more sensitive to neutrons with a small velocity and the GS20 would capture those with a higher one.

Figure 9.13 shows the proportion of UCN which are captured inside the stack either in the GS10 or in the GS20 layer. Most of the UCN are stopped within the GS10, but as the velocity increases, more UCN are detected in the GS20. Due to the different critical velocities, UCN with velocities between 4 and 4.4 m/s are all detected by the GS10. Beyond, the amount of neutrons detected by the GS20

(GS10) increases (decreases) with the UCN velocity. Therefore, each layer may have a different efficiency depending on the velocity region. The problem now is

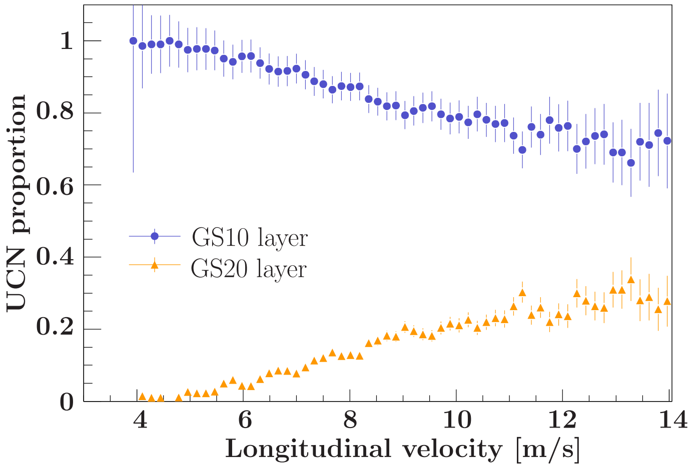

Figure 9.13: Fraction of UCN which are captured either in the GS10 (dots) or in the GS20 (triangles). The GS10 has a ^{6}Li content of 3.4%.

if this slight velocity dependence can be measured through the energy deposition distribution.

Velocity dependence of the energy deposition

The longitudinal velocity as a function of the energy deposition is shown in Fig. 9.14.

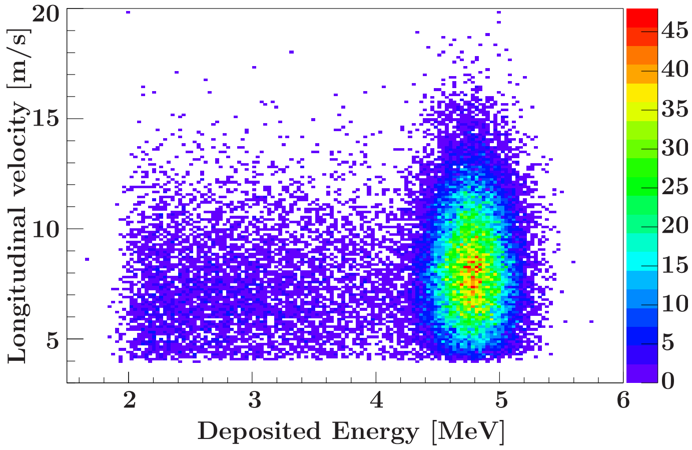

Figure 9.14: Longitudinal velocity vs energy deposition for the GS10/GS20 stack. The GS10 has a ^{6}Li content of 3.4%.

Most of the UCN are captured within the GS10 glass (~ 83%). As a consequence, the pattern is similar to that in Fig. 9.10. The edge events are located in the range

4-12 m/s. Most of the neutrons with longitudinal velocities above 12 m/s lead to a full energy deposition. However, it is not possible to see any velocity-dependent effect in the deposited energy distribution.

Figure 9.15(b) shows the energy deposition obtained with the three velocity distributions about 4, 8 and 10 m/s (Fig. 9.15(a)). For the low velocity distribution (mean about 4 m/s), 98% of the UCN are captured within the GS10. Between the two higher velocity distributions, the difference in energy deposition is slight and comes from the fact that the number of interactions in the GS20 glass is about 65% more important from the intermediate velocity distribution to the higher one. The ratio between the amount of edge events and the full energy events is found to be 0.48, 0.23 and 0.16, respectively for the velocity distributions with means about 4, 8 and 10 m/s.

Thus some velocity dependence should be measurable, but it will not be interesting if one wants to be sensitive at the meter par second or lower.

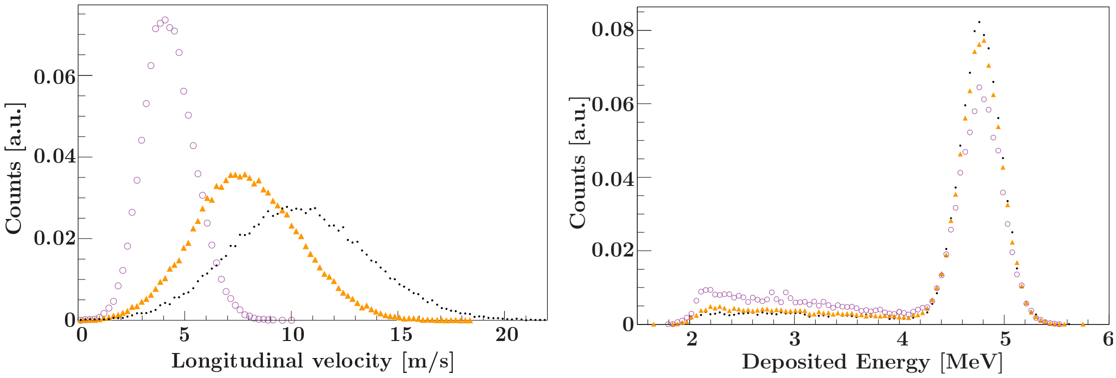

(a) Detected velocity distributions (b) Corresponding deposited energy spectra

Figure 9.15: Energy deposition (b) for different velocity distributions (a) in a GS10/GS20 stack. The GS10 has a ^{6}Li content of 3.4%.

9.4.4 Detection efficiency

9.4.4.1 Single scintillators

Figure 9.16 shows the calculated detection efficiencies for both GS10 and GS20 scintillators.

The value of the GS10 critical velocity is 4 m/s whereas for the GS20, it is equal to 4.4 m/s (see table 8.2). As a result, the GS10 is more efficient at low velocities than the GS20 scintillator.

The detection efficiency of the GSx scintillator depends on their thickness. This is especially true for the glasses which have a low ^{6}Li density (i.e. natural and depleted types). Within a GS10, the UCN mean free path is about 50 μm (see table 9.4). Therefore, a 100 μm thick and a 500 μm thick GS10 do not have the same detection efficiency at high velocities. In the case of the 100 μm thick GS10, UCN may cross the scintillator without being captured by a ^{6}Li nucleus. It is not the case for a 500

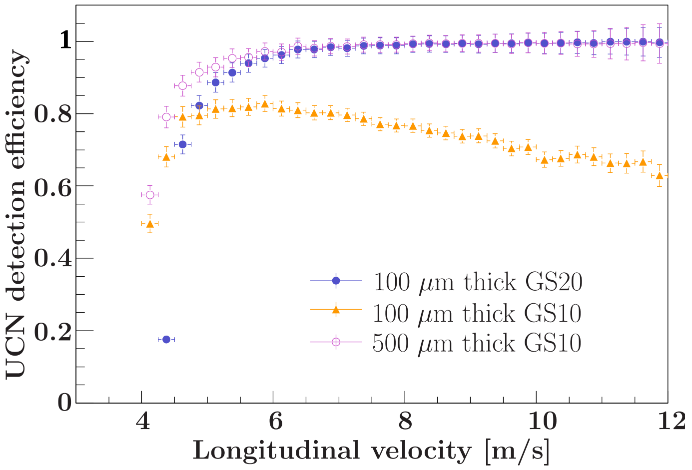

Figure 9.16: Detection efficiency of GS10 and GS20 as a function of the UCN velocity. Thicknesses are 100 and 500 μm for the GS10 and 100 μm for the GS20 glass. The initial velocity distribution is given in Fig. 9.1. The GS10 has a ^{6}Li content of 3.4%.

μm thick GS10. In the case of the GS20, the UCN mean free path is so small (2 μm) that its detection efficiency does not depend on the thickness. This holds for the initially simulated velocity distribution.

Table 9.6 summarizes the results about the detection efficiency for GS3, GS10 and GS20 scintillators. The amount of edge events is also shown. Again, the initial velocity distribution is that of section 9.2.1.

	GS3	GS10	GS10	GS20
Thickness [μm]	100	100	500	100
Detection efficiency [%]	1.8	71.4	91.7	89.0
Amount of edge events [%]	20	21	13	78

Table 9.6: Detection efficiency of GSx scintillators. The initial velocity distribution is given in Fig. 9.1. The GS10 has a ^{6}Li content of 3.4%.

Since the UCN mean free path inside the GS3 scintillator is about 6 cm, a thickness of 100 μm of this glass can be considered as transparent. Only 1.8% of UCN are captured. Several hundred of microns of GS10 or GS20 glass are sufficient to detect UCN. Detection efficiencies about 90% can be obtained for both. For the GS20, 78% of this absolute efficiency comes from the edge events. In contrast, it is only 13% for the 500 μm thick GS10 meaning that most of the events occur in the full energy peak at 4.78 MeV.

9.4.4.2 Bilayer scintillator

Table 9.7 show the detection efficiencies of the GS3/GS20 and GS10/GS20 stacks integrated over the whole velocity distribution.

Thickness [μm]	GS10/GS20 100/100	GS3/GS20 100/100
Detection efficiency [%]	91.6	89.1
Amount of edge events [%]	20.6	0.4

Table 9.7: Detection efficiency of GS3/GS20 and GS10/GS20 stacks. The initial velocity distribution is given in Fig. 9.1. The GS10 has a ^{6}Li content of 3.4%.

The GS20 layer of the GS10/GS20 stack compensates the lack of efficiency of the 100 μm thick GS10. As a result, an efficiency of about 92% is found, which is similar to the single 500 μm thick GS10. Nevertheless, the GS10/GS20 stack still has 21% of edge events. That is why the GS3/GS20 is interesting. There is no edge events due to the transparency of the GS3 layer. In addition, the detection efficiency is about 90% thanks to the GS20 glass. Unfortunately, it has a critical velocity of 4.4 m/s, which makes it less sensitive about 4-5 m/s than the GS10/GS20 stack. That explains the slight difference in detection efficiency between both stacks.

9.4.5 Conclusions

The Monte-Carlo simulations give a preliminary understanding about the detectors tested experimentally. A velocity distribution similar to that available for the experimental measurements has been simulated. The detection efficiency of the cascade-U detector is limited by the boron layer. The maximum value has been calculated and is equal to 82% for ^{10}B thicknesses in the range of 260-300 nm. Efficiencies of about 90% can be achieved with a 500 μm thick GS10 or a 100 μm thick GS20 scintillators. The simulations have shown that a GS3/GS20 stack would enable to get the full energy deposition (4.78 MeV) for all UCN events with an efficiency of about 90% for the considered initial velocity distribution. In the next chapter, we will refer to these simulations to compare with the experimental results.

Chapter 10

Experimental tests of UCN detectors

10.1 Introduction

Tests at ILL/PF2 have been carried out in order to study three types of detectors: the cascade-U detector, the ^{3}He gas detector and the ^{6}Li-doped glass scintillator (GS family). They have been compared with respect to their detection efficiency and their background sensitivity. Tests with scintillator stacks are also described.

10.2 Experimental set-up

Figure 10.1 shows the scheme of the set-up for the detector tests.

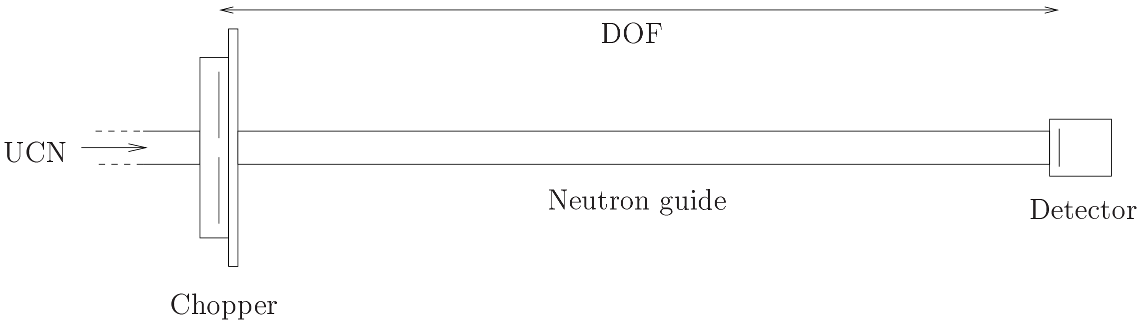

Figure 10.1: Scheme of the set-up for the detectors comparison.

Most of the measurements presented below used a chopper to determine the time-of-flight (TOF) distribution and then the velocity distribution at the TEST or EDM beamlines. A polyethylene collimator (5 mm thick) is placed at the entrance of the detector for the efficiency comparison.

Figure 10.2 shows the detector housing for the 3-inches diameter scintillators. No light guide have been used between the scintillators and the PMT. In most of the tests, an aluminium layer of 200 nm has been evaporated onto the entrance surface of the glass scintillator. It behaves as a light reflector. The signal from the PMT is amplified and then coded by a QDC or an ADC (1).

---

(1) The main conclusions obtained for the scintillators are the same whatever the coder used (ADC

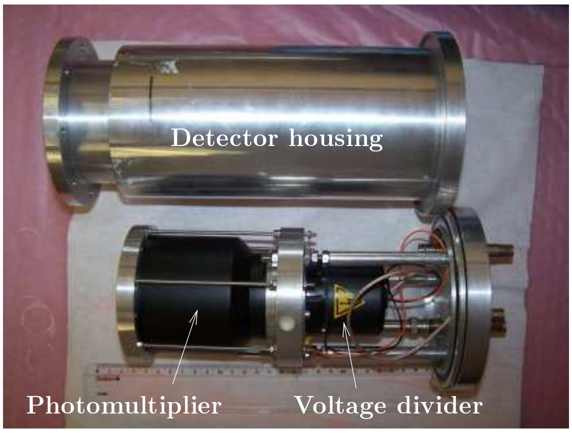

Figure 10.2: Set-up of the scintillator detectors.

The ^{3}He gas detector and the cascade-U are described in chapter 8. Their signal are amplified and coded through an ADC.

10.3 Time-of-flight measurements

The TOF measurements consist in measuring the time during which the neutrons travel a given distance, namely the distance-of-flight (DOF). The start of the measurement corresponds to the opening of a beam chopper. The stop is given by the neuton detection. The velocity can then be extracted. Note that only the *longitudinal* velocity component is measured with this technique since one knows the longitudinal DOF only (and not the entire path of the UCN inside the guide tubes).

10.3.1 Description of the chopper

A chopper manufactured by PSI has been used during our tests [89]. It is made of three rotating polycarbonate discs mounted within an aluminium vacuum housing. Two of them rotate in opposite directions with the same frequency and the same opening angle of 120°. The third one is slower (by a factor of 1/6) with an opening angle of 56°. Two rotation axes are located symmetrically at about 80 mm from the center of the neutron guide — one holds the slow and a fast disc. A picture of the chopper is shown in Fig. 10.3.

The discs are driven by a stepping motor (864 steps). Its frequency can be controlled by a dedicated LabView application. The coincidence between the opening of the three discs is monitored by a photosensor which generates a TTL pulse every rotation. The pulse triggers a positive ramp with a frequency slightly higher than that of the chopper. This ramp is then sampled by an ADC812F which is triggered at each neutron detection.

---

or QDC)

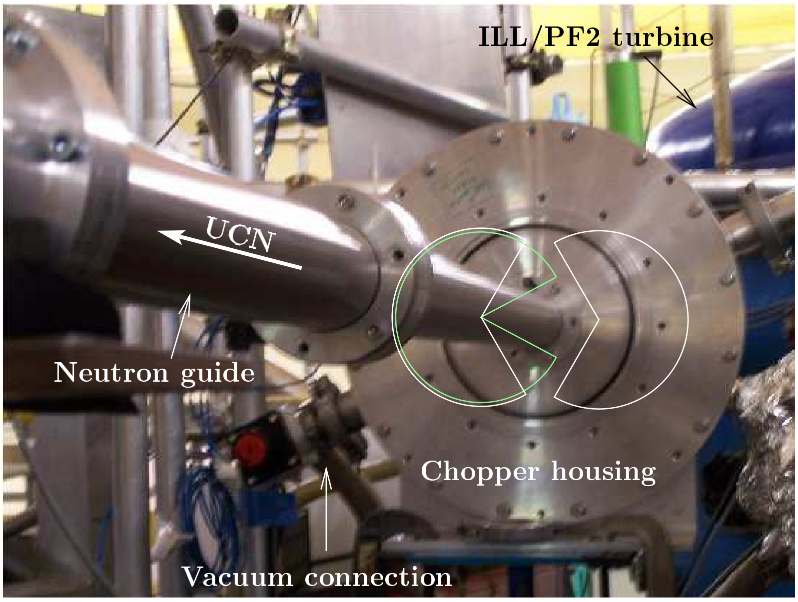

Figure 10.3: The PSI chopper installed at ILL/PF2 TEST beamline.

10.3.2 TOF calibration and velocity determination

The ramp which codes the TOF is digitized over 12 bits, i.e. 4096 channels. By knowing the chopper frequency, it is then possible to translate the channel data into time data. Nevertheless, the TTL signal which initiates the coding ramp is not sent at the same time than the opening of the chopper. A time offset has to be determined in order to measure the actual TOF of the neutrons. This can be done by turning the stepping motor at a low frequency, about 5-20 mHz. As a result, the TOF of each neutron cannot be well discriminated since the chopper turns too slowly. But it is now possible to deduce the characteristics of the chopper opening, i.e. its duration and starting time. Figure 10.4 shows the TOF measurement obtained with a motor frequency of 5.79 mHz. Two openings are visible. The duration of the chopper opening is $2\Delta t = 6.8$ s, where Δt denotes half of the opening window. The new starting time is taken at the middle of the neutron burst. Therefore, the measured time has to be corrected by the difference between the middle of the pulse and the TTL signal. This offset equals to 1.8 s in Fig. 10.4.

To determine the neutrons velocity, the chopper frequency is tuned to 0.81 Hz. This leads to a chopper opening every 1.23 s with $\Delta t \approx 0.024$ s. This last number corresponds to the error of the neutron TOF due to the opening duration. At the chopper velocity of 0.81 Hz, the offset between the middle of the burst and the TTL signal is about 12.8 ms. Thus, the longitudinal velocity component $v \pm \Delta v$ can be determined as:

$$v = \mathrm{DOF}/t \qquad \text{and} \qquad \Delta v = v\Delta t/t, \tag{10.3.1}$$

with t the corrected TOF.

Figure 10.5 shows the time-of-flight measurement with the chopper rotating at 0.81 Hz. Calibrated TOF is given in Fig. 10.5(a) and the corresponding velocity

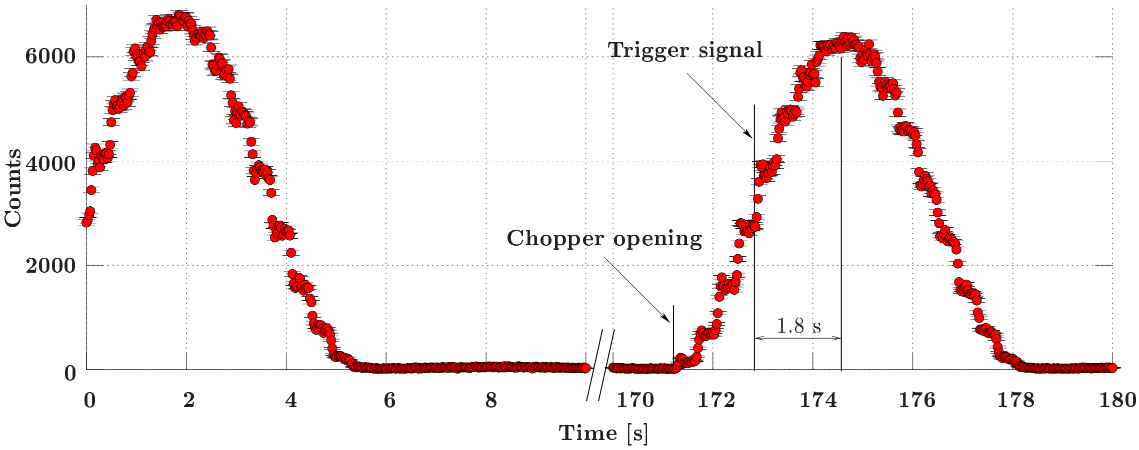

Figure 10.4: TOF spectrum with two neutron bursts. The chopper frequency is 5.79 mHz.

spectrum in Fig. 10.5(b). Note that the background subtraction has not been performed for these spectra.

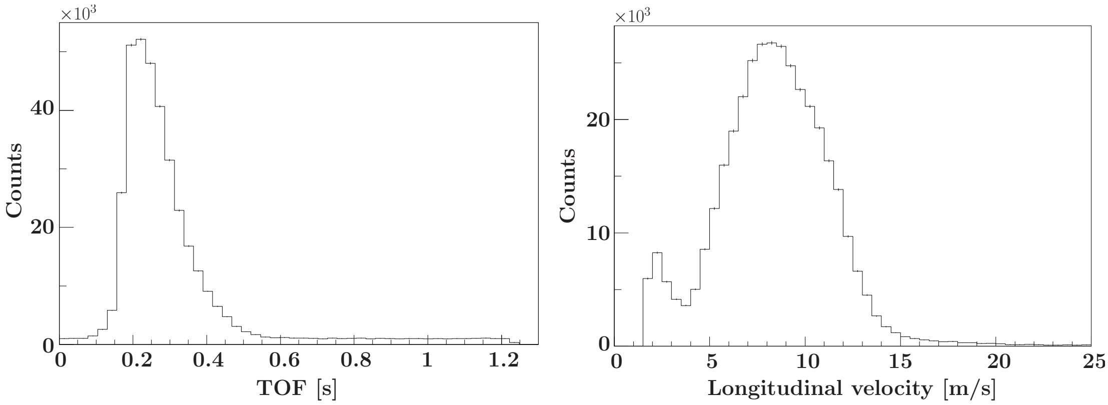

(a) (b)

Figure 10.5: TOF spectrum (a) and deduced velocity distribution (b) obtained with a chopper frequency of 0.81 Hz on the TEST beamline.

10.4 The data acquisition system

The data are stored via the GANIL Data Acquisition Sytem (DAS v6.03) [90].

The signal from the detector first passes through a discriminator and triggers the MCR Ganil module for fast coincidences [35]. It controls the whole system by validating or vetoing the acquisition. This means that a neutron detection is treated only if the MCR has emitted a validation gate (named FC). This gate is stretched and used as input for the coder of the amplified detector signal.

The signal from the gas detectors is amplified through a spectroscopy amplifier and coded through an ADC (12-bits ADC812F [35]). In the case of the scintillators, integration via a QDC (LeCroy 4300B FERA) has been used most of the time. ADC digitization has been also used with no difference between both methods.

The ADC812F also codes the signal from the TOF measurement. Since it is the slowest module, it initiates the acquisition process. The data (i.e. digitized detector signal and TOF signal) are finally transfered to the computer via a VME bus.

10.5 Data analysis and background subtraction

Figure 10.6 illustrates the method of background subtraction for a 100 μm thick GS10 (not shielded).

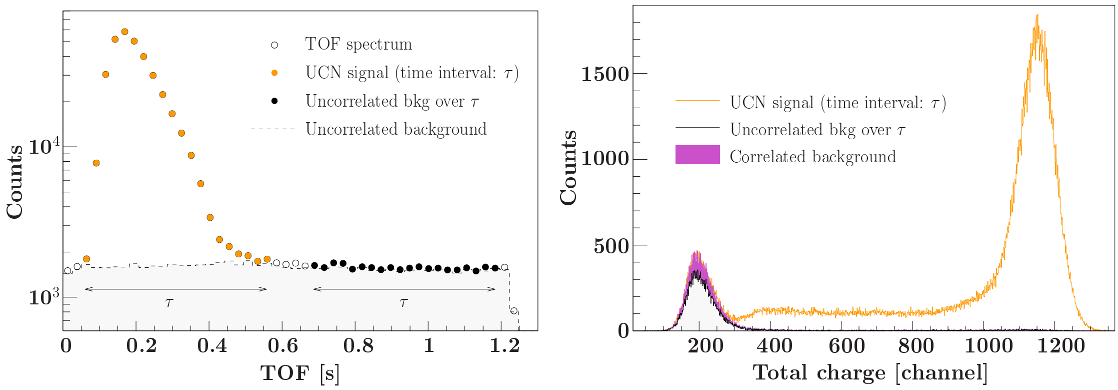

(a) (b)

Figure 10.6: (a) The TOF spectrum is made of three components: the UCN burst, the background uncorrelated with it (flat distribution) and the correlated one. (b) Corresponding total charge distributions over the same time range τ. This experimental test has been performed on the ILL/PF2 EDM beamline with a 100 μm thick GS10 scintillator detector (not shielded).

The TOF distribution in Fig. 10.6(a) shows two contributions for the background. The first one is not correlated to the neutron burst. It is present all the time. As a result, it appears as a flat distribution in the TOF spectrum. The second contribution comes with the neutron burst.

The black curve in Fig. 10.6(b) corresponds to the charge distribution of the uncorrelated background. It has been selected in the flat region of the TOF distribution over τ. It mainly consists in gamma events with a low charge. Thermal neutrons are also observed for larger charge but their contribution is much lower.

The estimation of the correlated gamma background is performed by subtracting the uncorrelated background to the neutron burst. This holds only at low charge where the gamma contribution is located. Note that the charge spectrum of the neutron burst in Fig. 10.6(b) has been obtained by selecting the events over the same time period τ than for the uncorrelated charge distribution. Thus the subtraction leads to the gamma events correlated with the neutron burst. In the case presented here, they represent about 2% of the total number of counts in the whole signal.

This contribution is more important for a thicker GS10 (500 μm thick). It is almost negligeable for the gas detectors since there they are almost insensitive to gamma background.

Figure 10.7 shows the cleaned distributions (velocity and total charge) obtained for the 100 μm thick GS10 detector.

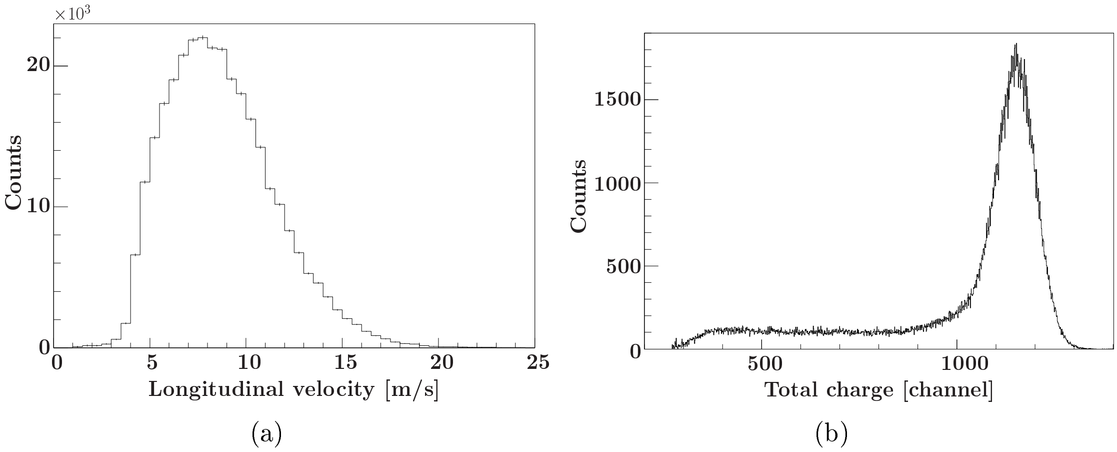

(a)

(b)

Figure 10.7: Velocity (a) and charge (b) distributions obtained after background subtraction.

10.6 Energy deposition study

10.6.1 The ^{6}Li-doped glass scintillator (GSx)

The advantage of ^{6}Li-doped glass scintillators is the large amount of energy released from the neutron capture: 4.78 MeV is deposited when both reaction products are stopped within the glass. Another point is the effect of the gamma background which is present near UCN sources. The best neutron/gamma discrimination is needed. For ^{6}Li-doped glasses, it has been noted that a gamma of 1.5 MeV produces the same amount of photons than for an energy deposition of 4.78 MeV resulting from a neutron absorption [41]. Nevertheless, it should be noted that the range of the electrons produced by the gammas is larger than the detector thickness. For the GS scintillators, simulations with Casino [42] have shown that the range of 1.5 MeV electrons is about 2.2 mm. Thus, the gamma contribution is reduced for glasses with thicknesses of several hundred of microns.

It was demonstrated in [39] that among the single GSx scintillators, the GS10 was the most convenient for UCN counting. It has the lowest critical velocity (v_c = 4 m/s) and therefore a high detection efficiency at low velocities (below 6 m/s). In addition, its ^{6}Li density (naturally doped) enables to get a low number of edge events and then a relatively good discrimination between UCN and gamma rays.

10.6.1.1 Single scintillators

GS3, GS10 and GS20 scintillators

Figure 10.8 shows the amplitude distributions obtained with GS3, GS10 and GS20 scintillators. The three glasses have a thickness of 100 μm. In these tests, no aluminium has been evaporated on their entrance face. For the GS10 and GS20, optical grease (silicone) has been used at the interface between the glass and the photocathode of the PMT. The measurement has been made on the ILL/PF2 EDM beamline with no chopper. The velocity spectrum has been slowed down by using curved guides. Note that this same set-up has been mounted on the TEST beamline with a chopper; the maximal longitudinal velocity was about 10 m/s.

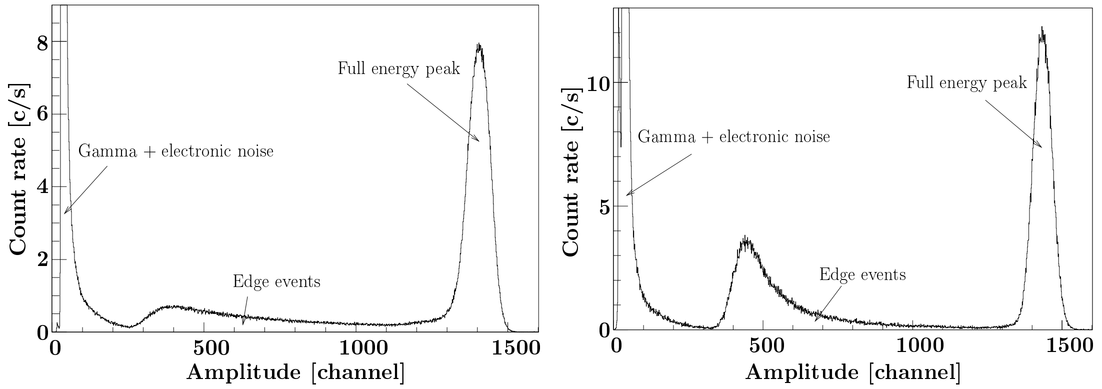

(a) GS10

(b) GS20

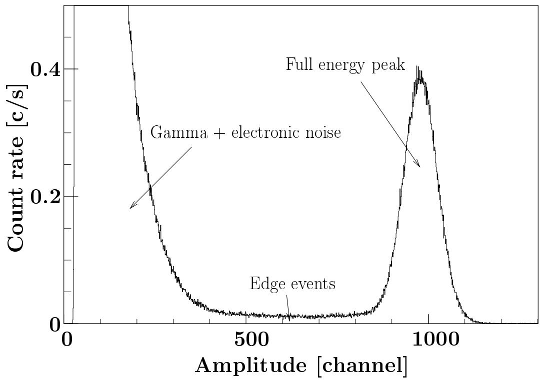

(c) GS3

Figure 10.8: Amplitude distributions for GS3, GS10 and GS20 scintillators. Their thickness is 100 μm. The measurement has performed at the ILL/PF2 EDM beamline. No chopper has been used. The velocity distribution has been slowed down with curved guides.

The amplitude distribution of the GS10 in Fig. 10.8(a) is quite similar to the simulation results. The proportion of edge events is about 30% and the peak resolution is 7%. For the GS20 (Fig. 10.8(b)), the edge events are more important since the UCN mean free path is lower than the GS10. Their amount is about 45% of the total number of UCN detected. This is much less than in the simulation. The reason could be that the ^{6}Li density inside the GS20 is different from that given in the documentation [38]. Concerning the GS3 glass (Fig. 10.8(c)), the number of UCN which are captured is very low. Indeed, the UCN mean free path is much longer than the thickness of the scintillator. If one compares with the GS20, the amount of detected UCN is only 3%. Since no grease has been applied in this case, the position of the UCN peak is lower than for the GS10 and GS20 glasses.

Energy deposition vs glass thickness

Figure 10.9 shows the charge distribution measured for GS10 scintillators with thicknesses of 100 and 500 μm. This test was performed on the ILL/PF2 TEST beamline with the chopper running. Three contributions are observed: the full energy peak (4.78 MeV) which have a resolution of about 10%, the edge events (uncomplete deposition) and the background (gamma plus electronic noise). The background contribution has been obtained using a 5 mm thick polyethylene cap in front of the detectors. It absorbs the UCN and enables to measure the gamma contribution.

The increase of thickness implies that the amount of energy deposited is more important. There is about 25% of edge events in the case of the the 100 μm thick GS10 whereas it is about 15% for the 500 μm thick one. This was checked with the simulations. The proportion of full energy events is more important for the latter since it stops almost all the neutrons. The 100 μm thick GS10 have edge events near the entrance face of the scintillator, but also at the exit face. That means more edge events than the 500 μm thick GS10.

The increase of thickness also implies that more gamma rays interact within the scintillator. For the 100 μm thick GS10, there is about 2% of background in the neutron signal. In contrast, it is about ten times more important for the 500 μm thick GS10. It causes the distortion of the edge event region. It should be noted that the amount of background measured here is very dependent on the experimental conditions. For instance, using a chopper modifies the proportion of UCN to background seen by the detector.

It is more interesting to use a very thin scintillator in order to better dissociate the neutron signal from the gamma contribution.

10.6.1.2 Scintillator stack

Stack scintillator detectors have been developped in order to further improve the UCN/gamma discrimination. Two scintillators with different ^{6}Li doping are associated. One is ^{6}Li-depleted (GS3) and the second one (GS20) is ^{6}Li-enriched. The GS3 glass stands on the GS20 which is directly onto the PMT. Since the GS3 is almost transparent to UCN, most of the UCN are captured within the GS20. The triton and alpha escaping from there can then release their energy inside the GS3 to make a full energy deposition.

Figure 10.10 shows the charge spectrum for the GS3/GS20 stack scintillator. This test has been performed on the TEST beamline without chopper and with a 20-mm diameter polyethylene collimator. No optical grease has been used neither at the

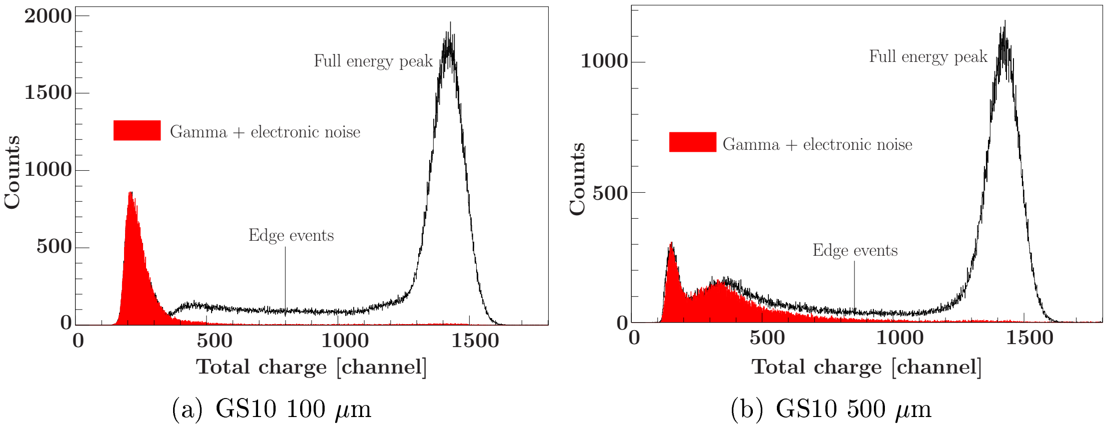

(a) GS10 100 μm

(b) GS10 500 μm

Figure 10.9: Charge distribution measured for a 100 μm thick and 500 μm thick GS10. This was performed at the ILL/PF2 TEST beamline with a chopper.

GS3/GS20 interface nor between the GS20 and the photocathode. Both scintillators are 100 μm thick. The GS3 has been covered with a 200 nm thick aluminium layer acting as a light reflector.

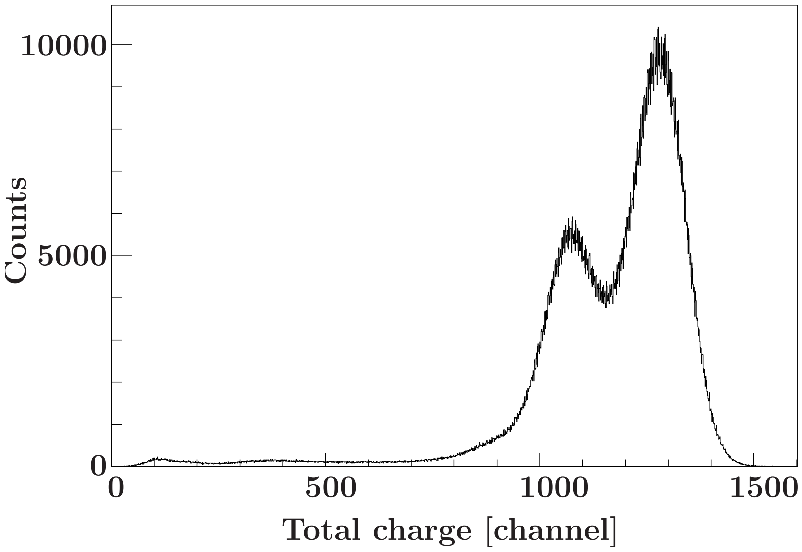

Figure 10.10: Charge spectrum of the GS3/GS20 stack.

The gamma (plus electronic noise) background is located below the channel 250. The fraction of edge events corresponds to about 3% of the total number of UCN detected. It is about 8-10 times lower than for the single 100 μm thick GS10. As a result, the UCN/gamma discrimination is improved with scintillator stacks.

Further tests have been carried out about the light collection of the stack. The goal was to figure out the origin of the two-peaks structure. GS3/GS10 and GS3/GS20 scintillator stacks have been tested. The thickness of each layer was 100 microns. Their diameter was 1 inch. Each stack was placed at the center of the 3 inches PMT. A collimator with an inner diameter of 20 mm was used. Optical grease (silicone) has been applied at the interface between the two scintillators and at the interface with the PMT. In addition, the velocity distribution at the EDM beamline has been slowed down to get a longitudinal velocity between 0 and 10 m/s. The detector signal was amplified and coded in amplitude. Figure 10.11 shows that the use of the optical grease improves the light collection. The mean position of the two peaks increase when grease is applied. Moreover, they are almost completely merged for the GS3/GS20 stack and form a single peak in the case of the GS3/GS10 stack. This means that the existence of the two peaks is due to light collection problems at the PMT interface.

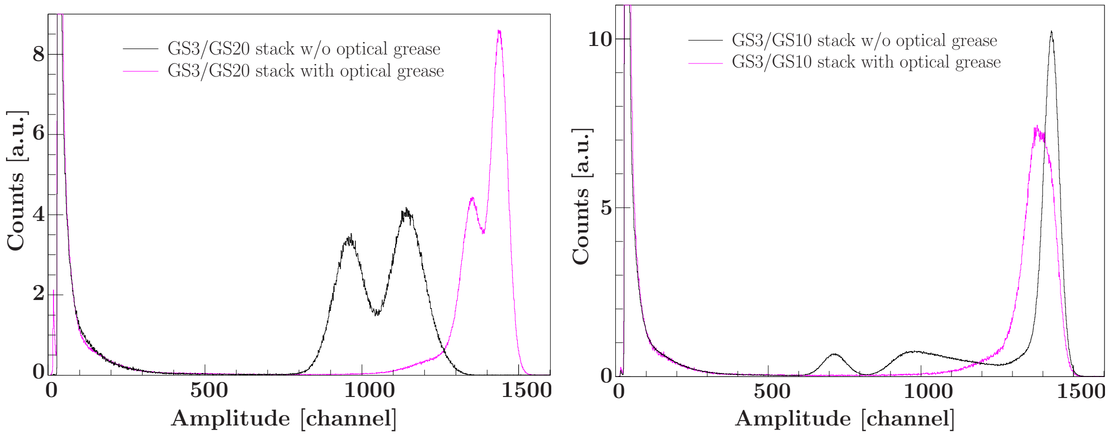

(a) GS3/GS20 stack

(b) GS3/GS10 stack

Figure 10.11: Effect of the optical grease on two scintillator stacks.

10.6.2 Gas detectors

10.6.2.1 The ^{3}He gas detector

Figure 10.12 shows the pulse height distribution measured at the ILL/PF2 EDM beamline with chopper installed. The background contribution within the neutron signal region (edge events region plus full energy peak) is low. It represents only 1% of the total number of neutrons detected. Indeed, the ^{3}He gas detector has a very low sensitivity to gamma background since the density of the detection volume (gas) is low as compared with the glasses. Moreover, low Z materials are used (^{3}He, Ar, CO_2).

10.6.2.2 The cascade-U detector

Figure 10.13 shows a picture of the cascade-U detector (on the right). The entrance foil has been dismounted (on the left). The dark grey square (8 cm x 8 cm) at the center of the aluminium foil corresponds to the boron layer.

Different thicknesses of the ^{10}B layer have been tested on the ILL/PF2 TEST beamline (with chopper installed). Figure 10.14 shows three pulse height spectra which correspond to thicknesses of 50, 200 and 800 nm of boron. As already

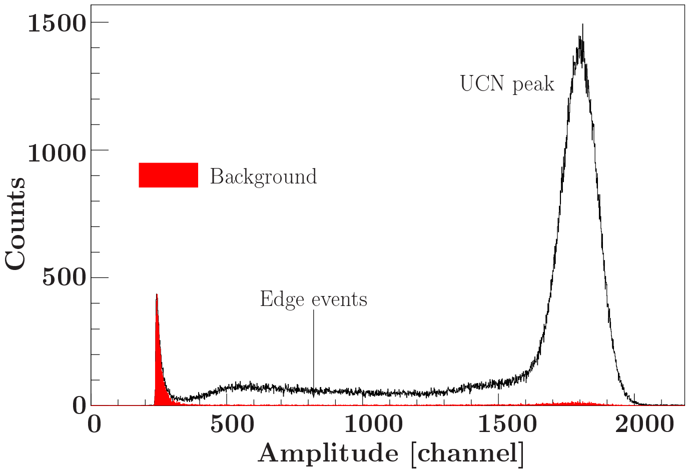

Figure 10.12: Pulse height spectrum of the ^{3}He gas detector.

explained in chapter 9, the two channels coming from the neutron capture are visible when the ^{10}B thickness is 50 nm. When the thickness increases, the alpha and ^{7}Li particles lose more energy in the boron layer. The single peaks cannot be distinguished anymore as shown for a ^{10}B thickness of 800 nm. These measured distributions are similar to those obtained in the simulations.

10.7 Background sensitivity

Three main background contributions can be identified: i) the electronic noise, ii) the gamma background and iii) the thermal neutron background. Whereas the electronic noise and the gamma background are mainly located at low amplitude (or charge), the thermal neutrons are observed at higher amplitude (or charge).

The background sensitivity of gas detectors and scintillators has been measured and compared at ILL/PF2. The detectors were off-line, standing on the ground. They were surrounded with lead and borated paraffin shieldings. Table 10.1 summarizes the background rates measured for four detectors. It has been estimated in the amplitude (charge) region corresponding to both edge and full energy events.

Detectors	GS10 (100 μm)	GS10 (500 μm)	^{3}He	cascade-U
Count rates [10^{-3} c/s]	130±12	720±25	15±1	20±1

Table 10.1: Background rates measurements at ILL/PF2.

Scintillators and gas detectors have the same sensitivity to thermal neutrons. But due to their higher density, the glasses are more sensitive to gamma rays (specially in the edge events region). As a conclusion, the scintillator show a sensitivity about 10 times higher than that of the gas detectors. This is obviously valid for the background conditions existing at ILL/PF2.

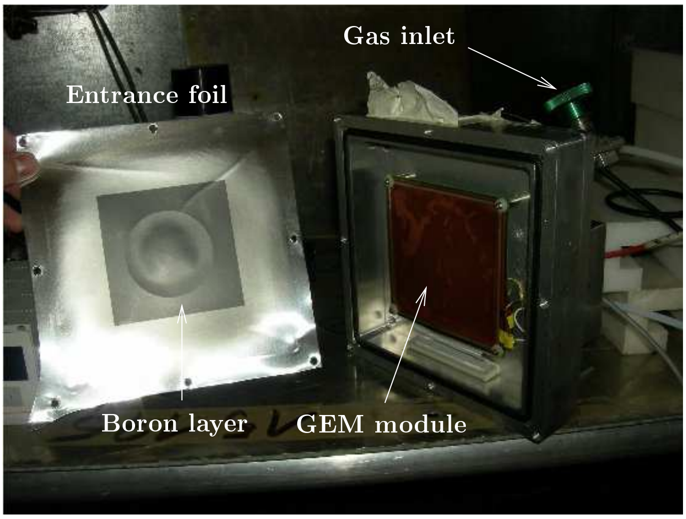

Figure 10.13: Cascade-U detector with the aluminium entrance foil dismounted. The dark grey color is the boron layer of 800 nm thick. The inside of the detector housing shows the GEM module and the readout electronic behind.

10.8 Comparison of detection efficiencies

10.8.1 GSx scintillators

On-line measurement

Table 10.2 summarizes the comparision of the efficiency of detection between GS10 and ^{3}He detectors. The tests have been carried out at the ILL/PF2 EDM beam line. The chopper was used in order to get the TOF distribution. A 5 mm thick polyethylene collimator with an opening diameter of 8 mm was sitting in front of the detectors. The ^{3}He gas detector (Strelkov-Dunia-10 type) was refilled 6 months before these tests.

Detectors	GS10 (100 μm)	GS10 (250 μm)	GS10 (500 μm)	^{3}He
Count rate [c/s]	215 ± 0.4	237.6 ± 0.3	322.8 ± 0.4	261.1 ± 0.5
Relative efficiency to ^{3}He	82.3 ± 0.3%	91.0 ± 0.2%	123.6 ± 0.3%	100.0%

Table 10.2: Count rates and relative efficiencies of GS10 and ^{3}He detectors at ILL/PF2 (EDM line). The errors are statistical.

The 500 μm thick GS10 is about 20% more efficient than the ^{3}He gas detector. The thinner scintillators (100 and 250 μm) are less efficient since the fastest UCN cross the detector without interacting. We have seen that the UCN/gamma discrimination is an advantage of the 100 μm thick GS10 compared with the 500 μm thick. Nevertheless, for the EDM beamline velocity distribution, the 500 μm thick GS10 is the most efficient.

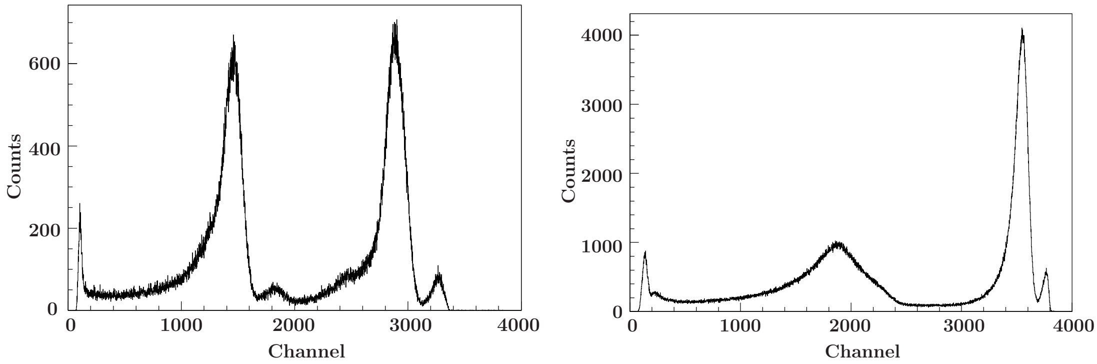

(a) For a boron layer of 50 nm

(b) For a boron layer of 200 nm

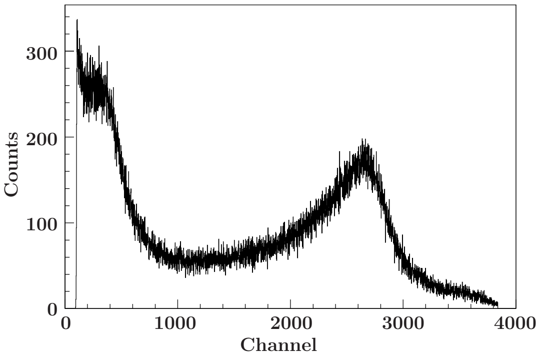

(c) For a boron layer of 800 nm

Figure 10.14: Pulse height spectra of the cascade-U detector for 3 different boron layer thicknesses.

Storage measurement with the EDM spectrometer

The comparison between the detection efficiency of the GSx scintillators and the ^{3}He gas detector have been performed under the EDM spectrometer. A 100 μm thick GS10, a 500 μm thick GS10 and a GS3/GS20 stack (100 μm/100 μm thick) have been tested. For these measurements, the UCN chamber is filled during 40 s. Then storage times τ_s of 5 and 100 s have been used in order to get respectively hard or soft velocity distributions [43]. Table 10.3 shows the efficiencies of the scintillators relative to the ^{3}He gas detector.

Detectors	GS10 (100 μm)	GS10 (500 μm)	GS3/GS20
Rel. efficiency to ^{3}He ($\tau_s = 100$ s)	$88.1 \pm 0.3\%$	$94.5 \pm 0.8\%$	$81.6 \pm 0.6\%$
Rel. efficiency to ^{3}He ($\tau_s = 5$ s)	$91.7 \pm 2.3\%$	$100 \pm 2.9\%$	$84.8 \pm 2.7\%$

Table 10.3: Relative efficiencies between GSx scintillators and the ^{3}He gas detector. Measurements have been done under the EDM spectrometer. The errors take into account the background subtraction.

Compared with the previous measurements carried out directly on the EDM beamline, the 500 μm thick GS10 is still more efficient than the thinner GS10 with a the relative efficiency about 7-8% higher. This is due to the fact that the velocity distribution is globally slower than for the online tests on the EDM beamline. As a consequence, less UCN cross through the 100 μm GS10.

For the soft velocity distribution ($\tau_s = 100$ s), the ^{3}He gas detector is more efficient than the scintillators. For the hard one ($\tau_s = 5$ s), it is still more efficient except in the case of the 500 μm GS10 which has a similar detection efficiency. One notes that the latter has a lower efficiency relatively to the ^{3}He gas detector for the soft velocity spectrum than for the hard one. This may be due to the critical velocity of the detector. It is seen for each scintillator. The ^{3}He detector has the slowest critical velocity (3.2 m/s). In contrast, that of the GS10 scintillator is 4 m/s and for the GS3/GS20, it is about 4.4 m/s.

Nevertheless, it cannot explain completely the fact that the GS3/GS20 stack is still about 15% less efficient than the gas detector for the hard velocity spectrum. Recent tests have been performed on the EDM beamline with a curved guide set-up in order to slow down the longitudinal velocity distribution (below 10 m/s). They have shown that the GS3/GS20 was about 20% less efficient than the single GS20 scintillator. Given that the GS3 and GS20 glasses have the same critical velocity, then UCN may be lost during the transmission through the GS3. This could then explain the difference of efficiency noted for these tests under the EDM spectrometer.

10.8.2 Cascade-U vs GS10 detectors

Two series of tests are shown in table 10.4. They have been performed at the ILL/PF2 TEST beam with the PSI chopper mounted in the beamline. For the first tests, a GS10 500 μm is compared with a cascade-U with a 200 nm thick boron layer. Then, the same GS10 was tested with the same cascade-U with 50 and 800 nm thick boron layers. Results of the simulations are also given.

GS10 (500 μm)	Casc. (200 nm)	GS10 (500 μm)	Casc. (50 nm)	Casc. (800 nm)
121.4±1.6 c/s	97.8±0.2 c/s	115.7±0.2 c/s	62.6±0.1 c/s	82.8±3.3 c/s
100 %	80±1 %	100 %	54.1±0.1 %	69±3 %
Simulated results				
100 %	87 %	100 %	47 %	72 %

Table 10.4: Relative efficiencies between the cascade-U and the GS10 detectors. The errors account for the background subtraction.

The cascade-U with a 200 nm thick boron layer is more efficient than the other configurations with thicknesses of 50 nm and 800 nm. However, in any case, the cascade-U detector is 20% less efficient than the 500 μm GS10. This result is consistent with the measurements performed in [44].

Simulations give results that are close to those of experiments. There are still some discrepancies which may be due to the quality of the aluminium foil or that of the boron deposition. For example, impurities inside the aluminium foil as well as inhomogeneties in the thickness of the boron layer would directly impact on the detector efficiency.

10.9 Conclusions

The experimental tests reported here summarize the results on three types of detectors. The drawback of the cascade-U is its entrance dead layer which decreases significantly its efficiency, as it has been shown in the simulations. The GS10 scintillator has been found to be competitive in terms of efficiency with the ^{3}He detector. The GS3/GS20 scintillator stack is interesting for UCN/gamma discrimination. Nevertheless, it is found to be 15-20% less efficient than the ^{3}He gas detector.

Chapter 11

Principle of the UCN spin analysis

The UCN spin analysis studied in this thesis requires a polarizer, an analyzer, and a spin flipper. The working principle for each of these devices is shown here with more details on the adiabatic spin flipper.

11.1 The UCN polarizer/analyzer

The principle of UCN polarization/analysis uses the interaction of the neutron magnetic moment with a magnetic field (cf. 7.3.3). When a neutron enters into a magnetic region, it feels the potential $-\vec{\mu}\cdot\vec{B}$. The height of this potential depends on the neutron spin state. For a given energy range, only one spin state is able to penetrate the region where the field is applied. Two techniques may be actually employed in order to polarize/analyze UCN : either with a magnetized ferromagnetic foil [45] or with a superconducting solenoid which produces a high magnetic field [62].

In the first case, the polarizer/analyzer is made of a substrate upon which a thin layer of magnetic material is deposited. The substrate must have a low Fermi potential, a low absorption cross section and a low thickness in order to give a transmission as high as possible. Usually, aluminium foils are used as support material. The thin magnetic layer is made of iron.

An external magnetic field magnetized the thin layer of magnetic material. Figure 11.1 shows the principle of UCN polarization through a magnetized sample. The coupling of the spin down (↓) and spin up (↑) neutrons with the magnetization field gives rise to two Fermi potential energies $V_F^{\uparrow}$ and $V_F^{\downarrow}$. Within the energy range given by these two values, spin up neutrons are reflected whereas spin down are transmitted. UCN are polarized.

The external field is chosen so that the magnetization is close to the saturation within the ferromagnetic layer. In pratice, magnetizations close to 2 Teslas may be obtained with thin iron layers [46, 47]. Moreover, iron has a quite high Fermi potential V_F of 210 neV (without any applied external magnetic field) such that it enables to select UCN with high velocities. Table 11.1 gives different energy ranges, calculated from (7.3.14), for different magnetizations inside the iron layer.

With such a polarizing system, one can reach polarizations larger than 90% for a single passage through the foil [51]. In contrast, a superconducting solenoid has about 100% polarizing efficiency [62]. This almost perfect efficiency is valid on a larger velocity range since the magnetic field is stronger. For an intensity of 5 T, the range is between 0 and 7.6 m/s. The UCN transmission is also larger since there is no UCN losses due to the presence of material inside the beamline. For a polarizer/analyzer foil made of 100 μm aluminium with a 200 nm iron layer, the absorption probability is about 5%. Nevertheless, the superconducting magnet needs more development and funding than the use of a ferromagnetic foil. That's why the latter is the most common UCN polarizing/analyzing device.

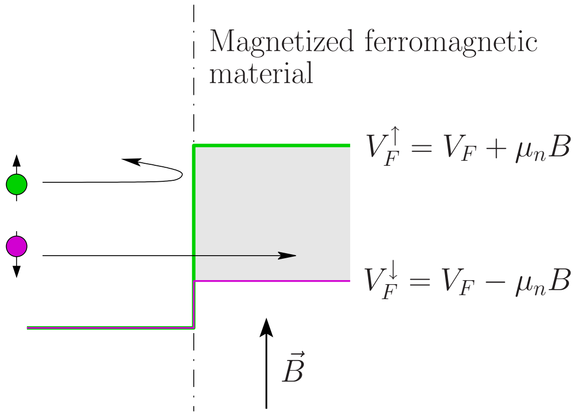

Figure 11.1: UCN polarization/analysis through magnetized foils from the point of view of potential steps. The colored region represents the energy range where the system is efficient since it allows only one spin state to penetrate.

B [T]	$V_F^{\downarrow}$ [neV]	$V_F^{\uparrow}$ [neV]	$v_c^{\downarrow}$ [m/s]	$v_c^{\uparrow}$ [m/s]
1	149.7	270.3	5.4	7.2
1.5	119.6	300.5	4.8	7.6
2	89.4	330.6	4.1	8.0

Table 11.1: The two potential steps of an iron foil according to the value of the magnetization field.

11.2 The adiabatic spin flipper

Descriptions of the classical and quantum approaches of the UCN adiabatic spin flip are given in the following paragraphs. The main advantage of this device is its ability to flip the neutrons spin over a wide velocity range.

11.2.1 Principle of the neutron spin flipper

11.2.1.1 Classical approach

The theoretical treatment relies on the equation of motion of a classical magnetic moment in external magnetic fields [91]. In order to realize the so-called adiabatic spin flip process, one has to use a specific configuration of two orthogonal magnetic fields. The first one is a static field $\overrightarrow{H_0}$ parallel to the vertical z direction. Its intensity decreases along the x axis. The second one, $\overrightarrow{H_{rf}}$, oscillates with a frequency ω_{rf}. It is perpendicular to the static field. The frequency ω_{rf} is chosen such that the resonance occurs at the middle of the gradient region. In the following expressions, we use the neutron intrinsic time $t = x/v$ as independent variable.

It is convenient to carry out the calculations in the neutron frame $\mathfrak{R}_1(\overrightarrow{x_1}, \overrightarrow{y_1}, \overrightarrow{z})$ which rotates at frequency ω_{rf} about the z axis [92] (cf. Fig. 11.2). The oscillating magnetic field is defined in $\mathfrak{R}_1$ as $\overrightarrow{H_{rf}} = H_{rf}(t)\,\overrightarrow{x_1}$. Due to the law of relative motion, an offset field appears in the z direction such that the static field gradient is written as $H_0(t) - \frac{\omega_{rf}}{\gamma_n}$. This is equal to zero at the resonance point (γ_n is the neutron gyromagnetic ratio). Finally, the effective field $\overrightarrow{H_e}$ seen by the neutron in $\mathfrak{R}_1$ is given by:

$$\overrightarrow{H_e}(t) = (H_0(t) - \frac{\omega_{rf}}{\gamma_n})\,\overrightarrow{z} + H_{rf}(t)\,\overrightarrow{x_1}. \tag{11.2.1}$$

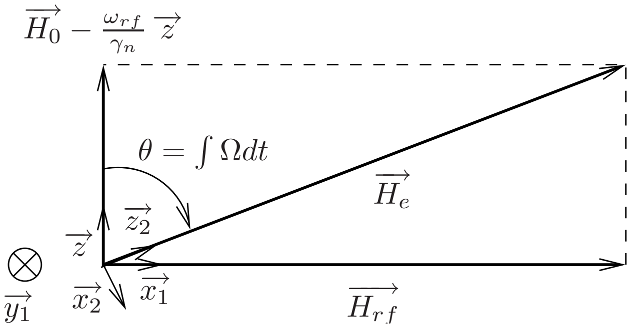

Figure 11.2: Scheme of the magnetic fields in $\mathfrak{R}_1$ frame. Here, $z = z_1$ and $y_1 = y_2$.

The neutron spin $\overrightarrow{S}(t)$ will undergo a torque due to the effective magnetic field. In $\mathfrak{R}_1$, it is:

$$\dot{\overrightarrow{S}}(t) = \gamma_n \overrightarrow{S}(t) \times \overrightarrow{H_e}(t). \tag{11.2.2}$$

This differential system may be expressed in a second coordinate frame $\mathfrak{R}_2(\overrightarrow{x_2}, \overrightarrow{y_1}, \overrightarrow{z_2})$ bound to the effective magnetic field such that: $\overrightarrow{H_e}(t) = H_e(t)\,\overrightarrow{z_2}$ (see Fig. 11.2). With the law of relative motion, one can rewrite (11.2.2) in $\mathfrak{R}_2$ as:

$$\dot{\overrightarrow{S}}(t) = \gamma_n \overrightarrow{S}(t) \times (\overrightarrow{H_e}(t) + \frac{\overrightarrow{\Omega}(t)}{\gamma_n}), \tag{11.2.3}$$

where $\overrightarrow{\Omega}(t) = \Omega(t)\ \overrightarrow{y_1}$ is the rotation velocity of $\overrightarrow{H_e}(t)$ in $\mathfrak{R}_1$. Expanding this equation gives the following set of first order differential equations:

$$\begin{aligned}\dot{S}_x(t) &= \gamma_n S_y(t)\, H_e(t) - S_z(t)\, \Omega(t),\\ \dot{S}_y(t) &= -\gamma_n S_x(t)\, H_e(t),\\ \dot{S}_z(t) &= S_x(t)\, \Omega(t),\end{aligned} \tag{11.2.4}$$

The problem of the spin motion is determined by comparing the neutron Larmor frequency ω_e about $\overrightarrow{H_e}$ with the field rotation rate $\Omega(t)$. According to the adiabatic approximation, the spin will follow the effective field if $|\Omega(t)| \ll |\omega_e|$ or $\eta(t) \gg 1$ with η the so-called adiabatic parameter [93]:

$$\eta(t) = \left|\frac{\omega_e}{\Omega(t)}\right| = \left|\frac{\gamma_n\, H_e(t)}{\Omega(t)}\right|. \tag{11.2.5}$$

Figure 11.3 shows spin motion when the adiabatic condition is satisfied. $\Omega(t)$ is obtained by deriving the following equations in $\mathfrak{R}_1$:

$$\begin{aligned}H_{rf}(t) &= H_e(t) \sin\theta(t),\\ H_e(t) &= \sqrt{H_{rf}(t)^2 + \left(H_0(t) - \frac{\omega_{rf}}{\gamma_n}\right)^2}.\end{aligned}$$

The resulting expression for the adiabatic parameter (11.2.5) is:

$$\eta(t) = \frac{\gamma_n\, H_e(t)^3}{\dot{H}_{rf}(t)\left(H_0(t) - \frac{\omega_{rf}}{\gamma_n}\right) - \dot{H}_0(t)\, H_{rf}(t)}. \tag{11.2.6}$$

These equations may be applied to a specific field configuration. A realistic expression of η may be derived from the sine-cosine modulation model. For the two magnetic fields H_0 and H_{rf}, one writes [94]:

$$H_{rf}(x) = A\ \sin(\pi \frac{x}{L}), \tag{11.2.7}$$

$$H_0(x) = B + A\ \cos(\pi \frac{x}{L}), \tag{11.2.8}$$

where L is the spin flipper length, $x \in [0, L]$ and B is the value of the static field at the center x_0 of the spin flipper. $A = H_0(0) - H_0(x_0)$ is the amplitude of the modulation. Then by inserting (11.2.7) and (11.2.8) in (11.2.5), one finds:

$$\eta = \frac{\gamma_n\, L\, A}{\pi\, v}. \tag{11.2.9}$$

Since the resonance at the middle of the spin flipper has been considered, then $\gamma_n\, B = \omega_{rf}$.The sine-cosine field model is in good agreement with the typical experimental set-up of an adiabatic spin flipper [50]. From equation (11.2.9), one deduces that for

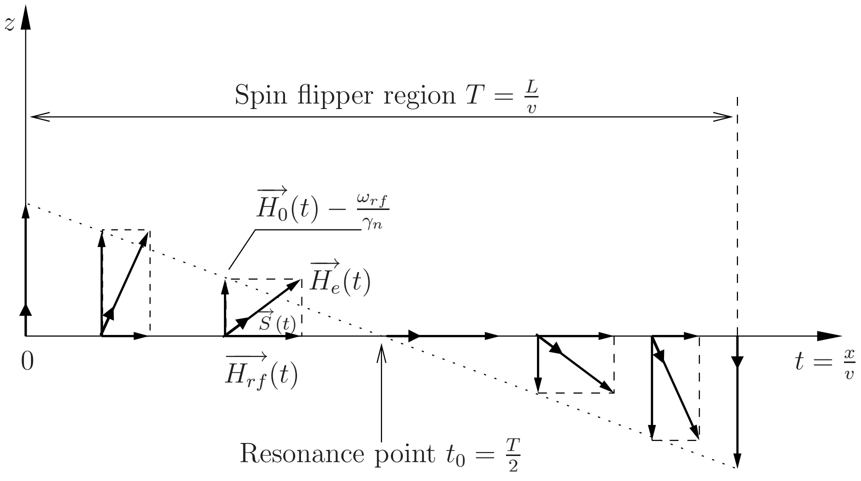

Figure 11.3: Evolution of the spin with the neutron current time. The vectors are presented in $\mathfrak{R}_1$ frame. According to the adiabatic condition, the spin follows the effective field H_e and after a resonance which occurs in the middle of the flipper, it finally ends antiparallel to the initially H_0 direction.

given L and A, the adiabatic condition $\eta \gg 1$ is verified for UCN velocities smaller than a maximum value v_l. With $v_l = 20$ m/s (i.e about the highest neutron velocities available at ILL/PF2), and a spin flipper length of $L = 20$ cm, then all neutrons will be flipped if the modulating amplitude of the magnetic fields is larger than 20 mG, which is pratically easy to perform. Moreover, simulations based on (11.2.4) have shown that for $\eta \geq 6$, the spin is still flipped with an efficiency of 90%.

11.2.1.2 Quantum mechanical approach

The quantum mechanical approach enables to determine an expression for the spin flip probability. It can be calculated by the use of rotation operators inside the Schrödinger equation [48].

We keep the same coordinate system with a neutron going along the axis x. The effective field H_e is along z at $t = 0$. At time $t \neq 0$, $H_e(t)$ makes an angle $\theta(t)$ with the axis z. H_e and θ are the only variables that we need to do our calculations. The time evolution of the spin is given by the Schrödinger equation:

$$i\hbar \frac{d}{dt}|\psi(t)\rangle = \hat{H}|\psi(t)\rangle, \tag{11.2.10}$$

with the Hamiltonian operator $\hat{H} = \hat{\vec{\mu}}_n \cdot \overrightarrow{H_e}$, where $\hat{\vec{\mu}}_n$ is the neutron magnetic moment operator which can be written by means of the Pauli matrices $\hat{\vec{\sigma}} = (\hat{\sigma}_x, \hat{\sigma}_y, \hat{\sigma}_z)$ with their expression:

$$\hat{\sigma}_x = \begin{pmatrix} 0 & 1 \\ 1 & 0 \end{pmatrix}, \qquad \hat{\sigma}_y = \begin{pmatrix} 0 & -i \\ i & 0 \end{pmatrix}, \qquad \hat{\sigma}_z = \begin{pmatrix} 1 & 0 \\ 0 & -1 \end{pmatrix}. \tag{11.2.11}$$

The wave function $|\psi(t)\rangle$ is the spinor such that: $|\psi(t)\rangle = \psi_+(t)\begin{pmatrix} 1 \\ 0 \end{pmatrix} + \psi_-(t)\begin{pmatrix} 0 \\ 1 \end{pmatrix}$. By expanding the Hamiltonian, one can find:

$$\begin{aligned}\hat{H} &= \gamma\,\hat{\vec{S}}\cdot\overrightarrow{H_e},\\ &= \gamma\,\frac{\hbar}{2}\,\hat{\vec{\sigma}}\cdot\overrightarrow{H_e},\\ &= \gamma\,H_e(t)\,\frac{\hbar}{2}\begin{pmatrix}\cos\theta(t) & \sin\theta(t)\\ \sin\theta(t) & -\cos\theta(t)\end{pmatrix}.\end{aligned} \tag{11.2.12}$$

Here we have used the polar expression of the field $\overrightarrow{H_e}(t) = H_e(t)\left(\sin\theta(t), 0, \cos\theta(t)\right)$. By inserting (11.2.12) in the Schrödinger equation (11.2.10), we deduce:

$$\begin{pmatrix}\dot{\psi}_+\\ \dot{\psi}_-\end{pmatrix} = -\frac{i}{2}\gamma\,H_e(t)\begin{pmatrix}\cos\theta(t) & \sin\theta(t)\\ \sin\theta(t) & -\cos\theta(t)\end{pmatrix}\begin{pmatrix}\psi_+\\ \psi_-\end{pmatrix}, \tag{11.2.13}$$

which is of the form :

$$\frac{d}{dt}|\psi(t)\rangle = -\frac{i}{2}\,\omega_e\,\hat{M}\,|\psi(t)\rangle, \tag{11.2.14}$$

where $\omega_e = \gamma\,H_e$ is the classical precession frequency around H_e. Then as we have done for the classical case, we should continue our calculations in the frame connected with the magnetic field vector $\overrightarrow{H_e}$. Mathematically, we use the operator $\hat{R}_y(\theta)$ which represents the rotation of a state vector by an angle θ about the y axis. In the case of a spin $\frac{1}{2}$ particle, the rotation operator defined by an angle ϕ around the axis ξ is $\hat{R}_\xi(\phi) = e^{-\frac{i}{2}\phi\,\hat{\sigma}_\xi}$ [95], which leads to the expression :

$$\hat{R}_\xi(\phi) = \cos\frac{\phi}{2} - i\hat{\sigma}_\xi\sin\frac{\phi}{2}. \tag{11.2.15}$$

Applying this result, we find for $\hat{R}_y(\theta)$:

$$\hat{R}_y(\theta) = \begin{pmatrix}\cos\frac{\theta}{2} & -\sin\frac{\theta}{2}\\ \sin\frac{\theta}{2} & \cos\frac{\theta}{2}\end{pmatrix}. \tag{11.2.16}$$

When we expand the equation (11.2.14), the transformation $|\psi(t)\rangle = \hat{R}_y\,|\psi'(t)\rangle$ results in:

$$\frac{d}{dt}|\psi'(t)\rangle = -\frac{i}{2}\omega_e\,\hat{R}_y^{-1}\hat{M}\hat{R}_y\,|\psi'(t)\rangle - \hat{R}_y^{-1}\dot{\hat{R}}_y\,|\psi'(t)\rangle. \tag{11.2.17}$$

At this point of the caculation, the state vector of the wave function is expressed in the coordinate system connected with the magnetic field H_e. Let's develop using equations (11.2.16) and (11.2.14). We find:

$$\begin{pmatrix}\dot{\psi}'_+\\ \dot{\psi}'_-\end{pmatrix} = -\frac{i}{2}\,\omega_e\begin{pmatrix}1 & 0\\ 0 & -1\end{pmatrix}\begin{pmatrix}\psi'_+\\ \psi'_-\end{pmatrix} - \frac{1}{2}\,\dot{\theta}\begin{pmatrix}0 & -1\\ 1 & 0\end{pmatrix}\begin{pmatrix}\psi'_+\\ \psi'_-\end{pmatrix} \tag{11.2.18}$$

Note here the indirect appearance of the adiabatic parameter $\eta = \left|\frac{\omega_e}{\dot{\theta}}\right|$ that we have seen during the treatment of the classical case (cf. equation (11.2.5)).

Let us go now a step further by applying another transformation. We are currently along the field H_e and the next stage is to follow the spin in this frame. We do this the same way than before thanks to the rotation operator $\hat{R}_{H_e}(\lambda)$ which makes a state vector turning by an angle λ about the field axis. The expression (11.2.15) provides the following result:

$$\hat{R}_{H_e}(\lambda) = \begin{pmatrix} e^{-\frac{i}{2}\lambda} & 0 \\ 0 & e^{\frac{i}{2}\lambda} \end{pmatrix}, \tag{11.2.19}$$

where λ represents the total angle of precession of the spin under the field action : $\lambda(t) = \int_0^t \omega_e(\tau) d\tau$.
The transformation $|\psi'(t)\rangle = \hat{R}_{H_e} |\psi''(t)\rangle$ consequently leads to:

$$\frac{d}{dt}|\psi''(t)\rangle = \hat{R}_{H_e}^{-1} \left[\frac{d}{dt}|\psi'(t)\rangle\right] - \hat{R}_{H_e}^{-1} \dot{\hat{R}}_{H_e} |\psi''(t)\rangle, \tag{11.2.20}$$

with $\frac{d}{dt}|\psi'(t)\rangle$ to be taken as (11.2.17). If one expands this expression in the matrix form, then :

$$\begin{pmatrix} \dot{\psi}''_+ \\ \dot{\psi}''_- \end{pmatrix} = \frac{\dot{\theta}}{2} \begin{pmatrix} 0 & e^{i\lambda} \\ -e^{-i\lambda} & 0 \end{pmatrix} \begin{pmatrix} \psi''_+ \\ \psi''_- \end{pmatrix} \tag{11.2.21}$$

Two coupled equations of the first order are found. They can be solved when choosing θ as new independant variable. Thus:

$$\begin{aligned} \frac{d\psi''_+}{d\theta} &= \frac{1}{2} e^{i\lambda} \psi''_-, \\ \frac{d\psi''_-}{d\theta} &= -\frac{1}{2} e^{-i\lambda} \psi''_+, \end{aligned} \tag{11.2.22}$$

with λ function of θ via the adiabatic parameter:

$$\begin{aligned} \lambda &= \int_0^t \omega_e(\tau) d\tau, \\ &= \int_0^\theta \frac{\omega_e}{\dot{\theta}} d\theta, \\ &= \int_0^\theta \eta(\theta) d\theta. \end{aligned} \tag{11.2.23}$$

The final system to solve finally comes after decoupling:

$$\begin{aligned} \frac{d^2\psi''_+}{d\theta^2} - i\eta \frac{d\psi''_+}{d\theta} + \frac{1}{4}\psi''_+ &= 0, \\ \frac{d^2\psi''_-}{d\theta^2} + i\eta \frac{d\psi''_-}{d\theta} + \frac{1}{4}\psi''_- &= 0. \end{aligned} \tag{11.2.24}$$

We have seen that for the sine-cosine magnetic field model, η could be simplified to a constant. The two above equation are then simple second order differential equations with constant coefficients. Both solutions have the form:

$$\psi''_\pm = e^{\pm\frac{i\eta\theta}{2}} \Big(C_\pm \cos(\frac{\theta}{2}\sqrt{1+\eta^2}) + iD_\pm \sin(\frac{\theta}{2}\sqrt{1+\eta^2}) \Big). \tag{11.2.25}$$

We may choose the initial boundary conditions at $t = 0$ as: i) $\theta = 0$ and ii) spin up state, i.e. $\psi_+ = 1$ and $\psi_- = 0$. To find the initial $\psi''_\pm$, we use our rotation operators defined above such that $|\psi''\rangle = \hat{R}^{-1}_{H_e}\hat{R}^{-1}_y\,|\psi\rangle$. It follows that $\psi''_+(\theta = 0) = 1$ and $\psi''_-(\theta = 0) = 0$. Applying this to the raw solutions (11.2.25), we find $C_+ = 1$ and $C_- = 0$. $D_\pm$ are calculated from the coupled system (11.2.22) which gives $D_+ = -\frac{\eta}{\sqrt{1+\eta^2}}$ and $D_- = -\frac{1}{i\sqrt{1+\eta^2}}$. The complete solutions for the spin up initial state are finally:

$$\psi''_+ = e^{\frac{i\eta\theta}{2}}\Big(\cos(\frac{\theta}{2}\sqrt{1+\eta^2}) - \frac{i\eta}{\sqrt{1+\eta^2}}\sin(\frac{\theta}{2}\sqrt{1+\eta^2})\Big),$$
$$\psi''_- = -\frac{e^{-\frac{i\eta\theta}{2}}}{\sqrt{1+\eta^2}}\sin(\frac{\theta}{2}\sqrt{1+\eta^2}). \tag{11.2.26}$$

Now we can determine the spin flip probability of this spin flipper. It should be emphasized that the term “spinflip” is in fact improperly used here. Indeed, it is not a quantum spin flip from on state to another because the principle of the adiabatic spin flipper is to maintain the spin along the effective field direction during its rotation. There is consequently no spin flip at all in that case!

One can find back the $|\psi\rangle$ with the use of the rotation operators and deduce that when the field has turned over π radians:

$$|\psi_+|^2 = \frac{1}{1+\eta^2}\sin^2(\frac{\pi}{2}\sqrt{1+\eta^2}),$$
$$|\psi_-|^2 = 1 - |\psi_+|^2, \tag{11.2.27}$$

where the first equation represents a spin flip in the quantum sense since the effective field is flipped over π radians. Inversely for the second expression, where the spin is kept along the quantization axis given by the field. Therefore this last equation really stands for the spin flip probability p of the adiabatic spin flipper [50]:

$$p = 1 - \frac{\sin^2(\frac{\pi}{2}\sqrt{1+\eta^2})}{1+\eta^2} \tag{11.2.28}$$

Figure 11.4 shows (11.2.28) as a function of the spin flipper length. One can see that the spin flipper size does not limit its efficiency. This works also for high UCN velocities. Consequently, it is possible to use small device to spin flip neutrons in a wide range of velocities.

11.2.2 Summary

The adiabatic passage of the neutron spin through a resonant coil requires a specific configuration of the magnetic field. The main parameter to achieve a complete flip of the neutron is the adiabatic parameter η which imposes a condition on the magnitude of the gradient field, the value of velocity and the spin flipper length. For ultracold neutrons, it verifies the adiabatic condition ($\eta \gg 1$) for a wide range of velocities and spin flipper length.

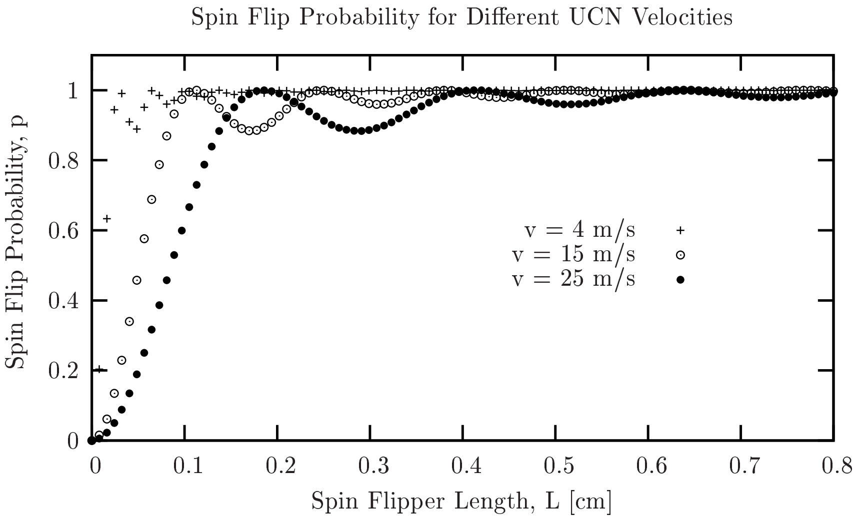

Figure 11.4: Spin flip probability as a function of the spin flipper length. These curves are calculated for $A = 4$ G.

Chapter 12

Monte Carlo simulations of the experimental procedures for spin analysis

In this chapter, Monte-Carlo simulations performed with the Geant4UCN package [96] are described. Both simultaneous and sequential spin analysis methods have been simulated. The goal is to decrease the counting period of both spin components at the end of a Ramsey cycle and to reduce the depolarization effects. That means that during the neutron EDM measurement, i.e. during a series of Ramsey cycles, the statistics will be accumulated faster. Furthermore, the figure of merit (Ramsey pattern) is expected to be larger.

12.1 Introduction

The mounting of the RAL-Sussex-ILL apparatus at PSI will require several modifications. Figure 12.1 shows a draft scheme of the apparatus at PSI where the spin polarization and analysis will be dissociated. Indeed, in the ILL nEDM setup, the polarizer and the analyzer are the *same* device. The incoming neutrons are first polarized by passing through a magnetized foil and then are stored during hundreds of seconds. They are finally released by the end of the storage period and are analyzed by the same foil (see Fig. 6.3). At PSI, a superconducting polarizer will be used in order to improve the polarizing efficiency of UCN. The spin analysis will be done below the switch guide tube system (see Fig. 12.1).

Simulations have shown that by improving the chamber material (from quartz to DPS) and reducing the height between the chamber and the input guide (about 1.2 m instead of 1.8 m) should increase by about 50% the number of stored neutrons in the chamber [97]. Since the UCN kinetic energy is modified by gravity, it impacts directly on the location of the spin analysis system which efficiency depends on UCN velocity (see chapter 11).

The following simulations take into account these modifications with the aim to compare two spin analysis procedures: sequential and simultaneous.

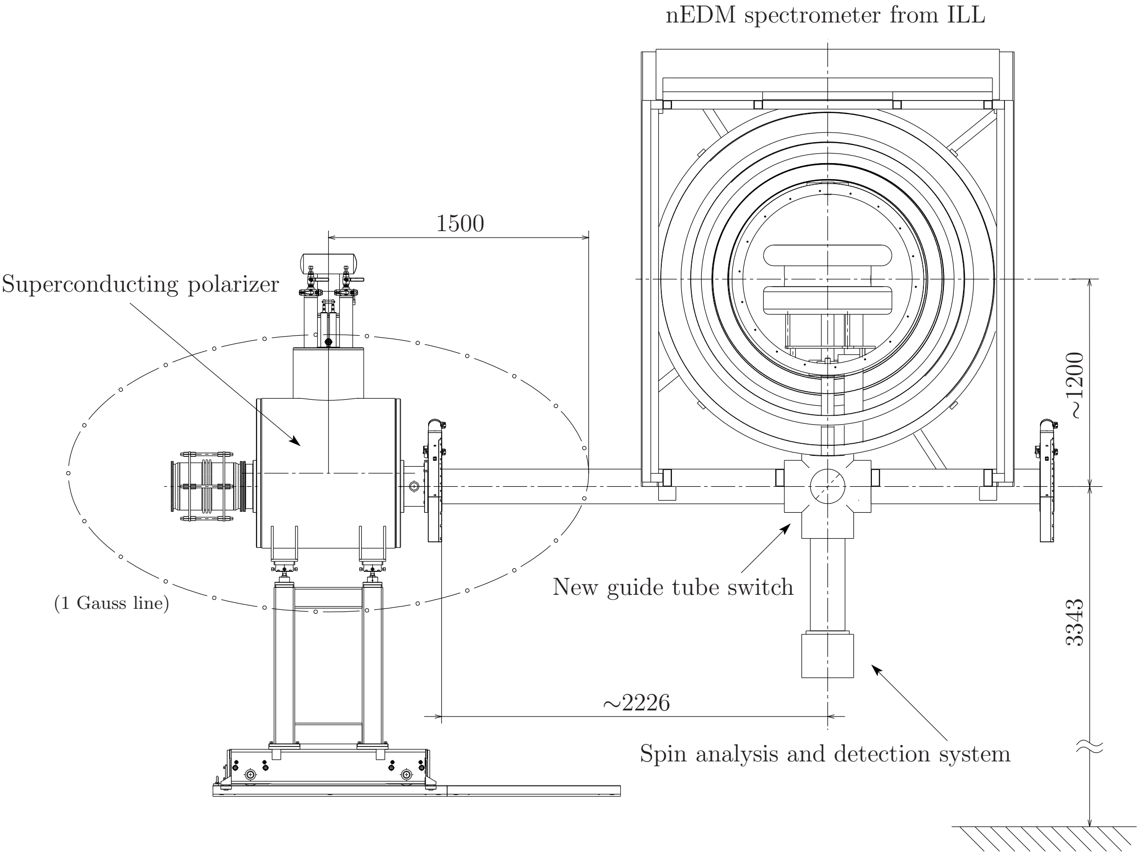

Figure 12.1: Adaptation of the Sussex-RAL-ILL apparatus at PSI. UCN will be polarized by the superconducting magnet and will fill the storage chamber. After some time, they are counted down in the detector. Note that the throughgoing port of the switch enables to bypass the nEDM apparatus for test experiments.

12.2 Materials and coatings in the simulations

Table 12.1 summarizes some of the properties of the materials used in the simulations. When the loss factor η and the spin flip probability per collision β of a material (see chapter 7) are unknown, we use some rough values ($\eta = 1 \cdot 10^{-4}$ and $\beta = 1 \cdot 10^{-5}$) which are in the typical ranges observed in experiments. Similarly, the absorption and total scattering cross sections are not always known from experiments. In this case, the values inserted in the simulations are the weighted average of the cross sections obtained for the constituting atoms. It should be noted that even in the case of a well-known material, the parameters given below always depend on the conditions (i.e. temperature, cleaning products, environment) in which it has been produced.

DLC (Diamond-Like-Carbon) and DPS (Deutrated PolyStyrene) are used inside the storage chamber since they have relatively high Fermi potentials and high resistivities to electric field. They are also compatible with a mercury comagnetometer [43]. NiMo coats the vertical guide tube and the inner part of the analyzing device. The analyzer is made of a 200 nm iron layer deposited on a 100 μm aluminum

	V_F [neV]	v_c [m/s]	σ_a [b]	σ_s [b]	η [$\cdot 10^{-4}$]	β [$\cdot 10^{-5}$]
DLC	221.1	6.5	0.0049	12.6	5	0.3
DPS	162	5.6	0.0047	7.15	4	0.3
NiMo (85/15)	220	6.5	4.49	18.5	1	1
Iron	210	6.3	2.56	11.62	0.85	1
Aluminium	54	3.2	0.231	1.503	0.225	1
GS10	84.8	4	14.7	3.1	1	1

Table 12.1: Lists of materials used in the Geant4 simulations. V_F stands for the Fermi potential and v_c for the corresponding critical velocity. σ_a is the absorption cross section and σ_s is the total scattering cross section. The two last parameters are the loss factor η and the spin flip probability β per collision.

foil. Finally, a 200 μm thick GS10 stands for the detector material.

The simulations also take into account the UCN probability of diffuse reflection per bounce. This parameter not only randomizes the UCN trajectories but also increases a bit the loss factor μ [53]. This last point is not implemented in the Geant4 simulation. In the storage chamber, we take 10% for DLC and DPS and 1% for the other materials [97].

12.3 The spin in the simulations

Simulating the classical spin motion generally leads to large calculation times (1). The problem is simplified in the simulation: a simple flag holds the neutron state information (up or down).

As a result, the spin flip mechanism only consists in reversing the spin flag. This may happen during a wall collision (see the β parameter in table 12.1), or when the adiabatic spin flipper is active.

12.4 Inputs of the simulations

The MC simulation of a given experiment should normally begin at the source exit which velocity distributions are known. However, such a simulation would be very time consuming for experiments with large or complicated geometries. The idea is then to make a MC simulation once and for all in order to obtain the UCN distributions (position and velocity) inside the nEDM chamber after 100 seconds of storage.

12.4.1 Initial UCN distributions at the ILL source exit

The initial velocity spectra used to simulate the filling of the nEDM chamber are those of chapter 9. The height to the UCN chamber is 1.5 m. The radial components

---

(1) It should also be noted that such work is profitable only if one gets a precise magnetic field map of a system — that is currently not the case for the nEDM spectrometer.

are taken as gaussian and are simply limited by the critical velocity of the stainless steel guide tube that is used at ILL. The longitudinal component is based on our measurements at ILL and its shape is given by two semi-gaussians (cf. Fig. 9.1). The distribution of the velocity modulus is shown on Fig. 12.2 (in black).

The positions of the particles are generated on a 67-mm diameter disc. No spin implementation is needed for this simulation.

12.4.2 Distributions after 100 seconds of storage

Thanks to the previous simulation, the UCN conditions after 100 seconds of storage in the precession chamber are available. It is now possible to shoot the UCN directly inside the storage volume and to simulate the sequential counting with respect to the spin state.

Either spin down or spin up populations of neutrons are initially shot. There is no calculation with a mixed population. Figure 12.2 shows the velocity modulus distribution (in green). The three velocity components (v_{x_0}, v_{y_0}, v_{z_0}) are considered as gaussian. Particles are generated uniformly over the whole storage volume — no gravity gradient is taken into account.

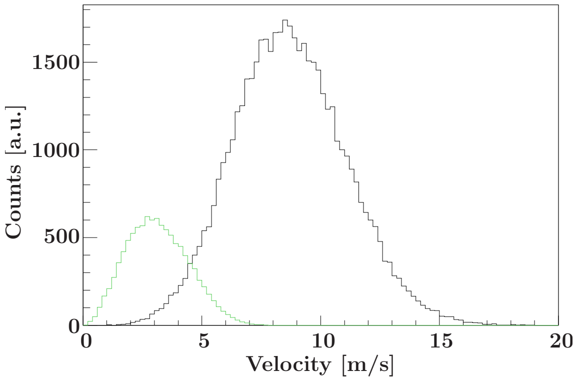

Figure 12.2: Initial velocity distributions used in the simulations. The black curve represents the velocity modulus spectrum at the source exit. The green one is the velocity distribution obtained after 100 s storage in the nEDM chamber. The insulating cylinder of this chamber is coated with DPS and the two electrodes with DLC. The diameter of the trap is 470 mm with a height of 120 mm.

12.5 Simulation of the sequential spin analysis system

12.5.1 Modelization of the spin flipper and analyzer

The spin flipper is a region of space — typically a cylinder — where the neutron spin may be flipped if the device is active. Note that the spin flip only occurs if the neutron crosses the total length of the spin flipper. Thus, if a neutron enters in the active region and, after a diffuse reflection, goes back without having crossed completely the spin flipper, then no spin flip will occur. This realizes a perfect spin flipper, i.e. with a unitary spin flip probability (see chapter 11).

The analyzer is formed by the stacking of two thin cylinders: one made of iron (200 nm thick) and the second in aluminium (100 μm thick). The iron layer is magnetized and an internal magnetic field of 1.5 Tesla is taken in the simulations. Indeed, we have observed in our multiple magnetization tests that the saturation magnetization at 2 Tesla was never completely obtained with our magnetization systems. Table 11.1 gives the values of the Fermi potentials for such a magnetization value.

12.5.2 The timing sequence

The geometry simulated in Geant4 is shown in Fig. 12.3. The UCN are generated inside the chamber at $t = 0$ s and have the possibility to fall down into the vertical guide tube. Then they are counted according to the experimental timing sequence defined by the RAL-Sussex-ILL collaboration [43]. It lasts 40 seconds with three time intervals:

- $T_1 : t \in [0, 8\,\mathrm{s}]$: the spin flipper is active and only UCN with a spin up state in the chamber can cross the foil. Then they are detected$^{(2)}$;

- $T_2 : t \in [8, 28\,\mathrm{s}]$: the spin flipper is off. UCN which have been trapped above the foil have now the good polarization (i.e. spin down) and can be counted;

- $T_3 : t \in [28, 40\,\mathrm{s}]$: the spin flipper is on. UCN with a spin up state can be again detected.

Such a timing sequence has been originally chosen to get approximately the same visibility coefficient α for either spin up or spin down populations in the nEDM chamber (see chapter 6). In the following, the numbers of neutrons which are counted when the spin flipper is tuned on (off) are denoted N_{on} (N_{off}).

Two Geant4 simulations have been performed with the same counting sequences, but with different initial populations of polarized neutrons, either 100% spin up or 100% spin down.

12.5.3 UCN losses in the geometry

Determining the losses during the counting procedure directly impacts on the statistics of the measurement. Below we describe the losses as a function of the timing sequence and the location in the geometry.

---

(2) Here the spin state is defined with respect to the magnetization direction within the analyzing foil.

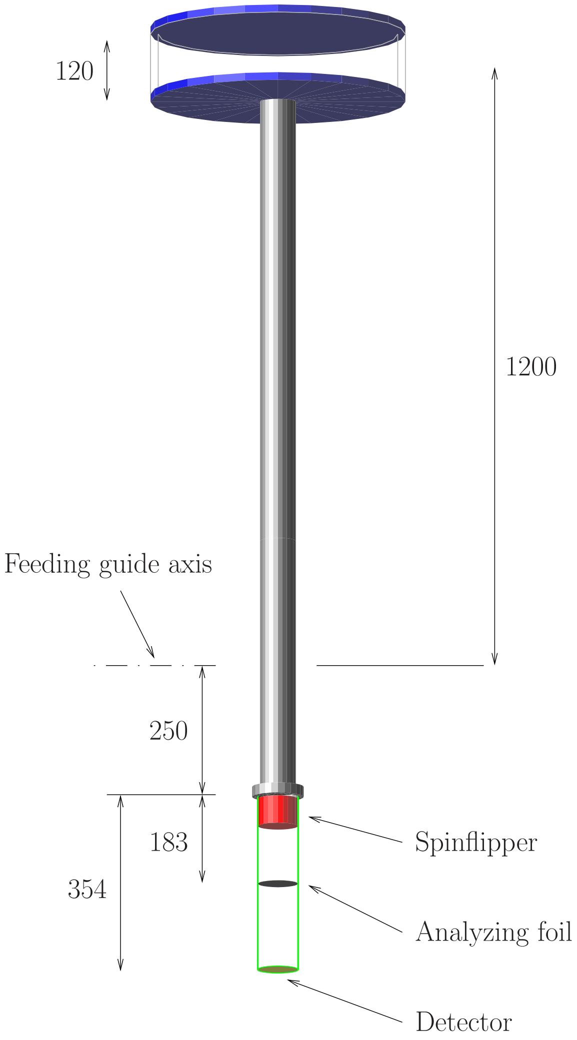

Figure 12.3: Geant4 geometry of the sequential analysis system. Dimensions are in mm.

100% spin down in the nEDM chamber

The losses have been registered as a function of the three time intervals T_1, T_2 and T_3. The percentages of losses, calculated with respect to the initial number of UCN ($N_0 = 25000$), are given in table 12.2.

As one might expect during T_1, the reflection losses are important since the particles are bouncing everywhere in the volume above the foil, and especially in the storage chamber (6.7%). During T_2, particles can cross the analyzer. The reflection losses are still present within the chamber and the vertical guide tube, but there are also absorption losses inside the analyzing foil mainly due to the aluminium substrate. During T_3, the number of remaining neutrons is very low and so it is for the losses. They represent less than 1% of N_0.

Finally, 22% of the initial number of particles are lost in the geometry. The majority of these losses are located within the nEDM chamber (over 40 s) and are partly due to the time when neutrons are waiting for being analyzed.

	$t \in T_1$	$t \in T_2$	$t \in T_3$	Whole sequence (40 s)
Storage chamber	6.7%	4.1%	0.4%	11.2%
Analyzing foil	0.06%	4.65%	0.09%	4.8%
Vertical guide	3.6%	2.0%	0.4%	6.0%
Whole geometry	10.36%	10.75%	0.89%	22.0%

Table 12.2: Percentages of losses obtained with an initial population of spin down UCN.

100% spin up in the nEDM chamber

Table 12.3 shows the percentages of losses calculated with respect to the initial number of neutrons ($N_0 = 25000$).

	$t \in T_1$	$t \in T_2$	$t \in T_3$	Whole sequence (40 s)
Storage chamber	5.2%	3.7%	1.0%	9.9%
Analyzing foil	3.3%	0.1%	1.6%	5.0%
Vertical guide	0.8%	3.1%	0.7%	4.6%
Whole geometry	9.3%	6.9%	3.3%	19.5%

Table 12.3: Percentages of losses obtained with an initial population of spin up UCN.

The same features than with the spin down UCN are observed. Again, because of the waiting period T_2, the UCN are continuously lost in the chamber (3.7%). Since neutrons are escaping from it in an exponential way, these losses are less important than in the spin down case for which T_1 and T_3 are the waiting periods. Indeed, here one loses about 7% during T_2 whereas these losses are about 11% for the previous simulation (cf. first and third columns in the table 12.2).

Comparisons and conclusions

The losses are different between both previous simulations because the two spin components are not analyzed during the same time intervals. Moreover, the fact that neutrons have to wait some time before being analyzed is also critical for the losses.

To decrease them, one could think of: i) choosing material coatings with higher Fermi potential, ii) decreasing the measurement time. As mentioned earlier (see section 12.2), we have chosen in these calculations new material coatings with high Fermi potential (see table 12.1). One may try to decrease the analyzer thickness. But in practice, this would make difficult the manipulation of the foil and it would certainly slow down the vacuum procedure in order not to damage it. Nevertheless, in stable operation (i.e. during an EDM measurement), a foil with a thinner substrate should decrease the losses and at the same time increase the number of counted UCN. For example, dividing the aluminium thickness by two would lead to have approximately 1.6 times less absorption.

12.5.4 Spin analysis efficiency

100% spin down in the nEDM chamber

Figure 12.4 shows the number of counts as a function of the time. The percentages with respect to the total number of detected neutrons are also given in table 12.4.

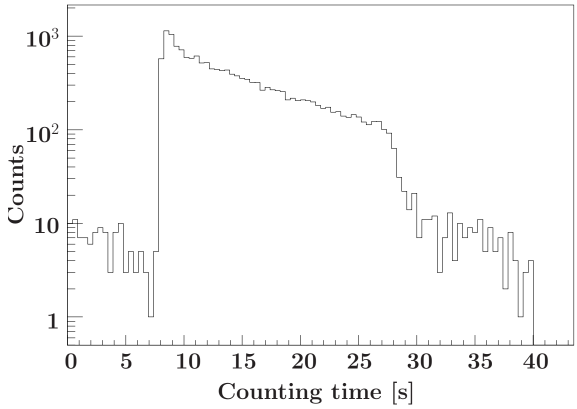

Figure 12.4: Counting time spectrum obtained with an initial population of 100% spin down UCN.

	$t \in T_1$	$t \in T_2$	$t \in T_3$	Whole sequence (40 s)
Spin down UCN	0.1%	97.5%	1.8%	99.4%
Spin up UCN	0.6%	0.0%	0.0%	0.6%
Total number	0.7%	97.5%	1.8%	100.0%

Table 12.4: Percentages of counts obtained with an initial population of spin down UCN.

During T_1, the spin flipper is on so that almost all the neutrons come with their spin up at the analyzing foil surface. Since they interact with $V_F^{\uparrow}$, they are reflected and only 0.7% successfully cross the foil. One can see in table 12.4 that 0.1% of spin down neutrons are detected: this is due to the depolarization effect. In contrast, the 0.6% of spin up results from the gravitational boost which gets their normal velocity to be above $v_c^{\uparrow} = 7.6$ m/s(3).

During T_2, the spin flipper is off and spin down neutrons can go through the analyzing foil. 97.5% of the total number of detected neutrons are then all correctly analyzed with a normal velocity component such that: $v_c^{\downarrow} < v_n < v_c^{\uparrow}$.

During T_3, the spin flipper is swiched on again. Therefore no neutrons should be detected. The fraction counted here corresponds to 1.8% of the total number detected. They are of two types: i) UCN that have been correctly analyzed just before the end of T_2 and have been detected during T_3 due to the flight distance between the spin flipper and the detector ; ii) and those that are located between

---

(3) Here $v_c^{\uparrow}$ ($v_c^{\downarrow}$) is the velocity corresponding to $V_F^{\uparrow}$ ($V_F^{\downarrow}$) as it has been denoted in the previous chapter.

the spin flipper and the foil at the end of T_1 when the spin flipper is about to be tuned off. This means that they are in the spin up state during T_2, flying above the foil and waiting for the spin flipper to be switched on again.

To quantify the analyzing power of the sequential method, we calculate the asymmetry [51]:

$$\frac{N_{off} - N_{on}}{N_{off} + N_{on}} \approx +95\%. \tag{12.5.1}$$

In a perfect case, this ratio is equal to 100% and N_{off} (N_{on}) corresponds to $N_{\downarrow}$ ($N_{\uparrow}$). The lower ratio is due to the UCN wrongly analyzed during T_1 and T_3 (2.5% of the total detected counts). It is important to note that, in the simulations, all neutrons are assumed to be 100% polarized. Furthermore, the spin flipper efficiency is 100%. Therefore, the asymmetry value partly results from the analyzing foil (i.e. the magnetization intensity and/or its location) and from the sequential method itself.

100% spin up in the nEDM chamber

Figure 12.5 shows the number of detected UCN as a function of the time. The percentages with respect to the total number of detected neutrons are also given in table 12.5. Contrary to the previous simulation, the neutrons have the spin down polarization at the level of the analyzer during T_1. About 68% of the total number of detected neutrons are counted there. They are all spin down neutrons and some

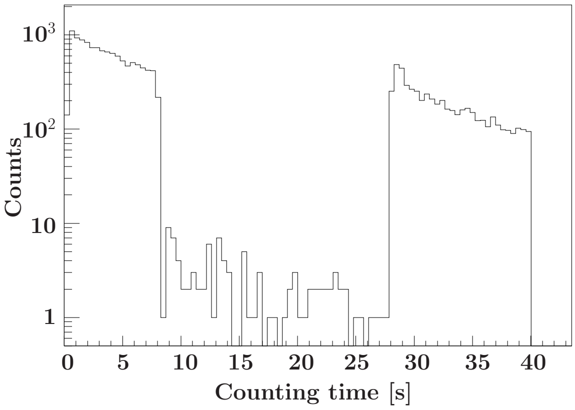

Figure 12.5: Counting time spectrum for initial spin up neutrons.

	$t \in T_1$	$t \in T_2$	$t \in T_3$	Whole sequence (40 s)
Spin down UCN	68.1%	0.9%	30.9%	99.9%
Spin up UCN	0.0%	0.1%	0.0%	0.1%
Total number	68.1%	1.0%	30.9%	100.0%

Table 12.5: Percentages of counts obtained with an initial population of spin up UCN.

of them have their normal velocity above $v_c^{\uparrow} = 7.6$ m/s at the foil surface. That means that they are not strictly well analyzed.

During T_2, the spin flipper is switched off. Although no UCN should be detected, 1% of the whole number of detected neutrons is registered: i) about half of these neutrons are analyzed at the end of T_1 and, due to the flight path, are detected during T_2 ; ii) The remaining neutrons are those that are located between the spin flipper and the analyzer when the spin flipper changes state from T_1 to T_2. These are spin down neutrons, but they don't have a sufficient normal velocity to pass through the analyzing foil. After some time, they finally succeed and it happens during T_2.

During the last time range T_3, 31% of the total number of detected neutrons are counted. They have been correctly analyzed by the foil (i.e. $v_c^{\downarrow} < v_{norm} < v_c^{\uparrow}$).

The efficiency of the spin analysis equals to:

$$\frac{N_{off} - N_{on}}{N_{off} + N_{on}} \approx -98\%. \tag{12.5.2}$$

That means that the system analyses the spin up component with an efficiency of 98%. The minus sign is inherent to the definition of the asymmetry variable.

Comparisons and conclusions

The asymmetries are different between the two previous simulations because the spin components are not analyzed during the same time intervals. We have seen that wrongly analyzed UCN come from: i) the limited range of velocities for the analyzer, ii) the distance between the spin flipper and the analyzing foil, and iii) that between the analyzer and the detector. The velocity range can be improved [45,51]. Indeed, here we have taken a quite low magnetization in the analyzing foil, preferring to choose something which is close to our experimental knowledge. The second point is hard to modify. No distance between the spin flipper and the foil would be the best. But it is pratically impossible because the stray field of the strong magnets located around the analyzer would disturb the weak magnetic field of the spin flipper and its tuning. Finally, the last point depends on geometrical constraints (i.e. switch box) as well as the critical velocity of the detector. It is then difficult to decrease the distance between the analyzer and the detector.

12.6 Simulation of the simultaneous spin analyzing system

12.6.1 Geometry and principle

The main motivation for the development of a simultaneous spin analyzing system resides in the increase of the UCN counting statistics. This could be realized by reducing the counting time, and therefore the reflection losses, during a single cycle.

Simultaneously analyzing both spin components is then naturally put forward. One needs two spin analyzing systems to analyse both spin components at the same time. Each of them will be made of a spin flipper, an analyzing foil and a detector. Note that although one spin flipper should be sufficient, the whole system is made symmetric. This comes from the experimental point of view where each arm should be well characterized in order to take into account possible systematic effects deriving from the spin analysis.

Figure 12.6 shows the geometries simulated with Geant4. Due to its "reversed-Y" shape, the simultaneous system will be named as "Y_θ" where θ is the angle (in °) between both analyzing devices. We will write "left arm" and "right arm" to denote each of them relatively to the incident neutron beam direction. In the simulations, the left spin flipper is always switched on and the right one is off.

The working principle for a perfect Y system is the following. Consider a spin down neutron which enters in the arm where the spin flipper is active. At the analyzing foil level, it comes in the spin up state and undergoes the upper Fermi potential. It is then reflected and goes back either inside the incoming guide or inside the second arm. This neutron will be detected once it penetrates in the arm where the spin flipper is off. Similarly, a spin up neutron will be detected if it enters in the active arm with spin flipper on.

In order to compare the simulations of the sequential system and the simultaneous one, the chamber and the vertical tube have the same dimensions and materials for both simulations. It should also be noted that the arms are identical — i.e. same spinflippers, analyzers, detectors, materials and dimensions — to the analyzing part of the sequential setup (cf. Fig. 12.3).

Y_{30} and Y_{120} geometries have been simulated with different initial spin populations of neutrons, either 100% spin down or 100% spin up. Each time, $N_0 = 25000$ UCN have been randomly shot within the chamber and with the initial velocity distribution at 100 s storage time shown in Fig. 12.2. The counting time is identical to that of the simulation of sequential method and equals 40 s. The losses and spin analysis efficiency of these systems will be discussed.

12.6.2 UCN losses

The Y_{120} system

Table 12.6 summarizes the losses inside the Y_{120} for two initial spin populations (100% spin down and 100% spin up). The losses are very similar for both spin configurations. About 20% of the initial number of neutrons (N_0) are lost in the whole geometry. The most important are within the chamber (about 8%); they are mainly reflection losses. Then those due to the absorption in the analyzing foil of the "active" arm equal to about 5.6-5.7%. The joining part, called trapezoid in the table, also absorbs about 3.2-3.3% of neutrons.

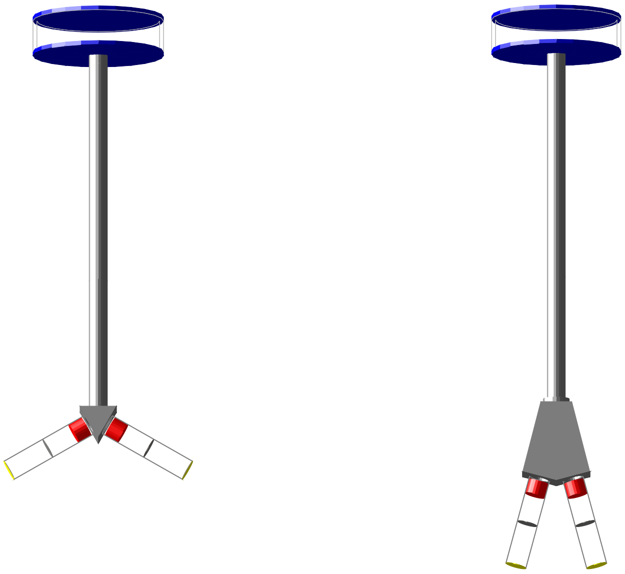

(a) EDM geometry with the Y_{120} (b) EDM geometry with the Y_{30}

Figure 12.6: Geant4 geometries of the Y systems developed for the simultaneous spin analysis method. (a) with an angle of 120° between both arms and (b) with an angle of 30°.

The $\mathbf{Y}_{30}$ system

Table 12.7 shows the loss percentages in the geometry for the initial spin up and spin down populations. The total losses in the geometry are about 3% lower than in the case of the Y_{120} and they are not distributed the same way in the geometry.

Between 40-70% more UCN are lost in the vertical tube with the Y_{120}. Due to gravity, UCN are more present in this volume than in the case of the Y_{30} during the entire simulation.

Concerning the trapezoid part, there are 20% more losses for the Y_{30} because of its larger inner surface.

There are 2-3 times more losses in the tubes of the Y_{120}. This is due to the orientation of the arms with respect to the vertical z axis. Consider two extreme situations: one with horizontal arms and another with vertical arms. When they enter in the Y system (Y_{30} or Y_{120}), the neutrons have a high vertical velocity component (between $5 - 7$ m/s). Therefore, one can understand that there will be more losses in the horizontal situation.

Since the analyzing foils are located lower in the Y_{30}, the neutron velocity is more important at this level and, inversely, there are less absorption losses ($1/v$-law) than for the Y_{120}. This is true for the arm where the majority of neutrons are detected. For the Y_{30}, we note about 4.7% of losses within the analyzer, which is 20% less than in the case of the Y_{120}. In contrast, for the other arm where no neutrons should

	S_1	S_2
Chamber	8.09	7.85
Vertical tube	1.78	1.58
Trapezoid	3.22	3.30
Left arm tube	1.36	1.70
Right arm tube	1.80	1.50
Left foil	0.05	5.72
Right foil	5.58	0.03
Total Losses	21.88	21.68

Table 12.6: Summary of the UCN losses for both Y_{120} simulations in which the initial UCN polarization is either down (S_1) or up (S_2). The results are given in terms of percentages with respect to the initial number of shot neutrons ($N_0 = 25000$) in each simulation.

	S_1	S_2
Chamber	8.41	7.74
Vertical tube	1.04	1.14
Trapezoid	3.84	4.07
Left arm tube	0.58	0.56
Right arm tube	0.59	0.55
Left foil	0.10	4.68
Right foil	4.66	0.11
Total Losses	19.22	18.85

Table 12.7: Summary of the UCN losses for both Y_{30} simulations in which the initial UCN polarization is either down (S_1) or up (S_2). The results are given in terms of percentages with respect to the initial number of shot neutrons ($N_0 = 25000$) in each simulation.

be detected, there is an increase of losses. For the Y_{30}, they are equal to about 0.1% whereas for the Y_{120}, they are 2-3 times less. Indeed in the case of the Y_{30}, more neutrons penetrate inside the analyzer since its z-location is lower than for the Y_{120}.

12.6.3 Spin analysis efficiency

The Y_{120} system

Table 12.8 summarizes the percentages of detected neutrons for both arms and for each initial spin component. The normalization is done with respect to the total numbers N_{tot} of detected neutrons. For the down case, the simulations gave $N_{tot} = 17557$ and for the up case, $N_{tot} = 17619$. UCN have been counted for 40 s.

Let us detail the results given in table 12.8 for the case of an initially down-polarized population of neutrons.

- The left arm:
  Since the spin flipper of this arm is always tuned on, we expect to detect only spin up neutrons. Therefore, no counts should be observed since all the

	100% spin down neutrons				100% spin up neutrons			
	Left arm		Right arm		Left arm		Right arm	
Spin state	up	down	up	down	up	down	up	down
N/N_{tot} [%]	0.11	0.22	0.00	99.67	0.01	99.64	0.17	0.18
Asymmetry [%]	99.3				-99.3			

Table 12.8: Percentages of detected neutrons in the Y_{120} simulation. For the calculations, the initial UCN spin population is either 100% down or 100% up. The results are given in terms of percentages with respect to the total number of detected neutrons N_{tot} in each simulation. The asymmetries between the two arms are also given.

neutrons are initially in a spin down state. 0.11% of UCN are detected with a spin up polarization. This is because they have, at the analyzer foil position, a normal velocity larger than the critical velocity of the upper edge: $v_n > v_c^{\uparrow}$. The 0.22% spin down neutrons have normal velocities at the foil position such that: $v_c^{\downarrow} < v_n < v_c^{\uparrow}$. They are detected because they experience a spin flip during a collision before the analyzer. They represent about 75% of the total number of spinflips at collisions in the whole simulation.

- The right arm:
  Since the initial neutrons are down-polarized, the majority (99.67%) of all the detected neutrons ends in the right detector. It can be inferred from the left arm results that about 0.11% of neutrons are detected because they have crossed the analyzer with $v_n > v_c^{\uparrow}$. It follows that in the whole simulation only about 0.22% of the detected UCN are wrongly analyzed. This is explained by the fact that the distance between the chamber and the analyzing foils is well adjusted for this geometry. In other words, the normal velocity distribution is almost entirely located between the two critical velocities $v_c^{\downarrow}$ and $v_c^{\uparrow}$ at the foil level.

For the Y systems, the asymmetry can be written as:

$$\frac{N_{right} - N_{left}}{N_{right} + N_{left}}. \tag{12.6.1}$$

For initially spin down neutrons, it gives 99.3%.

The simulation performed with initially spin up neutrons gives results similar to those obtained with down-polarized neutrons. Here, about all the detected UCN are in the left detector. The asymmetry equals to -99.3%, which identical in absolute from the previous case.

The Y_{30} system

Table 12.9 shows the counts and asymmetry results for the Y_{30} simulation. The counts are given with respect of the total numbers N_{tot} of neutron detected. For the down case, calculations have given $N_{tot} = 18478$ and for the up case, $N_{tot} = 18603$. One can do the same analysis that for the Y_{120}. It is interesting to note that the

	Initial spin down neutrons				Initial spin up neutrons			
	Left arm		Right arm		Left arm		Right arm	
Spin state	up	down	up	down	up	down	up	down
N/N_{tot} [%]	1.70	0.16	0.01	98.13	0.00	97.97	1.89	0.14
Asymmetry [%]	96.3				-95.9			

Table 12.9: Percentages of detected neutrons in the Y_{30} simulation. For the calculations, the initial UCN spin population is either 100% down or 100% up. The results are given in terms of percentages with respect to the total number of detected neutrons N_{tot} in each simulation. The asymmetries between the two arms are also given.

number of neutrons detected in the "inactive" arm has increased if we compare with the Y_{120} (cf. table 12.9). In fact, the reduction of the angle between both arms has caused an increase of the distance between the chamber and the analyzers position. Thus, due to the gravitational boost, the neutrons have a higher normal velocity at the foil position. So, more neutrons with $v_n > v_c^{\uparrow}$ can cross the foil and decrease the asymmetry value.

12.7 Comparison of the counting times for both methods

Both spin analysis system have been simulated over a counting period of 40 s. The number of counts obtained for the sequential spin analysis is taken as reference. We have calculated with respect to the emptying curve of the Y systems, the times needed for the Y_{30} and Y_{120} to reach the reference number given by the sequential method. Table 12.10 gives the results. For both initial spin state, we find the same results.

	Y_{30}	Y_{120}
Gain in counting time [%]	41	25

Table 12.10: Gain in counting time of the Y systems with respect to the sequential method of spin analysis.

Both Y systems are faster than the sequential system. The Y_{30} is the fastest due to its smaller angle between both arms.

12.8 Conclusions

Table 12.11 summarizes the results obtained for the UCN counts, losses in the geometry and the asymmetry parameter. Each system has been simulated with the same materials and two different initial spin populations of UCN (100% spin down or 100% spin up). The initial velocity distribution is obtained after a storage of 100 seconds inside a DPS/DLC UCN chamber.

	Sequence		Y_{120}		Y_{30}	
N_{tot}/N_0 [%]	64.1	66.4	70.2	70.5	73.9	74.4
Losses in geometry [%]	22.0	19.5	21.88	21.68	19.22	18.85
Asymmetry [%]	95.0	-98.0	99.3	-99.3	96.3	-95.9

Table 12.11: Summary of the simulations of the sequential and simultaneous systems. The results are given for initial spin down (left numbers) and spin up (right numbers) populations. The percentages of neutrons detected N_{tot} with respect to the initial number N_0 of shot UCN are given. The asymmetries and the percentages of losses are also summed up.

When initiating this study, it was expected that the losses in the sequential geometry would be higher than that of the Y systems. The results of the simulations have shown that it is not really the case. The losses are very similar. It can be seen from table 12.11 that the smallest losses are obtained for Y_{30} system.

Whereas the Y_{120} shows the largest asymmetry, the Y_{30} has lower values because of the neutrons which are wrongly analyzed due to the gravitational boost. When comparing the number of detected neutrons over 40 s, the Y_{120} enables to count 6.1%-9.6% more neutrons than the sequential methods (depending on the initial spin population of UCN). For the Y_{30}, it is 12.0%-15.3%.

Thus, the Y_{30} system should enable to count more neutrons with slightly less losses in the geometry and with an equivalent analyzing power than the sequential system. Moreover, the Y_{30} is 41% faster than the sequential method whereas the Y_{120} is only 25% faster.

Chapter 13

Experimental tests of polarization analysis

In this chapter, experimental results are reported about the performances of the devices used for UCN spin analysis (i.e. polarizer, analyzer and spin flipper). They constitute a preliminary work for the development of simultaneous spin analysis systems. Two such systems (Y_{120} and Y_{30}) have been tested. They are described in section 13.2.

13.1 Performances of the spin analyzing elements

The polarization/analysis process by transmission through magnetized iron foils can be modelized with matrix transitions [51]. The relation between the spin populations before and after the polarizer/analyzer can be written as:

$$\begin{pmatrix} I^+ \\ I^- \end{pmatrix} = \begin{pmatrix} a_{11} & a_{12} \\ a_{21} & a_{22} \end{pmatrix} \begin{pmatrix} I_0^+ \\ I_0^- \end{pmatrix}, \tag{13.1.1}$$

(I_0^+, I_0^-) are the initial beam intensities of both spin states, (I^+, I^-) are the those after the foil transmission. The a_{11} term corresponds to the proportion of spin up which are transmitted through the foil. Since only spin down UCN are able to cross the analyzing foil (see chapter 11 for more details), a_{11} may be considered as 0. The same argument applies for a_{21} which stands for the proportion of spin up neutrons that could have been depolarized during transmssion: $a_{21} = 0$. a_{22} is the amount of transmitted UCN in the spin down state. This should be the main quantity. Finally, one may consider the existence of the small fraction a_{12} of spin down UCN which are spin flip when crossing the foil [43, 51]. Such depolarization may be due to some interactions at the boundary of magnetic domains within the foil.

Hence, the transmission model of the polarizer/analyzer can be simplified to [51]:

$$\begin{pmatrix} I^+ \\ I^- \end{pmatrix} = \begin{pmatrix} 0 & a_{12} \\ 0 & a_{22} \end{pmatrix} \begin{pmatrix} I_0^+ \\ I_0^- \end{pmatrix}, \tag{13.1.2}$$

In the following, this model will be applied to the different tests performed at

ILL/PF2. The efficiencies of the spin flipper and that of the polarizer/analyzer will be extracted.

13.1.1 Main elements of the set-up

The polarizing and analyzing set-up

The polarizing and the analyzing foils are made of aluminum with a thin iron layer deposited onto an aluminium substrate. Several thicknesses have been tested for the iron layer (from 200 nm up to 1 μm thick) as well as for the Al substrate (from 13 up to 100 μm thick). Deposition were done by evaporation (LPC) or sputtering (PSI). Figure 13.1 shows a picture of the system used to magnetize the foils. The permanent magnets were either large pieces (see Fig. 13.1) of AlNiCo and/or tiny magnets made of NdFeB. They hold on a frame (yoke) made of iron. The resulting magnetic field intensity measured with a Hall probe at the center of the system is about 200-400 Gauss, depending on the magnets. With such an excitation field, the saturation magnetization within the iron foil (i.e. $B_{sat} = 2$ T) is expected to be reached [46, 47].

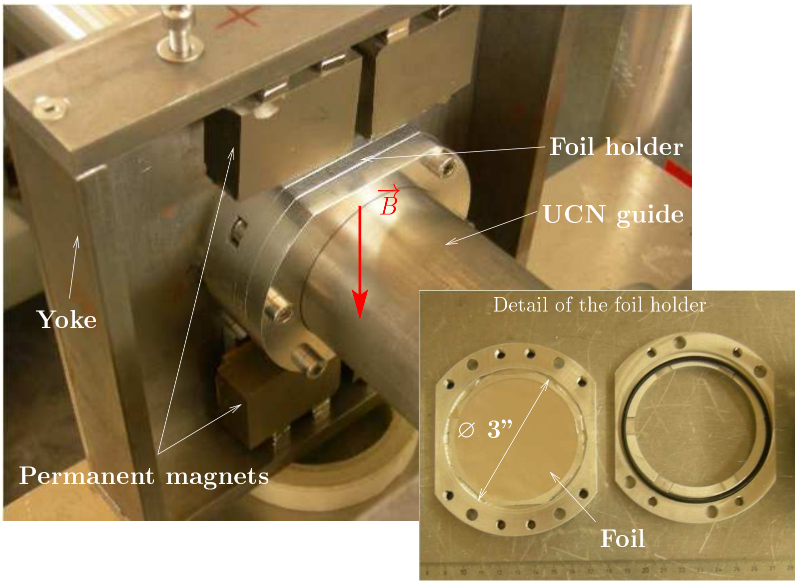

Figure 13.1: System of magnetization for the polarizing/analyzing foils.

The adiabatic spin flipper

Figure 13.2 shows the set-up around the adiabatic spin flipper. As it has been explained in chapter 11, the adiabatic flipping of UCN spins requires two magnetic fields: a static field gradient and an oscillating magnetic field.

Two options have been tested in order to produce the field gradient. First a cage has been used (see Fig. 13.2). The aluminium bars of the cage are filled with permanent magnets which creates a vertical field gradient. It is about 0.2 Gauss/cm.

The cage is located such that the magnetic field is uniform along the vertical axis, i.e. on the top and below the spin flipper guide tube. The second option used the stray field from the magnetization system of the polarizer/analyzer [50, 51].

The oscillating magnetic field oscillates perpendicularly to the vertical field gradient. It is created with a copper coil wounded around a plastic tube. Practically, a simple copper foil is inserted inside the spin flipper tube. An oscillating current with an amplitude of about 1 A was used for the copper coil. The resulting amplitude of the RF magnetic field can be calculated. It is about 5 Gauss for a coil of 100 turns over 24 cm. Following the equation (11.2.9), the adiabatic parameter η equals to 350 for an UCN velocity of 20 m/s. Since $\eta \gg 1$, the adiabatic condition is fulfilled at 20 m/s. It also works for lower velocities since the value of η increases.

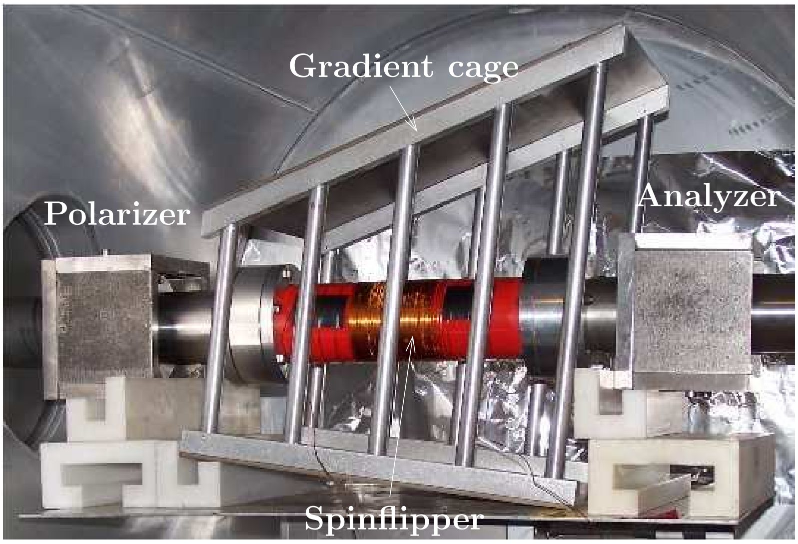

Figure 13.2: Devices used for spin analysis measurements.

13.1.2 Measurements

Polarizing efficiency

Figure 13.3 shows the scheme of the measurement. UCN from the ILL/PF2 turbine are chopped and polarized by transmission through a polarizing foil. Then their spin is adiabatically flipped within a spin flipper of 24 centimeters length. A spin analyzing foil ends the procedure prior to detection. The polarizer and the analyzer are assumed to be identical since the same set-up is used for the magnetization systems and since both foils come from the same sputtered sample. Note that special care is taken not to have zero magnetic field regions between the polarizer and the analyzer in order to avoid UCN depolarizations.

The resonant frequency of the spin flipper is found by varying that of the oscillating magnetic field. Since the polarizer and the analyzer are crossed by the same spin state, the minimum counting rate indicates that the spin flip (i.e. the resonance) occurs. Typical resonant frequencies were found about 15 kHz with the cage set-up described previously.

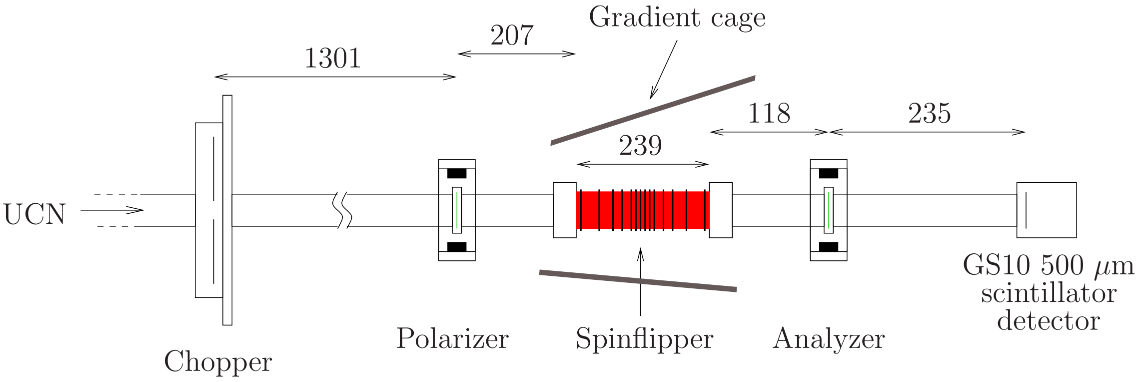

Figure 13.3: Scheme of the set-up used for polarization efficiency measurement. Distances are in mm.

In the following, I_0 and I_1 denote respectively the counting rate measured when the spin flipper is off and on. f is the flipping efficiency. I^+ and I^- are the beam intensities of the spin up and the spin down populations.

The polarizing efficiency p is defined as:

$$p = \frac{I_p^- - I_p^+}{I_p^- + I_p^+}, \tag{13.1.3}$$

where $I_p = I_p^+ + I_p^-$ is the beam intensity after the polarizer. From the matrix model defined at the beginning of this section, the expression of the polarizing efficiency may be calculated as a function of I_0 and I_1. One may write:

$$\begin{pmatrix} I_0^+ \\ I_0^- \end{pmatrix} = \begin{pmatrix} 0 & a_{12} \\ 0 & a_{22} \end{pmatrix} \begin{pmatrix} I_p^+ \\ I_p^- \end{pmatrix}, \tag{13.1.4}$$

$$\begin{pmatrix} I_1^+ \\ I_1^- \end{pmatrix} = \begin{pmatrix} 0 & a_{12} \\ 0 & a_{22} \end{pmatrix} \begin{pmatrix} 1-f & f \\ f & 1-f \end{pmatrix} \begin{pmatrix} I_p^+ \\ I_p^- \end{pmatrix}, \tag{13.1.5}$$

At the time of detection, both spin components are added together. One may found:

$$I_0 = I_0^+ + I_0^- = (a_{12} + a_{22})\, I_p^-, \tag{13.1.6}$$

$$I_1 = I_1^+ + I_1^- = (a_{12} + a_{22}) \Big[f I_p^+ + (1-f) I_p^- \Big]. \tag{13.1.7}$$

The expressions (13.1.6) and (13.1.7) enable to write I_p^+ and I_p^- as a function of I_0, I_1 and f. Therefore, p is calculated as:

$$p = \frac{I_0 - I_1}{(2f-1)I_0 + I_1}. \tag{13.1.8}$$

Experimentally, a flipping efficiency f close to 100% is easily obtained (see the measurement of the flipping efficiency further in this chapter). As a result, the polarizing efficiency is simplified to the asymmetry:

$$p \approx \frac{I_0 - I_1}{I_0 + I_1}. \tag{13.1.9}$$

Figure 13.4(a) shows velocity distributions obtained with the set-up of Fig. 13.3. Two measurements have been performed with the spin flipper off and on. For the latter, a cut is clearly visible about 7 m/s. Below this velocity, no UCN are detected due to the action of the spin flipper. Figure 13.4(b) plots the polarizing efficiency as a function of the UCN longitudinal velocity. For UCN velocities below 7 m/s, the value is above 90%.

The velocity range where the spin analysis can be performed is related to the intensity of the saturation magnetization within the foils. For the iron layer, a saturation at about 2 Tesla is expected. This corresponds to a velocity range between 4.1 and 8 m/s (see table 11.1). The measured range is lower and may be due to an incomplete saturation magnetization.

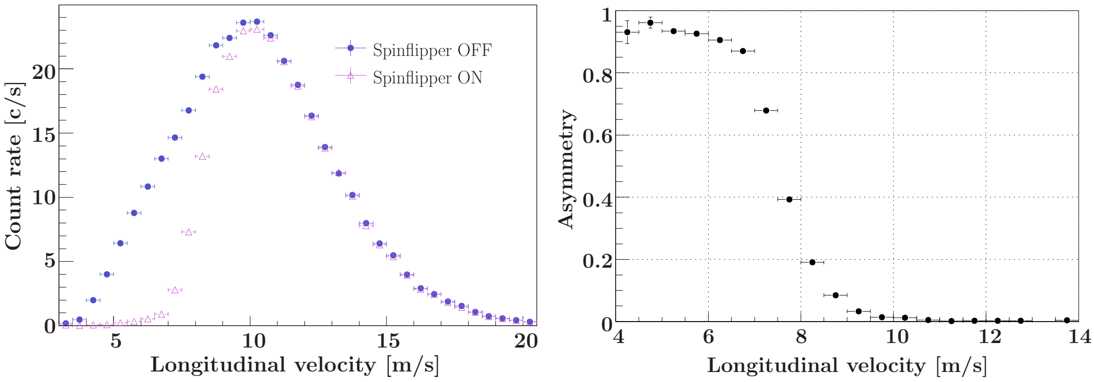

(a) (b)

Figure 13.4: Polarization measurements performed at ILL/PF2 EDM beamline.

Feasibility of short spin flippers

With the same set-up as in Fig. 13.3, several tests have been realized by varying the length of the spin flipper. Indeed, short spin flippers would enable to build compact spin analyzing device. It is especially interesting for the development of the simultaneous system (see section 13.2).

Figure 13.5 shows the polarizing efficiency as a function of the velocity for four spin flipper lengths with the associated number of turns of the coil.

The measurements show that a spin flipper with a length of 1 cm with only 8 turns is still efficient to flip the UCN spins. The current and magnetic field intensities used for the different runs are given in table 13.1. The adiabaticity parameter η is calculated using equation (11.2.9) for a UCN velocity of 7 m/s. The adiabatical condition is not fulfilled anymore for the case of 2 turns over 2 mm. This explains the low asymmetry observed in Fig. 13.5 for the shortest spin flipper.

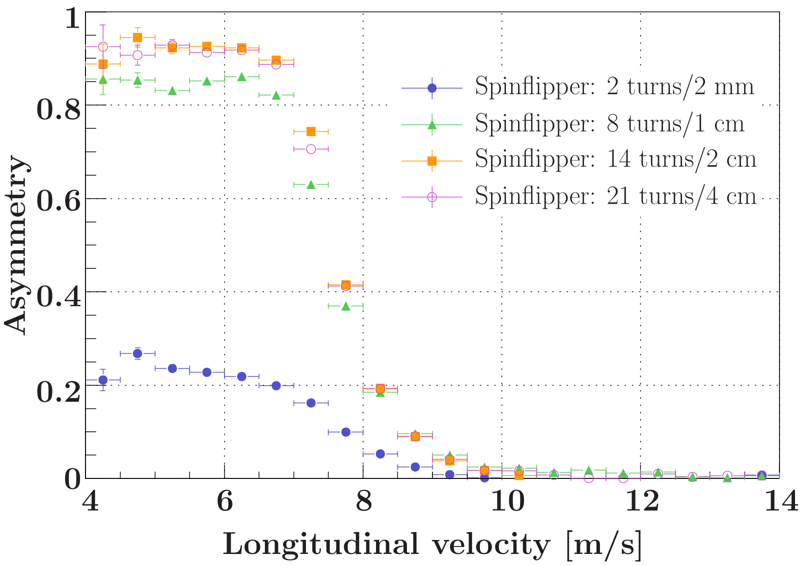

Figure 13.5: Polarizing efficiency vs spin flipper length.

Coil (turns/length)	2 t/2 mm	8 t/1 cm	14 t/2 cm	21 t/4 cm
Current amplitude [A]	2.5	2.5	2.2	2.8
Magnetic field [Gauss]	0.9	3.5	5.3	9.2
η(7 m/s)	1.5	29.2	88.3	307

Table 13.1: Magnitude of the oscillating current provided to the different spin flipper coils. The corresponding magnetic field amplitude as well as the adiabatic parameter η are calculated.

Flipping efficiency

The use of two spin flippers enables to determine their flipping efficiency [51]. Figure 13.6 shows the scheme of the experiment performed in order to measure both spin flip efficiencies.

With two spin flippers, four combinations may be achieved. The corresponding beam intensities are denoted I_{00}, I_{01}, I_{10} and I_{11}. The first (second) index represents the state of the spin flipper A (B). When the spin flipper is on (off), the index is 1 (0). f_A and f_B stand for the flipping efficiencies of the spin flippers A and B, respectively.

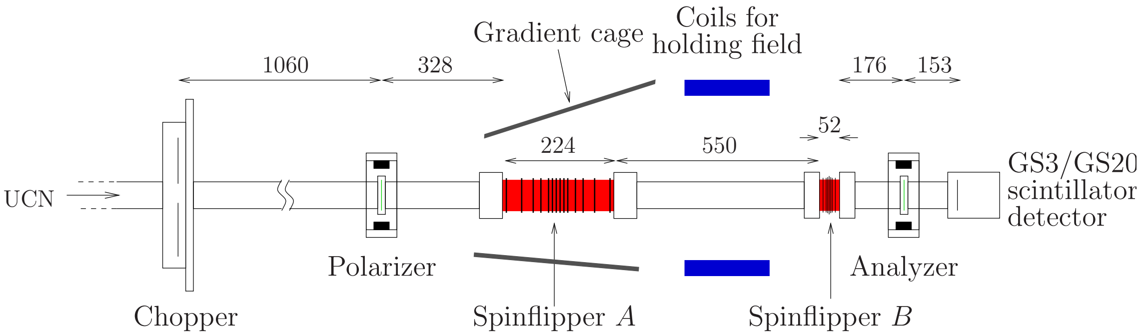

Figure 13.6: Scheme of the set-up dedicated to the flipping efficiency measurement. Distances are in mm.

The four intensities can be derived as follows:

$$I_{00} = (a_{12} + a_{22})\, I_p^-, \tag{13.1.10}$$

$$\begin{pmatrix} I_{01}^+ \\ I_{01}^- \end{pmatrix} = \begin{pmatrix} 0 & a_{12} \\ 0 & a_{22} \end{pmatrix} \begin{pmatrix} 1-f_B & f_B \\ f_B & 1-f_B \end{pmatrix} \begin{pmatrix} I_p^+ \\ I_p^- \end{pmatrix}, \tag{13.1.11}$$

$$\begin{pmatrix} I_{10}^+ \\ I_{10}^- \end{pmatrix} = \begin{pmatrix} 0 & a_{12} \\ 0 & a_{22} \end{pmatrix} \begin{pmatrix} 1-f_A & f_A \\ f_A & 1-f_A \end{pmatrix} \begin{pmatrix} I_p^+ \\ I_p^- \end{pmatrix}, \tag{13.1.12}$$

$$\begin{pmatrix} I_{11}^+ \\ I_{11}^- \end{pmatrix} = \begin{pmatrix} 0 & a_{12} \\ 0 & a_{22} \end{pmatrix} \begin{pmatrix} 1-f_B & f_B \\ f_B & 1-f_B \end{pmatrix} \begin{pmatrix} 1-f_A & f_A \\ f_A & 1-f_A \end{pmatrix} \begin{pmatrix} I_p^+ \\ I_p^- \end{pmatrix}. \tag{13.1.13}$$

Defining $\alpha = (a_{12} + a_{22})$, these equations can be simplified as:

$$I_{00} = \alpha\, I_p^-, \tag{13.1.14}$$

$$I_{01} = I_{01}^+ + I_{01}^- = \alpha\big[f_B I_p^+ + (1-f_B) I_p^-\big], \tag{13.1.15}$$

$$I_{10} = I_{10}^+ + I_{10}^- = \alpha\big[f_A I_p^+ + (1-f_A) I_p^-\big], \tag{13.1.16}$$

$$I_{11} = I_{11}^+ + I_{11}^- = \alpha\Big(\big[f_A(1-f_B) + f_B(1-f_A)\big] I_p^+ + \big[(1-f_B)(1-f_A) + f_A f_B\big] I_p^-\Big). \tag{13.1.17}$$

f_A can be calculated by using equations (13.1.15) and (13.1.17). This leads to:

$$I_{11} = I_{01}(1-2f_A) + f_A(\alpha I_p^+ + I_{00}). \tag{13.1.18}$$

From (13.1.16) and (13.1.14), one writes $\alpha I_p^+ = (I_{10} - (1-f_A) I_{00})/f_A$. Inserting this expression in (13.1.18) leads to f_A [50]:

$$f_A = \frac{1}{2}\Big(1 - \frac{I_{11} - I_{10}}{I_{00} - I_{01}}\Big). \tag{13.1.19}$$

Similarly, one finds:

$$f_B = \frac{1}{2}\Big(1 - \frac{I_{11} - I_{01}}{I_{00} - I_{10}}\Big). \tag{13.1.20}$$

Figure 13.7 shows the corresponding flipping efficiencies f_A and f_B measured at ILL/PF2 as a function of the velocity. Within the velocity range of interest, the flipping efficiencies are very close to 100% ($f_{A,B}$ ~99%). As a result, the efficiency of the whole system mainly depend on the polarizer and analyzer efficiencies.

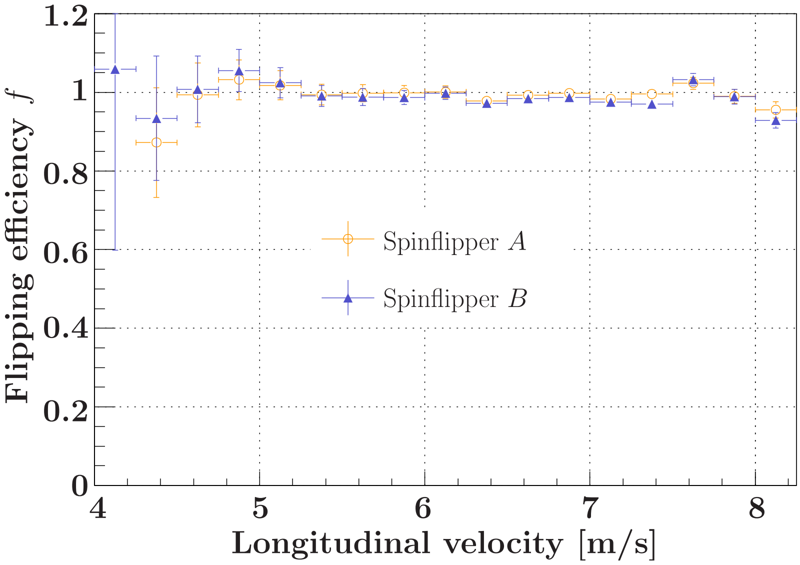

Figure 13.7: Flipping efficiencies as a function of the UCN longitudinal velocity. The measurement was done at the ILL/PF2 TEST beamline.

13.1.3 Conclusions

The development and the optimisation of the devices used for spin analysis have been performed during these preliminary tests. A polarizing/analyzing efficiency of about 90% has been measured. The flipping efficiency of our adiabatic spin flippers is consistent with 100%, even for spin flippers with a few centimeters length. These tests have been used for the development of simultaneous spin analysis systems.

13.2 The simultaneous spin analysis system

Tests have been performed at ILL/PF2 TEST beamline with the Y_{30} and Y_{120} set-up. The transmission and spin analysis capabilities have been measured as a function of the UCN velocity.

13.2.1 Description of the Y systems

Figure 13.8 shows the two simultaneous spin analysis devices standing horizontally.

They are made of stainless steel (316L). Since it is a magnetic material, copper foils polished by hand have been inserted within the whole system (see Fig. 13.9(a)). The analyzing foils are made of 100 μm thick Al foil (Goodfellow 99% purity) with 200 nm of sputtered iron.

The effective length of the spin flippers has been reduced to 5 cm (see Fig. 13.9(b)). The distance between the spin flippers and the analyzing foils is 10 cm. That between the analyzers and the entrance face of the detectors is 14 cm. The total length of the arms (from the joining part to the detector entrance) is 40 cm.

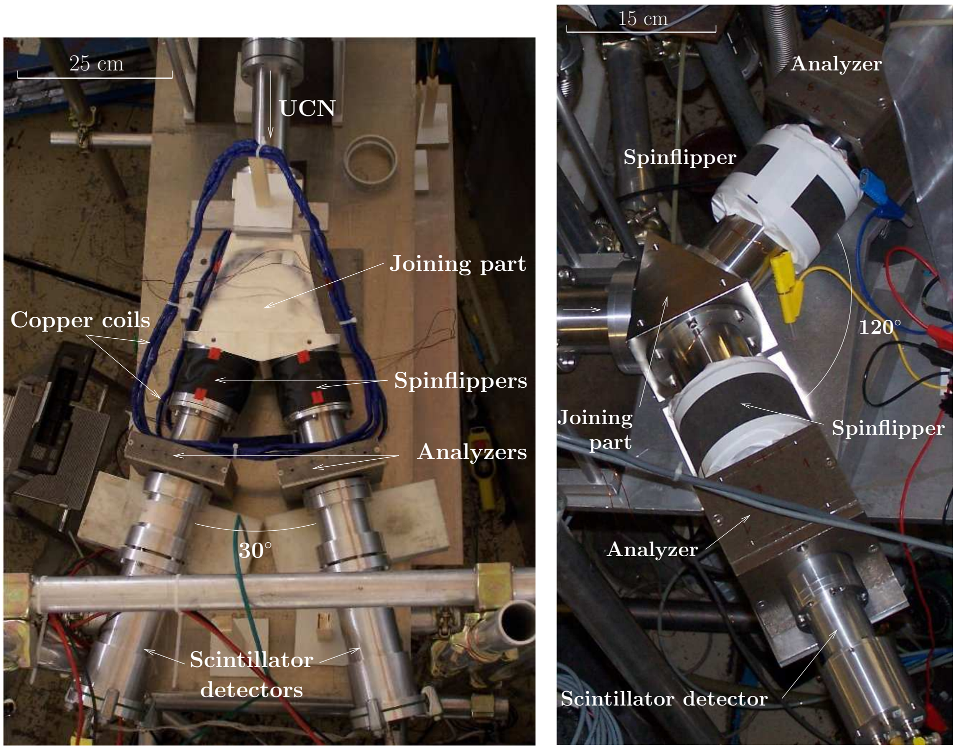

(a) Y_{30} (b) Y_{120}

Figure 13.8: Simultaneous systems in operation.

The detectors used for the two arms are GS10 scintillators. They have a thickness of 500 μm for the right arm and 100 μm for the left one⁽¹⁾.

13.2.2 Transmission measurements

The transmission of the single arms as well as that of the complete Y_{30} and Y_{120} systems have been measured. Figure 13.10 shows a sheme of the experimental procedure. The chopper is used to get the TOF information. No foils have been mounted, neither for polarizing nor analyzing. Therefore, the spin flipper are not used during these transmission measurements (off-state).

Step 1 is the reference measurements. It consists in measuring the beam intensities. Then the arms are added to the beamline: this is step 2. Note that Step 1 and 2 are performed twice since two GS10 detectors are used. Finally, the Y_{30} and Y_{120} sytems are tested during Step 3.

Case of the single arms

Figure 13.11 shows the velocity spectra for Step 1 (reference measurement) and Step 2 (measurement with arm) for both arms. Although the velocity distributions are very similar, it can be noted that the count rate is 10% higher for the right detector.

---

(1) At that time, it was not possible to buy identical scintillators to perform such tests.

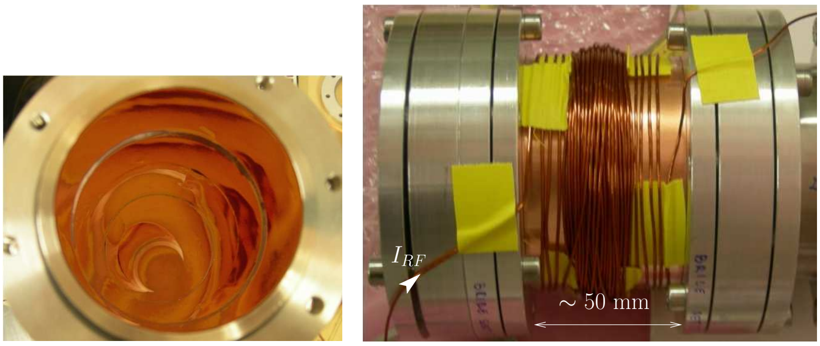

(a) Coating made with copper foils

(b) Spinflipper

Figure 13.9: Details of some elements of the Y systems.

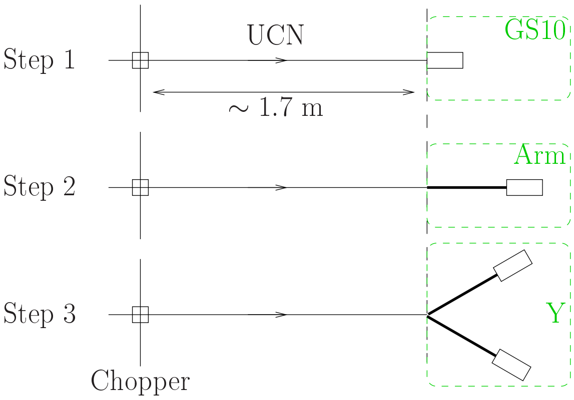

Figure 13.10: Procedure used for the measurement of the UCN transmission.

It has been already shown (see chapter 10) that the 500 μm thick GS10 is about 30% more efficient than the 100 μm thick GS10 on the TEST beamline. Here the cleaning of the spectra for the 500 μm thick GS10 was not optimal since only relative measurements had to be performed. For this detector, only events associated with a complete energy deposition have been selected. This explains why the relative efficiency between the thick scintillator and the thin one is only 10%.

The transmission is defined as the velocity distribution of Step 2 divided by that of Step 1. The two curves for each arm are plotted in Fig. 13.12.

Both arms have a similar transmission. It is about 60% between 4 and 11 m/s. The increase for higher velocities may be explained by the fact that neutrons with such high longitudinal velocities bounce less onto the inner surface of the guide tube. The transmission is consequently larger.

Case of the Y system

The procedure for the determination of Y system transmission is similar than for the single arms. Since both arms are identical, only the counting rate measured for the left arm is considered to estimate the transmission of the whole Y system.

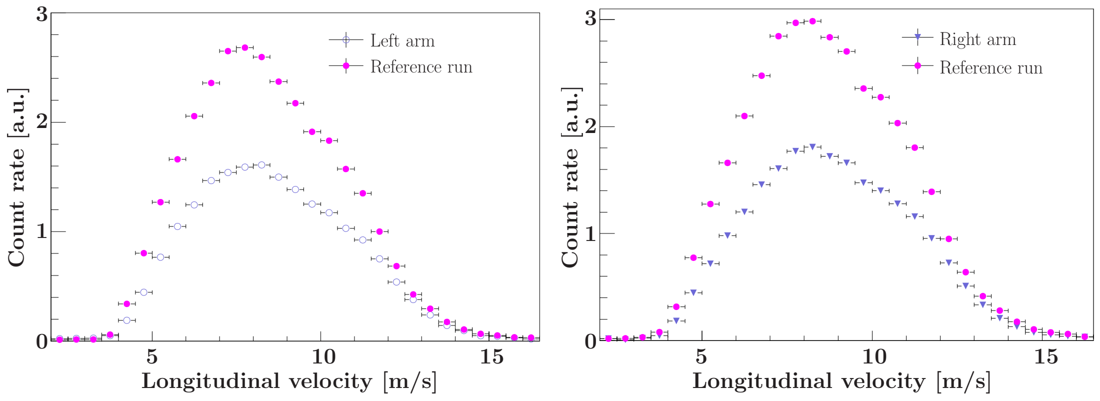

(a) (b)

Figure 13.11: Velocity distributions measured with the single arms. The reference curves (Step 1) have been obtained with the corresponding detectors.

Figure 13.13(a) shows the velocity distributions for the left arm measured with the Y_{30} and Y_{120} systems. The reference measurement (Step 1) with the corresponding detector (100 μm thick GS10) is also plotted. The velocity distribution obtained with the Y_{120} is dramatically softened. Neutrons with longitudinal velocity higher than 10 m/s are not transmitted. They are lost in the joining part although it is coated with copper foil.

The transmission is calculated by dividing the velocity spectra of the left arm obtained with the Y_{30} and Y_{120} by the distribution of Step 1. Note that the counting rate of the left arm was multiplied by two since the right arm was not considered in the calculation(2). Figure 13.13(b) shows the corresponding transmission curves for the Y systems. The transmission of the Y_{30} system is about 47% between 4 and 11 m/s, and then increases up to 60% between 12 and 15 m/s. Such a geometry is more convenient for UCN with a high longitudinal velocity due to the small angle between the two arms. In contrast, the Y_{120} kills all the UCN with a velocity between 10 and 15 m/s. Its transmission is lower than 20% for UCN longitudinal velocities below 10 m/s. The transmission of the Y_{30} device is in any case larger than that of the Y_{120}.

13.2.3 Measurement of the polarization efficiency

The procedure is similar to the transmission measurement. The polarizer is added upstream into the beamline. A static magnetic field is also produced between the polarizer and the analyzer in order to maintain the UCN polarization. The gradient field required by the adiabatic spin flipper is the stray field from the magnetizing system of the analyzer. The measurement principle is described in section 13.1.2. Two measurements were performed: one with the spin flipper switched on and another

---

(2) Another method would be to sum the rate from both arms, and then compare it with the mean rate obtained for the two detectors in Step 1. The transmission obtained with this method is the same than that actually presented here

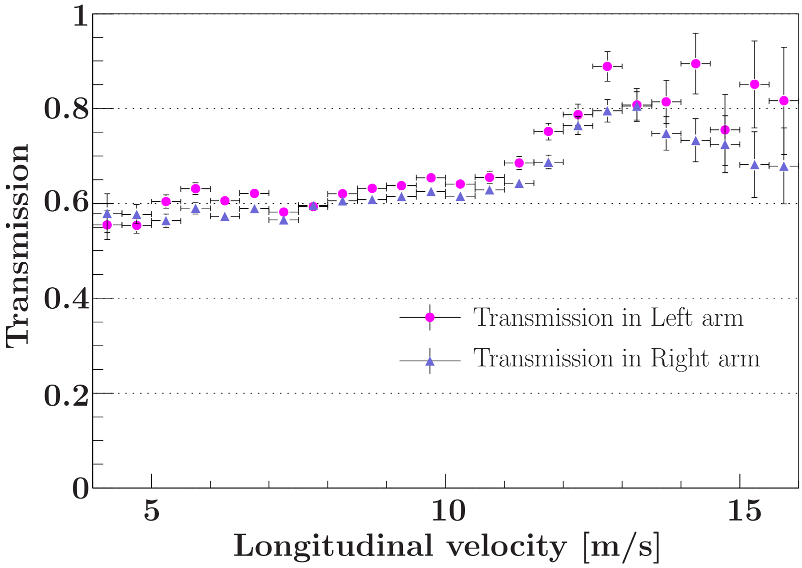

Figure 13.12: UCN transmission in the left and right arms tested under the Step 2 configuration.

with the spin flipper off. Then the asymmetry parameter was extracted following the equation (13.1.9).

Case of the single arms

The polarization efficiency was measured for each arm in the straight configuration. Figure 13.14 shows the corresponding velocity distributions measured at the TEST beamline.

When the spin flipper is on, the cut at low velocities is not complete as it appeared for the preliminary tests (see Fig. 13.4(a)). Nevertheless, both arms have the same cut, hence the same analyzing efficiency. Indeed, the asymmetries of the left and right arms are shown in Fig. 13.15. A value about 80% is found for both below 6.5 m/s. During these tests, higher values could not be achieved unfortunately. The following precautions have been taken anyway:

- The polarizer/analyzer and the magnetizing systems are the same than those used in section 13.1.2. The intensity of the external magnetic field at the foil center is about 400 Gauss which is sufficient to magnetize the iron layer [47].

- Regions with zero magnetic fields have been suppressed with the holding magnetic field. No zero field regions have been measured using a hall probe between the polarizer and the analyzer.

- The resonance of the adiabatic spin flipper has been clearly measured. No external field did modify this resonance during the measurement. From the fields amplitudes, the adiabatic coefficient has been calculated. It is larger than 700.

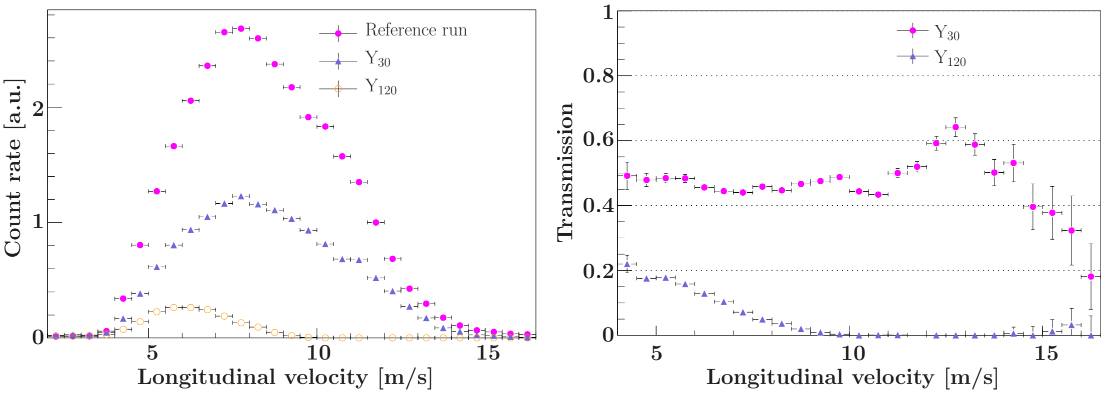

(a) (b)

Figure 13.13: Results of the transmission tests in the Y systems. The reference curve is measured in Step 1 with the 100 μm thick GS10. The velocity distributions of the Y systems have been scaled up by a factor two in order to be compared with the reference curve.

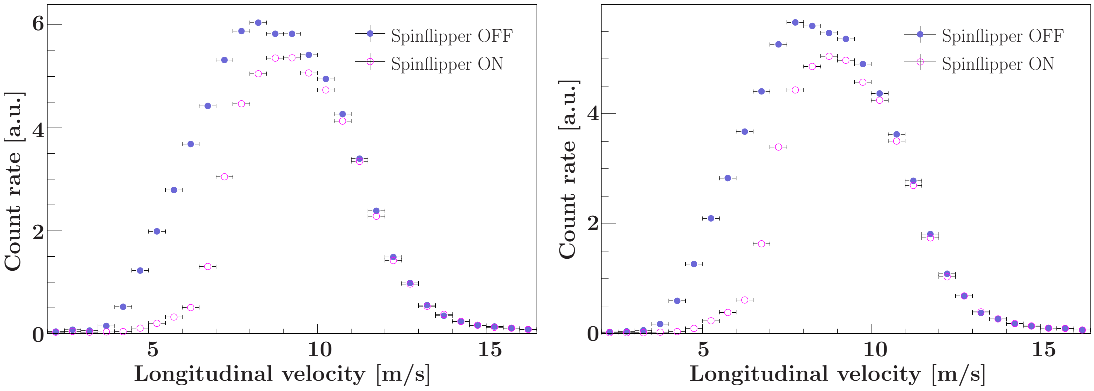

(a) Left arm (b) Right arm

Figure 13.14: Velocity spectra for SF ON and OFF for the single arms.

- No magnetic materials have been used within the guide tubes: there is mainly copper in the system.

Case of the Y system

Only the Y_{30} has been tested since the transmission of the Y_{120} system is very low on the TEST beamline. Figure 13.8(a) shows a picture of the Y_{30} in operation. Two runs have been performed: for the run 1, the left spin flipper is switched on and the right one is off; for the run 2, the opposite configuration is taken. The asymmetry parameters of each arm have been extracted to estimate the spin analyzing efficiency of the simultaneous system. Figure 13.16 shows the velocity spectra measured for each arm with their respective spin flipper switched on or off. The detector of the right arm (500 μm thick GS10) is more efficient at high velocities than that of the left arm (100 μm thick GS10). As a result, more UCN are detected at high velocity

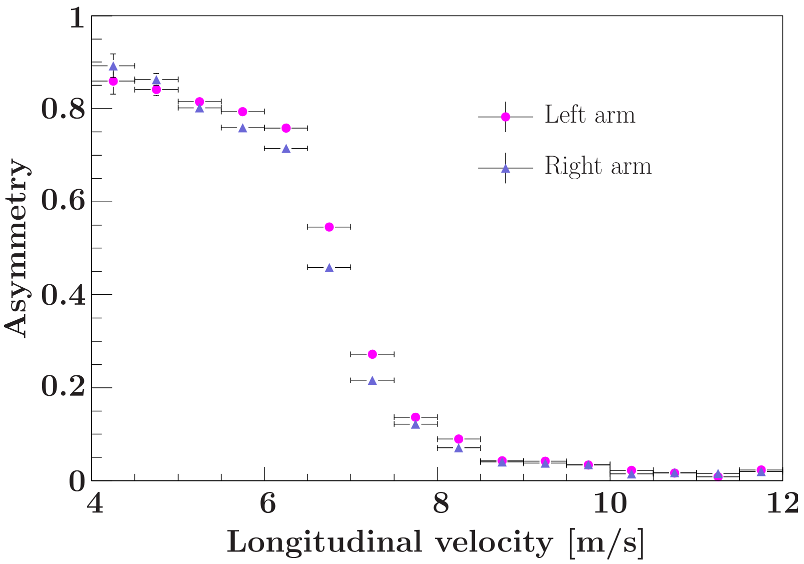

Figure 13.15: Polarization efficiency for the single arms.

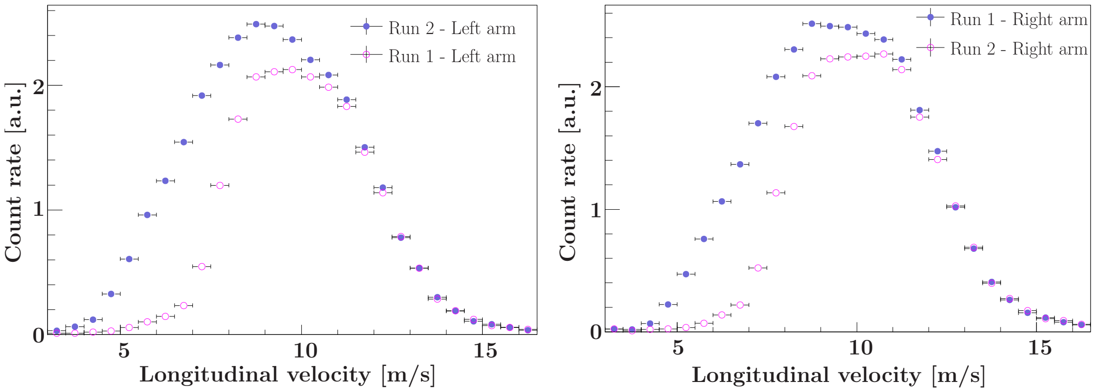

(a) Left arm (b) Right arm

Figure 13.16: Velocity spectra from two runs performed with the Y_{30}.

(especially above 9 m/s).

The corresponding asymmetries are plotted in Fig. 13.17. They are very similar with a value about 80% below 7 m/s. This is consistent with the previous measurement performed with single arms.

13.3 Conclusions

The main results concerning the developments for UCN spin analysis have been shown. Polarizer/analyzer and spin flippers have been qualified. It has been shown that a polarizing/analyzing efficiency of about 90% could be reached. The use of short spin flippers of a few centimeters with flipping efficiency close to 100% has also been demonstrated.

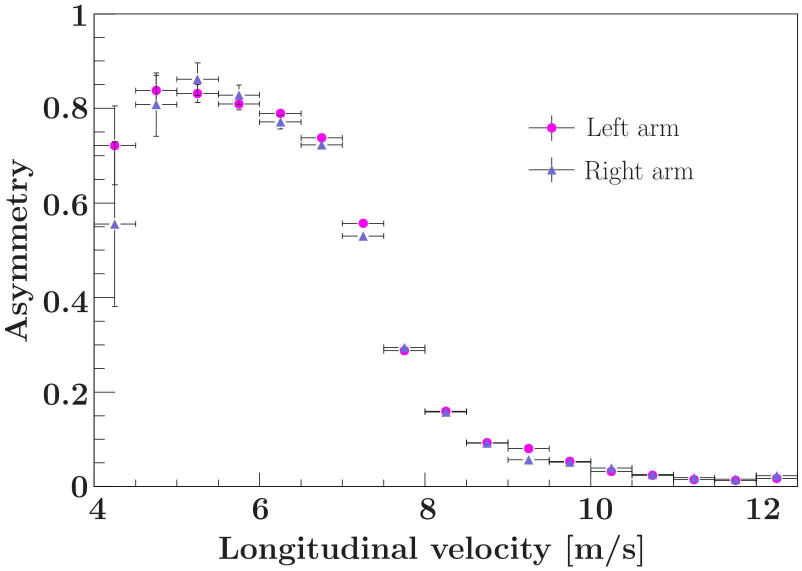

Figure 13.17: Polarization efficiencies of each arm measured with the Y_{30} system.

Two simultaneous spin analysis systems have been used at the ILL/PF2 TEST beamline in horizontal configuration. They have been tested with an inner coating made of copper foils. The UCN transmission of the Y_{30} system is about 50% whereas that of the Y_{120} is below 20%. Simultaneous spin analysis with the Y_{30} has shown that both arms have the same analyzing efficiency of 80%.

The simultaneous spin analyzing systems still need to be improved. The copper coating has to be replaced with a material with a higher Fermi potential (e.g. NiMo). The asymmetry of 80% has to be improved. The systems must be tested in vertical configuration below the storage chamber of the EDM spectrometer. The comparison with the sequential method of spin analysis has still to be carried out. This will enable to compare with our simulations of chapter 12 which have considered the systems in vertical position under the EDM spectrometer.

Conclusions and outlook

The neutron EDM d_n has played a crucial role in the study of P and CP/T symmetries for elementary particles. The upper limit of d_n has continuously decreased since the early 1950s. It has enabled to rule out many of the possible extensions to the Standard Model of particle physics. The new project at PSI plans to put the experimental limit on d_n at the level of 10^{-28} $e \cdot$cm. This will be possible due to the new intense spallation neutron source. The resulting intense UCN flux will require fast detectors.

Three kind of detectors have been tested at ILL during this thesis: the standard ^{3}He gas detector, the cascade-U and ^{6}Li-doped glass scintillators (GSx). Among the single scintillators, the 100 μm thick GS10 has the best UCN/gamma discrimination. Its sensitivity to the background (mainly gamma) at ILL/PF2 has been measured. It is about one order of magnitude larger than the background sensitivity of the gas detectors. Its detection efficiency is 20% lower than that of the ^{3}He detector on the EDM ILL/PF2 beamline. Below the EDM spectrometer and with a storage time of 100 s, it is 10% less efficient than the ^{3}He gas detector, whereas a 500 μm thick GS10 has a comparable efficiency than the ^{3}He gas detector. In order to improve the UCN/gamma discrimination, a GS3/GS20 stack has been developed. Each layer has a thickness of 100 μm. Since the GS3 (^{6}Li depleted) is almost transparent to UCN, all the neutron captures occur within the GS20 layer. The GS3 enables to get back the energy of the edge events from the GS20. In this way, a complete energy measurement is performed. The fraction of edge events has been reduced by about an order of magnitude as compared with the 100 μm thick GS10. Nevertheless, the GS3/GS20 stack is about 20% less efficient than the ^{3}He gas detector when it is used below the EDM spectrometer. This difference is partly due to its larger critical velocity (4.4 m/s instead of 3.2 m/s for the ^{3}He detector). Moreover, tests have shown that the GS3/GS20 stack was about 20% less efficient than the GS20 detector with a longitudinal velocity distribution lower than 10 m/s. Since both scintillators have the same critical velocity, the difference may be explained by the transmission through the GS3 layer. The cascade-U has been tested with three thicknesses of boron layer: 50, 200 and 800 nm. That of 200 nm has enabled to achieve a detection efficiency of about 80% with respect to the 500 μm thick GS10 scintillator. Monte-Carlo simulations have shown that this detector has a maximum absolute efficiency of about 82%. Optimal thicknesses have been calculated within the range 260-300 nm.

Sequential and simultaneous spin analyses have been compared through Geant4 Monte-Carlo simulations. The emptying of UCN from the EDM chamber was simulated. The height of the UCN storage chamber with respect to the horizontal feeding guide tube has been reduced to 1.2 m as planned for the new installation of the set-up at PSI. Two systems for simultaneous spin analysis (Y) have been simulated: one with an angle of 30° between both arms, and the other with an angle of 120°. The Y_{30} system has been found to detect about 12-15% more neutrons over a counting period of 40 seconds than the sequential system (depending on the initial spin population simulated). The number of losses inside the geometry and the asymmetry of the counted neutrons have been found to be similar when comparing the Y_{30} and the sequential systems. Moreover, the Y_{30} has been found to be 41% faster than the sequential method whereas the Y_{120} is only 25% faster. The experimental tests on spin analysis have shown that a polarizing/analyzing efficiency of about 90% can be reached. The spin flipper efficiency has been found to be consistent with 100%. The simultaneous analyzing systems were tested in horizontal configuration on the TEST beamline. The transmission of the Y_{30} system was about 50% whereas that of the Y_{120} was below 20%. Simultaneous spin analysis with the Y_{30} shown that both arms have the same analyzing efficiency of 80%.

A segmented detector made of several stack-PMT modules is under development at LPC. The scintillator stacks are planned to be assembled by molecular sticking in order to get a single optical medium, thus improving the light collection.

The simultaneous spin analyzing system requires further improvements. The coating has to be replaced in order to get a higher Fermi potential. For instance, NiMo would be interesting with its quite high critical velocity of about 6.5 m/s. The asymmetry of 80% has to be improved. Finally, tests need to be performed at PSI under the EDM spectrometer. This would enable to compare both methods of spin analysis and also to compare with the simulations presented in this thesis.

Bibliography

[1] E. M. Purcell und N. F. Ramsey. *On the Possibility of Electric Dipole Moments for Elementary Particles and Nuclei.* Phys. Rev. **78**, 807 (1950).

[2] S. K. Lamoreaux I. B. Khriplovich. *CP Violation Without Strangeness: Electric Dipole Moments of Particles, Atoms, and Molecules.* Springer-Verlag Berlin, Heidelberg 1997.

[3] E. M. Purcell J. H. Smith und N. F. Ramsey. *Experimental Limit to the Electric Dipole Moment of the Neutron.* Phys. Rev. **108** (1), 120–122 (1957).

[4] C. S. Wu *et al.* *Experimental Test of Parity Conservation in Beta Decay.* Phys. Rev. **105**, 1413–1415 (1957).

[5] G. Lüders. Dan. Mat. Fys. Medd. **28** (5) (1954).

[6] G. Lüders. *Proof of the TCP Theorem.* Ann. Phys. **2**, 1–15 (1957).

[7] N. F. Ramsey. *Time Reversal, Charge Conjugation, Magnetic Pole Conjugation, and Parity.* Phys. Rev. **109**, 225–226 (1958).

[8] J. H. Christenson *et al.* *Evidence for the 2π Decay of the* ${K_2}^0$ *Meson.* Phys. Rev. Lett. **13**, 138–140 (1964).

[9] A. D. Sakharov. *Violation of CP invariance, C symmetry, and baryon asymmetry of the Universe.* JETP Lett. **5**, 24–27 (1967).

[10] C. A. Baker *et al.* *Improved Experimental Limit on the Electric Dipole Moment of the Neutron.* Phys. Rev. Lett. **97**, 131801 (2006).

[11] M. Pospelov und A. Ritz. *Electric dipole moments as probes of new physics.* Ann. Phys. **318**, 119–169 (2005).

[12] X-G. He *et al.* *The neutron electric dipole moment.* Int. J. Mod. Phys. A **4**, 5011–5046 (1989).

[13] J. M. Pendlebury und E. A. Hinds. *Particle electric dipole moments.* NIM A **440**, 471–478 (2000).

[14] N. F. Ramsey. *A Molecular Beam Resonance Method with separated Oscillating Fields.* Phys. Rev. **78**, 695–699 (1950).

[15] P. D. Miller *et al.* *Limit to the Electric Dipole Moment of the Neutron.* Phys. Rev. Lett. **19** (7), 381–384 (1967).

[16] W. B. Dress *et al.* *Upper Limit for the Electric Dipole Moment of the Neutron.* Phys. Rev. **170** (5), 1200–1206 (1968).

[17] J. K. Baird *et al.* *Improved Upper Limit to the Electric Dipole Moment of the Neutron.* Phys. Rev. **179**, 1285–1291 (1969).

[18] W. B. Dress *et al.* *Improved Upper Limit for the Electric Dipole Moment of the Neutron.* Phys. Rev. D **7**, 3147–3149 (1973).

[19] W. B. Dress *et al.* *Search for an electric dipole moment of the neutron.* Phys. Rev. D **15** (1), 9–21 (1977).

[20] I. S. Altarev *et al.* *A Search for the Electric Dipole Moment of the Neutron using Ultracold Neutrons.* Nucl. Phys. A **341**, 269–283 (1980).

[21] I. S. Altarev *et al.* *A New Upper Limit on the Electric Dipole Moment of the Neutron.* Phys. Lett. B **102** (1), 13–16 (1981).

[22] J. M. Pendlebury *et al.* *Search for a neutron electric dipole moment.* Phys. Lett. B **136** (5,6), 327–330 (1984).

[23] I. S. Altarev *et al.* *Search for an electric dipole moment of the neutron.* JETP Lett. **44** (8), 360–363 (1986).

[24] K. F. Smith *et al.* *A Search for the Electric Dipole Moment of the Neutron.* Phys. Lett. B **234** (1,2), 191–196 (1990).

[25] I. S. Altarev *et al.* *New measurement of the electric dipole moment of the neutron.* Phys. Lett. B **276**, 242–246 (1992).

[26] I. S. Altarev *et al.* *Search for the Neutron Electric Dipole Moment.* Phys. Atom. Nuclei **59** (7), 1152–1170 (1996).

[27] P. G. Harris *et al.* *New Experimental Limit on the Electric Dipole Moment of the Neutron.* Phys. Rev. Lett. **82** (5), 904–907 (1999).

[28] A. Steyerl. *A "neutron turbine" as an efficient source of ultracold neutrons.* NIM **125**, 461–469 (1975).

[29] A. Steyerl *et al.* *A new source of cold and ultracold neutrons.* Phys. Lett. A **116** (7), 347–352 (1986).

[30] P. G. Harris *et al.* *The Neutron EDM experiment at the ILL.* NIM A **440**, 479–482 (2000).

[31] *A Proposal for a Cryogenic Experiment to Measure the Neutron Electric Dipole Moment (nEDM).* `http://arxiv.org/pdf/0709.2428`.

[32] A. Fomin *et al.* *An Ultracold Neutron Facility at PSI.* PSI Report TM-14-01-01. `http://ucn.web.psi.ch/techrev_final/ucn_techrev.pdf` (2000).

[33] *PSI: Search for the neutron electric dipole moment.* `http://nedm.web.psi.ch`.

[34] T. Kawai *et al.* *An improvement of the detection efficiency of a solid state UCN detector with a* ^{6}*Li/Ti multilayer neutron converter working at liquid helium temperature.* NIM A **378**, 561–563 (1996).

[35] *Modules gérés par l'acquisition Ganil (last update 1998).* `http://www.ganil.fr/acquisition/doc/liste_modules.html`.

[36] F. Sauli. *GEM: A new concept for electron amplification in gas detectors.* NIM A **386**, 531–534 (1997).

[37] *CASCADE: A High-Rates Detector for Neutron Applications in Science and Research.* `http://www.n-cdt.com`.

[38] *Applied Scintillation Technologies, glass scintillators.* `http://www.apace-science.com/ast/g_scint.htm`.

[39] G. Ban *et al.* *First Tests of* ^{6}*Li Doped Glass Scintillator for Ultracold Neutron Detection.* J. Res. Natl. Inst. Stand. Technol. **110** (3), 283–288 (2005).

[40] *Neutron scattering lengths and cross sections.* `http://www.ncnr.nist.gov/resources/n-lengths/`.

[41] C. W. E. van Eijk. *Inorganic-scintillator development.* NIM A **460**, 1–14 (2001).

[42] D. Drouin *et al.* *CASINO v2.42 – A Fast and Easy-to-use Modeling Tool for Scanning Electron Microscopy and Microanalysis Users.* Scanning **29**, 92–101 (2007).

[43] D.J.R. May. *A High Precision Comparison Of The Gyromagnetic Ratios Of The* ^{199}*Hg Atom And The Neutron.* PhD thesis University of Sussex 1998.

[44] U. Schmidt *et al.* *Position Sensitive UCN-Detector.* ILL Experimental Report 3-14-157 (2004).

[45] A. I. Egorov *et al.* *Production, storage, and polarization of ultracold neutrons.* Sov. J. Nucl. Phys. **19** (2), 147–152 (1974).

[46] C. D. Graham. *Iron and nickel as magnetization standards.* J. Appl. Phys. **53** (3), 2032–2034 (1982).

[47] K. Závěta. *The magnetization curves of thin iron films.* Czechosl. J. Phys. **6** (5), 473–481 (1956).

[48] R. T. Robiscoe. *A Spin Flip Problem.* Am. J. Phys. **39**, 146–150 (1971).

[49] V. I. Luschikov *et al. On the calculation of the neutron adiabatic spin-flipper.* NIM **228**, 159–160 (1984).

[50] S. V. Grigoriev *et al. Peculiarities of the construction and application of a broadband adiabatic flipper of cold neutrons.* NIM A **384**, 451–456 (1997).

[51] R. Herdin *et al. Experiment on the efficient polarization of ultracold neutrons.* NIM **148**, 353–357 (1978).

[52] T. D. Lee und C. N. Yang. *Question of Parity Conservation in Weak Interactions.* Phys. Rev. **104**, 254–258 (1956).

[53] S. K. Lamoreaux R. Golub, D. Richardson. *Ultra-Cold Neutrons.* Adam Hilger Bristol, Philadelphia and New York 1991.

[54] K. Green *et al. Performance of an atomic mercury magnetometer in the neutron EDM experiment.* NIM A **404**, 381–393 (1998).

[55] J. M. Pendlebury *et al. Geometric-phase-induced false electric dipole moment signals for particles in traps.* Phys. Rev. A **70**, 032102 (2004).

[56] C. A. Baker *et al. Experimental measurement of ultracold neutron production in superfluid* ^{4}*He.* Phys. Lett. A **308**, 67–74 (2003).

[57] C. A. Baker *et al. Development of solid-state silicon devices as ultra cold neutron detectors.* NIM A **487**, 511–520 (2002).

[58] O. Zimmer *et al. A precise measurement of the spin-dependent neutron scattering length of* ^{3}*He.* EPJdirect A **1**, 1–28 (2002).

[59] D. R. Rich *et al. A measurement of the absolute neutron beam polarization produced by an optically pumped* ^{3}*He neutron spin filter.* NIM A **481**, 431–453 (2002).

[60] *SNS Neutron EDM Experiment.* `http://p25ext.lanl.gov/edm/edm.html`.

[61] A. Serebrov *et al. Multi-chamber EDM Spectrometer. Status 2007.* 6th UCN Workshop "Ultra Cold & Cold Neutrons Physics & Sources" `http://cns.pnpi.spb.ru/ucn/articles/Serebrov3.pdf` July 2007.

[62] M. Lasakov *et al. Superconducting UCN polarizer for a new EDM spectrometer.* NIM A **545**, 490–492 (2005).

[63] E. B. Aleksandrov *et al. A Noise-Immune Cesium Magnetometer.* Inst. Exp. Tech. **50** (1), 91–94 (2007).

[64] M. Lasakov *et al. A large area silicon UCN Detector with the analysis of UCN polarization.* NIM A **545**, 301–308 (2005).

[65] V. K. Ignatovich. *The Physics of Ultracold Neutrons.* The Clarendon Press Oxford 1990.

[66] *Institut Laue-Langevin: Neutrons for Science.* `http://www.ill.eu`.

[67] *PSI: Ultra Cold Neutron Source.* `http://ucn.web.psi.ch`.

[68] J. Byrne. *Neutrons, Nuclei and Matter: An Exploration of the Physics of Slow Neutrons.* Institute of Physics Publishing Bristol and Philadelphia 1995.

[69] R. Golub und J. M. Pendlebury. *Ultra-cold neutrons.* Rep. Prog. Phys. **42**, 439–501 (1979).

[70] A. Steyerl. *Measurements of total cross sections for very slow neutrons with velocities from 100 m/sec to 5 m/sec.* Phys. Lett. B **29** (1), 33–35 (1969).

[71] H. Rauch *et al.* *Giant Absorption Cross Section of Ultracold Neutrons in Gadolinium.* Phys. Rev. Lett. **83** (24), 4955–4958 (1999).

[72] A. D. Stoika *et al.* *Upscattering Detected as the Main Reason for Anomalous Loss of Ultra-Cold Neutrons in Neutron Storage Experiments.* Z. Phys. B **29**, 349–352 (1978).

[73] V. V. Nesvizhevsky *et al.* *Investigation of storage of ultra-cold neutrons (UCN) in traps.* ILL Annual Report pages 62–64 (1997).

[74] P. Geltenbort *et al.* *A new escape channel for ultracold neutrons in traps.* JETP Lett. **70** (3), 170–175 (1999).

[75] V. V. Nesvizhevsky. *Interaction of Neutrons with Nanoparticles.* Phys. Atom. Nuclei **65** (3), 400–408 (2002).

[76] E. V. Lychagin *et al.* *Mechanism of Small Variations in Energy of Ultracold Neutrons Interacting with a Surface.* Phys. Atom. Nuclei **65** (11), 1995–1998 (2002).

[77] A. P. Serebrov *et al.* *Low-energy heating of ultracold neutrons during their storage in material bottles.* Phys. Lett. A **309**, 218–224 (2003).

[78] P. Maier-Komor *et al.* *Design and advanced preparation of mutilayer converters for ultracold-neutron detectors.* NIM A **561**, 45–51 (2006).

[79] T. Kitagaki *et al.* *An abnormal ultra-cold-neutron absorption in solid UCN-detectors.* NIM A **529**, 425–428 (2004).

[80] H. M. Shimizu *et al.* *Development of a solid-state detector with a ^{6}Li-Ti multilayer converter for ultracold neutrons.* NIM A **350**, 296–299 (1994).

[81] T. Kawai *et al.* *Neutron reflectivity of ^{6}Li-Ti multilayer with a Ni reflector applied to UCN detector.* Physica B **213.214**, 969–971 (1995).

[82] P. Maier-Komor *et al.* *Development of antireflection coatings with a* ^{6}*LiF/*^{62}*Ni multilayer converter for ultracold neutron detectors.* NIM A **480**, 104–108 (2002).

[83] P. Maier-Komor *et al.* *An ultracold neutron (UCN) detector with Ti/*^{6}*LiF multilayer converter and* ^{58}*Ni reflector.* NIM A **480**, 109–113 (2002).

[84] P. Maier-Komor *et al.* *Antireflection foils with multi-layer converter for ultracold neutron detectors.* NIM A **521**, 242–246 (2004).

[85] *SRIM - The Stopping and Range of Ions in Matter.* `http://www.srim.org`.

[86] W. K. Chu. *Calculation of energy straggling for protons and helium ions.* Phys. Rev. A **13** (6), 2057–2060 (1975).

[87] E. Bonderup und P. Hvelplund. *Stopping Power and Energy Straggling for Swift Protons.* Phys. Rev. A **4** (2), 562–569 (1971).

[88] *User Manual of the CASCADE-U 100 Detector* 04 2007. Contacts: `Martin.Klein@physi.uni-heidelberg.de`, `cschmidt@physi.uni-heidelberg.de`.

[89] P. Fierlinger *et al.* *A time-of-flight chopper for ultracold neutrons.* NIM A **557**, 572–575 (2006).

[90] *Ganil Data Acquisition System.* `http://wiki.ganil.fr/gap/wiki/Documentation/Software/DAS`.

[91] F. Bloch. *Nuclear Induction.* Phys. Rev. **70** (7,8), 460 (1946).

[92] I. I. Rabi. *Use of Rotating Coordinates in Magnetic Resonance Problems.* Rev. Mod. Phys. **26** (2), 167–171 (1954).

[93] A. Abragam. *The Principles of Nuclear Magnetism.* The Clarendon Press Oxford 1961.

[94] S. V. Grigoriev *et al.* *Neutron wave-interference experiments with adiabatic passage of neutron spin through resonant coils.* Phys. Rev. A **64**, 013614 (2001).

[95] A. Messiah. *Mécanique Quantique.* Dunod Paris 1960.

[96] F. Atchison *et al.* *The simulation of ultracold neutron experiments using GEANT4.* NIM A **552**, 513–521 (2005).

[97] M. Kuźniak. *The Neutron Electric Dipole Moment Experiment: Research and Development for the New Spectrometer.* PhD thesis Jagiellonian University 2008.

List of Tables

List of Figures